DE TTK

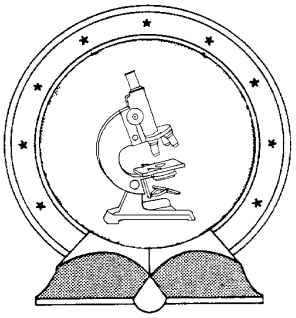

1949

The Role of Enzyme Mimetic Mn(III) Porphyrins in the Redox Reactions of Biologically Active Simple Inorganic Compounds

Ph.D. thesis

József Kalmár

Supervisor: *Dr. Gábor Lente*

UNIVERSITY OF DEBRECEN
Chemistry Graduate School
Debrecen, 2013

DE TTK

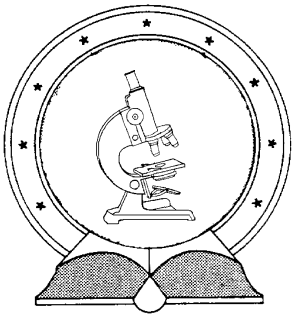

1949

The Role of Enzyme Mimetic Mn(III) Porphyrins in the Redox Reactions of Biologically Active Simple Inorganic Compounds

Ph.D. thesis

József Kalmár

Supervisor: *Dr. Gábor Lente*

UNIVERSITY OF DEBRECEN
Chemistry Graduate School
Debrecen, 2013

THE ROLE OF ENZYME MIMETIC Mn(III) PORPHYRINS IN THE REDOX REACTIONS OF BIOLOGICALLY ACTIVE SIMPLE INORGANIC COMPOUNDS

Értekezés a doktori (Ph.D.) fokozat megszerzése érdekében
a Kémia tudományágban

Írta: ***Kalmár József*** okleveles vegyész és angol-magyar szakfordító

Készült a Debreceni Egyetem Kémiai Doktori Iskolája
(Koordinációs kémiai programja) keretében

Témavezető: ***Dr. Lente Gábor*** egyetemi docens

A doktori szigorlati bizottság:

elnök: Dr. Rábai Gyula egyetemi tanár (DE)

tagok: Dr. Turányi Tamás egyetemi tanár (ELTE)

Dr. Tóth Imre egyetemi tanár (DE)

A doktori szigorlat időpontja: *2012. szept. 25.*

Az értekezés bírálói:

Dr. .....

Dr. .....

Dr. .....

A bírálóbizottság:

elnök: Dr. .....

tagok: Dr. .....

Dr. .....

Dr. .....

Dr. .....

Az értekezés védésének időpontja: *2013.* .....

Ezen értekezést a Debreceni Egyetem Természettudományi Doktori Tanács Kémiai Doktori Iskola K/2 Koordinációs Kémia programja keretében készítettem a Debreceni Egyetem természettudományi doktori (Ph.D.) fokozatának elnyerése céljából.

Debrecen, 2013. május 10.

Kalmár József

Tanúsítom, hogy Kalmár József doktorjelölt 2009 - 2013 között a fent megnevezett Doktori Iskola K/2 Koordinációs kémia programjának keretében irányításommal végezte munkáját. Az értekezésben foglalt eredményekhez és az ezekből született publikációkhoz a jelölt önálló alkotó tevékenységével meghatározóan hozzájárult. Az értekezés elfogadását javasolom.

Debrecen, 2013. május 10.

Dr. Lente Gábor

”Never say you think when you know,
or you know when you think.”

(”Sose mondd, hogy gondolod, amikor tudod,
és sose mondd, hogy tudod, amikor csak gondolod!”)

Quentin Tarantino

Acknowledgment

First of all, I would like to thank my supervisor, **Dr. Gábor Lente**, for working with me patiently since 2004, introducing me into the theory and practice of chemical kinetics, and using his inexhaustible creativity to advance my scientific career. I am grateful to **Prof. István Fábián** for carefully following my work with Gábor, and giving me critical advice in both practical, theoretical and also in personal matters. My greatest collaborator (and wife), **Mrs. Kalmár-Biri Bernadett,** needs to be acknowledged for the infinite patience and precision she showed during our scientific collaboration.

I would also like to thank:

- **Prof. Michael T. Ashby** for inviting me to spend a year in his laboratory in the University of Oklahoma, and for his professional and personal advice.
- **Prof. István Bányai** for introducing me into the practice of dynamic NMR measurements, and for his insightful comments regarding various projects.
- **Prof. Sándor Kéki** and **Dr. Lajos Nagy** for their indispensable help with the mass spectrometric measurements.
- **Prof. Mladen Biruš**, **Dr. Ana Budimir**, **Dr. Tin Weitner** and **Prof. Ines Batinić-Haberle** for the excellent collaboration, and also for their personal help during my stay in Zagreb, Croatia.
- **Prof. Ronald L. Halterman** and **Dr. Shawna B. Ellis** for letting me join their research project in the University of Oklahoma.
- **Mr. Gábor Bellér and Dr. Mario Gabričević** for their invaluable friendship, and for supporting me during the various stages of my graduate studies.
- **All the present and former members of the D524 laboratory** for their technical help, and also for the excellent atmosphere they provided during my stay.
- **My family** for providing me a calm and loving family background indispensable for successful scientific work.

Last, but not least I would like to express my gratitude towards **Richter Gedeon Tálentum Alapítvány** for financially supporting my graduate studies.

TABLE OF CONTENTS

1) INTRODUCTION

One of the greatest achievements of modern chemistry is to enable scientists to design reactions rationally for the production of almost any arbitrary chosen substance. The majority of these artificially designed chemical reactions, however, would be too slow to be beneficially utilized without the use of supplementary reactants called catalysts, which increase the reaction rates without contaminating the final products. Besides the rationally designed chemical processes, most of the naturally occurring reactions, e.g. in the living cell, are also catalytic. While chemical scientists implement a wide variety of catalysts, the biochemical processes are exclusively catalyzed by proteins or protein complexes called enzymes.

One of the largest and most widely studied families of catalysts are the metal complexes. In these substances, one or more metal ions or atoms are coordinatively bound to one or more ligand molecules. The quality of the ligand and the mode of its coordination to the metal center fundamentally determine the physical and chemical properties of the metal complexes. Thus, following careful scientific investigation, these properties can be fine tuned by altering the structure of the complexes. Nowadays, there is an increasing interest towards transition metal porphyrin complex based catalysts.[1,2,3,4] The exceptional structural stability of metal porphyrins provides a good scaffold for rationally designing catalysts by manipulating the electronic and chemical properties of these compounds by small structural changes.[5] Furthermore, the accessibility of several oxidation states of the metal center in a relatively narrow electric potential range also promotes the development of transition metal porphyrins as redox catalysts.[6] The beneficial implementation of these unique properties are also common in naturally occurring chemical processes. Most enzymes taking part in biochemical redox reactions contain non-peptide moieties called prosthetic groups and the prosthetic groups of several of these enzymes are transition metal porphyrins.[7,8] Most probably, the colorful palette of the porphyrin containing enzyme catalyzed redox reactions inspired many researchers to design artificial metal porhyrins to mimic these biocatalysts. The most promising use of enzyme mimetic transition metal porphyrins would be the treatment of diseases caused by the distortion of the redox homeostasis. One approach that seems successful so far is the introduction of

superoxide dismutase enzyme (SOD) mimetic metal porphyrin complexes to tissues which are exposed to abnormally high concentrations of free radicals. Thus, the so called oxidative stress related damage of these tissues could be eased.[9]

In order to design reactions effectively regardless of the field of usage, one has to gain a good understanding about the mechanism of the studied chemical processes. The mechanism of the reaction is the continuity of the elementary reaction steps from the consumption of the reactants until the formation of the products. One of the approaches for studying the mechanism of a chemical process is to characterize the intermediate reaction products analytically and make deductions regarding their formation and subsequent reactions. Another powerful tool is to find the correct mathematical correlation between the time-dependent concentrations of the reactants, intermediates and end products. These correlations are strictly determined by the mechanism of the chemical process in question and described by the principles of the chemical kinetics disciple.

Abbreviated names of the studied porphyrins:

MnTSPP^{3-}: Mn(III) meso-tetrakis(4-sulfonatophenyl)porphyrin

MnTMe-4-Pyp^{5+}: Mn(III) meso-tetrakis(N-methylpyridinium-4-yl)porphyrin

Mn^{IV}(O)TMe-4-Pyp^{4+}: oxo-Mn(IV) meso-tetrakis(N-methylpyridinium-4-yl)porphyrin

Mn^{V}(O)TMe-4-Pyp^{5+}: oxo-Mn(V) meso-tetrakis(N-methylpyridinium-4-yl)porphyrin

MnTEt-2-Pyp^{5+}: Mn(III) meso-tetrakis(N-ethylpyridinium-2-yl)porphyrin

MnTnHex-2-Pyp^{5+}: Mn(III) meso-tetrakis(N-hexylpyridinium-2-yl)porphyrin

MnTTEG-2-Pyp^{5+} ***or*** **Mn(III)TTEG**:
Mn(III) meso-tetrakis(N-tri(ethyleneglycol)pyridinium-2-yl)porphyrin

MnTTEG-2-Pyp^{4+} ***or*** **Mn(II)TTEG**:
Mn(II) meso-tetrakis(N-tri(ethyleneglycol)pyridinium-2-yl)porphyrin

2) RESEARCH OBJECTIVES

In the past few years, novel synthetic water soluble Mn(III) porphyrins have been developed for therapeutic purposes. The structures of some selected complexes are given in Scheme 1. Because the biologically important reactions of the Mn(III) porphyrins occur at the metal site and possibly involve the inner-sphere coordination of the reactant to the metal center, we found it important to determine the water exchange rates and study the exchange mechanism for representative Mn(III) porphyrins. Four complexes from Scheme 1 were chosen for this study: MnTEt-2-PyP^{5+}, MnTnHex-2-PyP^{5+}, MnTTEG-2-PyP^{5+} and MnTSPP^{3-}.

The high reactivities of Mn(III) porphyrins towards small molecules and the ability to undergo fast axial-ligand substitution during redox cycling are proposed to be key aspects of the in vivo and in vitro solution phase chemistry of these complexes. Accordingly, we characterized the biologically relevant redox reaction of a selected SOD mimic Mn(III) porphyrin complex (MnTTEG-2-PyP^{5+} as seen in Scheme 1) with N-hydroxyurea (HU as seen in Scheme 1) in vitro. The reason to study the reaction of HU with a Mn(III) porphyrin is that HU, similarly to other hydroxamic acids, may act as either a nitric oxide or a nitroxyl (HNO) donor under oxidative conditions, and Mn(III) porphyrins are described to display different reactivities towards NO donor and towards HNO donor compounds.

The defensive peroxidase enzymes lactoperoxidase, myeloperoxidase and eosinophil peroxidase commonly contain Fe(III) porphyrin (heme) prosthetic groups in their active sites, and among other substrates catalyze the oxidation of SCN^- by H_2O_2 to hypothiocyanite ion ($OSCN^-$ as seen in Scheme 1). To elucidate the mechanism of an analogous reaction, we have studied the oxidation of SCN^- with peroxomonosulfate ion (HSO_5^- formulated as Oxone®). The peroxidase mimicking catalytic effect of a Mn(III) porphyrin (MnTMe-4-PyP^{5+} as seen in Scheme 1) was also investigated in the $SCN^- + HSO_5^-$ + catalyst reaction system.

The stability of $OSCN^-$ and mechanism of its hydrolytic decomposition fundamentally determine its in vivo chemical availability. Considering that thiocyanogen ($(SCN)_2$) yields $OSCN^-$ when it is hydrolyzed at basic pH but does not at neutral pH, one might conclude that the hydrolysis of $(SCN)_2$ and that of $OSCN^-$ are interconnected near neutral pH. Therefore, we investigated the hydrolytic decomposition of both $OSCN^-$ and $(SCN)_2$ in detail at slightly acidic

and neutral pH to show that the observed mechanisms are relevant to the stability of $OSCN^-$ at physiological pH.

Scheme 1. Structures of the studied compounds.

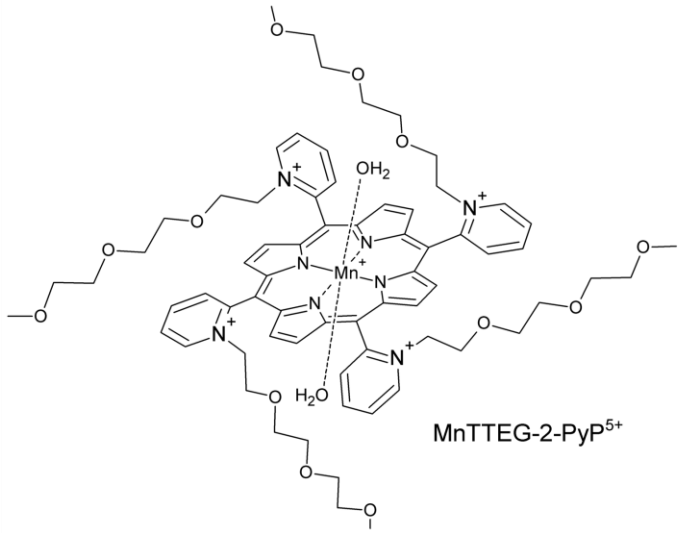

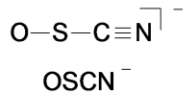

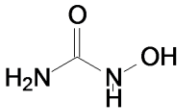

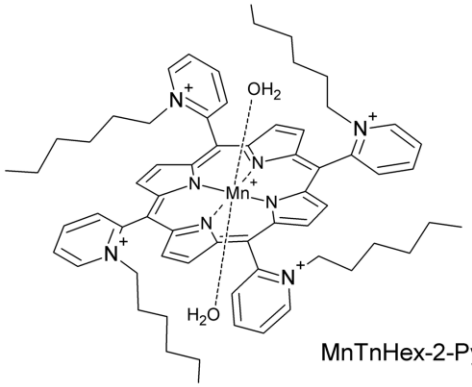

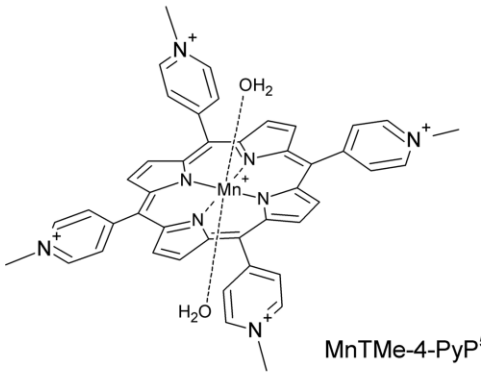

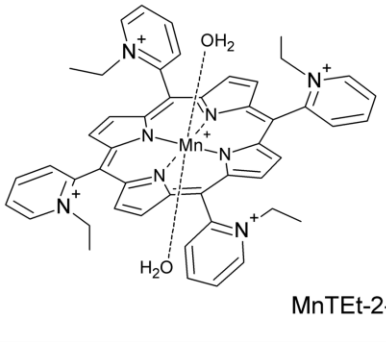

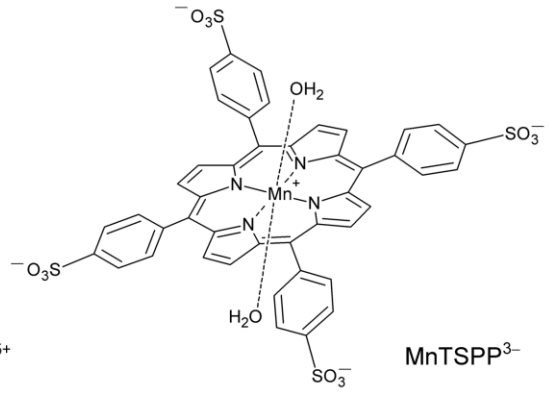

3) LITERATURE OVERVIEW

3.1) Manganese(III) porphyrins

Reactive oxygen and nitrogen species have been implicated in numerous pathological conditions including inflammation, ischemia/reperfusion, hemorrhagic shock, autoimmune diseases, neurological disorders, radiation injuries, carcinogenesis and senescence.[10,11,12,13] In the past few years, numerous metalloporphyrins have been developed for therapeutic purposes including the treatment of several diseases related to oxidative stress.[1415] Some of the most efficacious of these synthetic porphyrins are water soluble Mn(III) porphyrins.[16,17,18] Manganese lacks the toxicity related to Fenton chemistry, and the porphyrin cyclic structure provides both a high metal/ligand complex stability and rich biologically relevant redox chemistry at the metal site. Thus, novel water soluble Mn(III) porphyrins and porphyrin derivatives have been successfully developed as superoxide dismutase enzyme (SOD) mimics.[19,20,21,22] The most efficacious of these compounds, the ortho- Mn(III) N-alkylpyridyl-porphyrins, possess electron withdrawing positively charged quaternized pyridyl substituents close to the metal site,[13,17,21] which, similarly to the SOD enzymes themselves, allows: (1) the Mn(III)/Mn(II) reduction potential tuned to be in the desirable range, (around +300 mV vs. NHE), and (2) electrostatic facilitation for the approach of the negatively charged superoxide ion ($O_2^{\bullet -}$). In addition to the antioxidant capacity, these Mn(III) porphyrins are highly bioavailable as their in vivo ability to reduce oxidative stress related injuries are proved in several studies.[23,24,25,26] The lipophilic ortho isomers of Mn(III) N-alkylpyridyl-, N-methoxyalkyl- and N-tri(ethyleneglycol)-porphyrins are the most potent in vivo antioxidants. It is worth to mention that the oxygen-containing side chain derivatives, such as N-methoxyalkyl- and N-tri(ethyleneglycol)-porphyrins, possess superior properties relative to N-alkylpyridylporphyrins with respect to bioavailability and toxicity, yet such derivatization reduced compound lipophilicity. The reason to incorporate oxygen atoms into alkyl chains was to suppress micellar properties of longer alkyl-chain analogs and, as a result, MnTnBuOE-2-PyP^{5+} is considered for clinical development. The above mentioned SOD mimetic Mn(III) porphyrins are also reactive towards other oxygen or nitrogen species of in vivo toxicity, in particular towards peroxynitrite ion[27,28] and

nitric oxide.[29,30] Though the anionic $MnTSPP^{3-}$ has insignificant SOD-like activity,[20,34] it possesses considerable ability to reduce peroxynitrite ion[31] which justifies its use in studying oxidative stress injuries, particularly from a mechanistic point of view.

The high reactivity of these Mn(III) porphyrins towards small molecules and their ability to undergo fast axial-ligand substitution[32,33] during redox cycling are key aspects of their in vivo and in vitro solution-phase chemistry. The mechanism of the in vitro reactions of the mentioned SOD mimic complexes with free radicals (e.g., $O_2^{\bullet-}$, $ONOO^-$, $CO_3^{\bullet-}$) are well characterized. In some cases, even the complicated kinetics of the reactions were studied.[34] Despite the biological importance of the redox reactions of Mn porphyrins, only a few studies give detailed information on their mechanisms.[35,36,37] On the other hand, the protolytic equilibria and the electrochemical properties of some selected Mn(III) porphyrins are well characterized. As a general rule, the positively charged Mn(III) porphyrins could be deprotonated in two steps, in which the two axially coordinated water molecules lose protons. Structural studies indicate that the formation of the Mn=O species is predominant after the loss of the second proton instead of the HO–Mn–OH species.[38,39]

Since as early as 1924, it has been well accepted that both porphyrins and their metal complexes have affinity for malignant tissues.[40] This feature has led to their extensive application in nuclear medicine, X-ray and magnetic resonance imaging (MRI). In spite of the papers[41,42] describing the possible application of Mn(III) porphyrins as tumor imaging agents, only a few patents were awarded for the use of Mn(III) porphyrins as tumor visibility enhancing MRI contrast agents. The majority of the published papers are dealing with $MnTSPP^{3-}$ and the safe use of this porphyrin was proposed as an effective liver specific MRI contrast agent.[43] Although other Mn(II) and Mn(III) porphyrins were also studied and tested, only a non-porphyrin MnDPDP (Mangafodipir Trisodium™) reached phase III clinical trials to date for the detection of liver tumors. The $MnTSPP^{3-}$ complex has a high relaxivity, which was found to be even higher when bound to bovine serum albumin due to the preference of Mn(III) monomeric high spin state.[44] However, the application of $MnTSPP^{3-}$ in human medicine is precluded by its relatively high toxicity.[45] Therefore, $MnTSPP^{3-}$ is considered useful in radioactive (^{51}Mn) nuclear medicine rather than in MRI.[46] It was also recently shown that $MnTEt\text{-}2\text{-}PyP^{5+}$ and

MnTnHex-2-PyP^{5+} exhibit powerful potentials as molecular MRI probes for prostate cancer detection and may be particularly effective at selectively detecting multifocal disease in situ. In vivo, MnTEt-2-PyP^{5+} and MnTnHex-2-PyP^{5+} selectively accumulate in prostate tumors with 10–11-fold greater relaxation changes than in the normal prostate gland.[47,48] The relaxivity of MnTSPP^{3-} for water protons is unexpectedly high, mainly because of the high inner-sphere relaxation term.[49] The NMR dispersion curves of T_1 were described as unique for both shape and values[50] and the results could not be interpreted by the Solomon-Blombergen-Morgan theory.[51,52] In calculations, 10 ns was applied as the average residence time of the water molecule in the coordination sphere for both MnTSPP^{3-} and FeTSPP^{3-} complexes.[50] In spite of this remarkable progress in describing the magnetic aspects of the anomalous relaxivity of MnTSPP^{3-}, another important factor, i.e. its water exchange rate constant thus far has not been reported. The axial interaction of water with the central metal ion is of fundamental importance in both the ligand-substitution and redox processes of metalloporphyrins in aqueous solution. In the case of Fe(III) porphyrin complexes, the rates and the mechanism of water exchange were satisfactorily elucidated.[53] Some selected porphyrins, FeTSPP^{3-}, FeTMe-4-PyP^{5+} and FeTMPS^{4-} were studied as anionic, cationic and sterically shielded anionic complexes, in order. For all three complexes, a dissociative mode of activation was suggested on the basis of positive activation entropies and activation volumes. For the FeTMPS^{4-} complex, the limiting dissociative (D) mechanism was proposed because of the presence of bulky mesityl groups, while for the FeTSPP^{3-} and FeTMe-4-PyP^{5+} complexes, a dissociative interchange mechanism, I_d, was proposed. The water exchange of negatively charged FeTSPP^{3-} is five times faster[54] than that of FeTMe-4-PyP^{5+}, indicating a labilizing effect of the increased electron density on the metal ion center.

3.2) N-hydroxyurea

N-hydroxyurea (HU) has been used in human medical therapy for more than 40 years because of its broad antitumor spectrum. In limited cases of cervical[55] and uterine[56] cancer, the therapeutic effect of HU was found to be adequate without significant impact on normal cellular mechanisms. Currently, HU has become a standard agent against chronic myelogenous leukemia, polycythemia vera, and myeloproliferative disorders.[57,58] N-hydroxyurea has recently been introduced into

sickle cell anemia therapy[59,60,61] with considerable success. A long-term study indicates that there is a 40% decrease in mortality among patients who received the HU therapy.[62] The clinical efficiency of HU is assumed to be due to the in vivo formation of fetal hemoglobin.[62,63] However, some patients benefit from the HU therapy before any increase in the fetal hemoglobin concentration even takes place. This indicates that another mechanism of therapeutic action needs to coexist.[64] Sickle cell anemia patients receiving HU have shown increases in the production of nitric oxide (NO) metabolites, which include iron-nitrosylhemoglobin (HbNO), NO_2^-, and NO_3^- ions.[65,66,67] It has been reported that HU, similarly to many other hydroxamic acids, acts as a nitric oxide donor under oxidative conditions in vitro.[68,69] Direct nitric oxide producing reactions of HU and hemoglobin, myoglobin, or hemin may contribute to the overall pathophysiological properties of this drug.[70] EPR evidence showed that HU reacts with oxy-, deoxy-, and metHb to produce 2-6% of iron-nitrosylHb.[71] The formation of NO_3^- during the reaction of N-hydroxyurea and oxyHb and the lack of any nitrous oxide production in these reactions suggests the intermediacy of nitric oxide as opposed to its reduced form, nitroxyl (HNO). However, the exact mechanism by which HbNO forms in vivo is not completely understood.[72] Moreover, several articles show evidence for HNO formation from N-hydroxyurea under different oxidative conditions.[73]

Thus it is clear that the mechanisms of oxidation reactions of HU cannot be interpreted without the understanding of solution phase chemistry of NO and HNO. There are an increasing number of observations which show some biological significance for these species. More importantly for the present study, the kinetics and mechanism of the autoxidation, comproportionation and disproportionation reactions of NO and HNO are well described.[74,75] Higher oxidation state transition metal porphyrins (e.g., Mn(III) and Fe(III) porphyrins) tend to react directly with HNO to form the corresponding $\{Metal^{II}NO\}^7$ type complexes. On the other hand, NO reacts with the lower oxidation state transition metal porphyrins (e.g., Mn(II) and Fe(II) porphyrins) to give $\{Metal^{II}NO\}^7$ complexes. The thermodynamic stability of these $\{Metal^{II}NO\}^7$ complexes are high, but the release of NO can be facilitated by illumination, for instance. Some recent reports describe characteristically different reactivities of some Mn(III) porphyrins with NO and with HNO donor compounds. Martí *et. al*. showed[76] that nitroxyl donor compounds ($Na_2N_2O_3$ – Angeli's salt and toluene sulfohydroxamic acid) readily coordinate to

the cationic MeTMe-2-PyP^{5+} to give the corresponding {Mn^{II}NO}^{7} complex after oxidation. The anionic MnTSPP^{3-} does not react directly with the donor compounds, but reacts with their decomposition product HNO producing the {Mn^{II}NO}^{7} complex. Nitric oxide donors (sodium nitroprusside and S-nitroso-N-acetylpenicillamine) react with both cationic and anionic Mn(III) porphyrins only in the presence of a reducing agent.[76]

3.3) Thiocyanate and hypothiocyanite ions

The diverse, and often catalytic oxidation reactions of thiocyanate anion (SCN^-) are intensively studied (vide infra) because the biological importance of this anion is connected to its vivid in vivo redox chemistry[77]. In addition, SCN^- is an environmental pollutant, and its oxidative removal from industrial wastewater is essential. Furthermore, the in situ oxidation of SCN^- is of fundamental importance during the thiocyanation of various compounds in synthetic organic chemistry.

Thiocyanate ion is enzymatically oxidized by H_2O_2 to the antimicrobial hypothiocyanite ion[78] ($OSCN^-$) in vivo.[79,80,81] The rate of the direct $SCN^- + H_2O_2$ reaction is low,[82] but defensive peroxidase enzymes found in neutrophils (myeloperoxidase[83]) and eosinophil granulocites (eosinophil peroxidase[84]) catalyze this reaction effectively. Extracellular enzymes in milk (lactoperoxidase[85]), in the airways (lactoperoxidase[86]) and in saliva (salivary peroxidase[87]) are also efficient catalysts for the oxidation of SCN^- by H_2O_2. Furthermore, $OSCN^-$ is a potent bactericide and plays an important role in multiple stages of the non-immune defense system[79,80] at several physiological locations (e.g., in the mouth[88] and in the airways[89,90]). Thus, the insufficiently low in vivo local concentration of its precursor SCN^- is assumed to play an important role in the development of several chronic diseases, like cystic fibrosis.[77,91] Thiocyanate ion can be oxidized to $OSCN^-$ in a noncatalytic way by hypochlorous acid (HOCl)[92] and by hypobromous acid (HOBr).[93] These reactions may be important in controlling the redox activities of those defensive peroxidase systems where $SCN^-/OSCN^-$ and Cl^-/OCl^- or Br^-/OBr^- are simultaneously present. The understanding of the in vivo redox chemistry of SCN^- is further complicated by the fact that the two electron oxidation product of SCN^-; $OSCN^-$ can be subsequently oxidized by the same oxidizing agents as SCN^-, i.e. H_2O_2, HOCl or HOBr.[79,80,81] The reactions of $OSCN^-$ with these oxidizing agents are difficult to study, because $OSCN^-$ cannot be synthesized

in the absence of excess SCN^-. This problem is attributed to the "overoxidation" of $OSCN^-$, which is assumed to be of a similar order of magnitude as its production from SCN^-.[79,81,94] The half-life of the decomposition of $OSCN^-$ is on the order of several minutes at pH 7,[95] further limiting the applicable experimental conditions. Hypothiocyanite ion is a mild oxidizing agent, under physiological conditions, it reacts readily only with thiol (–SH) groups giving sulfenyl thiocyanates. The reactions of $OSCN^-$ with –SCN and –CN groups are also observed, but are scarcer.[81]

From environmental aspects, thiocyanate (SCN^-) and cyanide (CN^-) ions are considered to be the main inorganic anionic pollutants of wastewater and recycled water from metallurgical, mostly gold extraction plants. Although the toxicity of CN^- is undoubtedly higher than that of SCN^-, the latter can be found in larger quantities in metallurgical wastewater, and is more toxic to fish. The removal of SCN^- is important for the detoxification of industrial water because molecular oxygen can oxidize SCN^- to sulfate ion (SO_4^{2-}) and CN^- on a longer timescale, especially under UV radiation. For this reason, the admissible limit of SCN^- in metallurgical wastewater is usually as low as 0.05 mg/l. Technologically feasible processes for SCN^- removal almost exclusively utilize oxidative degradation approaches.[96] The fundamental reactions of these processes are catalytic,[97,98,99] photocatalytic,[100,101] and also biological oxidations.[102,103] The universal goal is to convert SCN^- quantitatively into environmentally more tolerable cyanate ion (OCN^-) (or carbonate ion (CO_3^{2-}) and nitrogen (N_2)) and SO_4^{2-}. The oxidizing agents of choice are usually hydrogen peroxide (H_2O_2)[97] and ozone (O_3)[99] in order to avoid the formation of any hazardous side products.

The oxidation of SCN^- plays a crucial role in organic synthetic strategies aiming at the preparation of thiocyanated compounds. To create a reactive intermediate for the thiocyanation of both aromatic[104,105,106] and aliphatic[107,108,109] compounds, a mixture of various oxidizing agents is used in situ with thiocyanate salts. Some of these synthetic methods utilize HSO_5^- in the form of Oxone® as the oxidizing agent in order to achieve milder reaction conditions with higher yields.[106,108,109]

Peroxomonosulfate ion is a peroxo compound and resembles H_2O_2 in its redox behavior, although the reactions of HSO_5^- with inorganic reducing agents[110,111] are characteristically faster than those of H_2O_2. The oxygen atom transfer reactions of HSO_5^- to halide ions (Cl^-, Br^- and I^-) are described in detail.[110] Thermodynamic

arguments are compiled to strengthen the proposed oxygen atom transfer mechanism. Stoichiometric[112] and kinetic results[113,114] indicate that the oxidation of SCN^- by HSO_5^- is a complicated multistep process under acidic conditions, at pH values between 2.2 and 6.3. The end products were identified as OCN^-, CN^- and SO_4^{2-}.[112] On the basis of calculations by the initial rate method and using numerical integration for simulating kinetic observations, Smith and Wilson concluded that the key initial step in the overall reaction is the equilibrium between SCN^- and HSO_5^-:[113,114]

$$HSO_5^- + SCN^- \rightleftharpoons SO_4^{2-} + HOSCN \qquad (R1^H)$$

where "HOSCN" was an uncharacterized intermediate. The formation of a second intermediate (thiocyanogen: $(SCN)_2$) is proposed in the rapid comproportionation of SCN^- and HOSCN, which inhibits the accumulation of HOSCN under acidic conditions. In a wide range of pH from the physiologically relevant neutral to the highly basic, the comproportionation of SCN^- + $OSCN^-$ to give $(SCN)_2$ is negligible, thus the accumulation of $OSCN^-$ is assumed in analogous oxidation reactions of SCN^-.[95,115] It has been recently reported that the positively charged MnTMe-2-PyP^{5+} and MnTMe-4-PyP^{5+} Mn(III) porphyrins display haloperoxidase mimicking catalytic activity in the oxidation of Br^- by H_2O_2.[116] The catalytically active species was identified to be the oxomanganese(V) (oxoMn(V)) porphyrin, Mn^V(O)TMe-4-PyP^{5+}, in both cases. The haloperoxidase activity of MnTMe-4-PyP^{5+} is described to be superior to that of MnTMe-2-PyP^{5+} in the Br^- + H_2O_2 reaction because of the generally better reactivity of the former porphyrin in oxygen atom transfer reactions.[117] In other papers, it is also shown that HSO_5^- can rapidly oxidize the above mentioned Mn(III) porphyrins into oxoMn(V) porphyrins.[118] When both HSO_5^- and SCN^- is present in the same reaction system with Mn(III) porphyrins, the formation of oxoMn(V) porphyrin is expected, which rapidly transfers the axial oxygen atom to SCN^- giving $OSCN^-$.

There have been no systematic investigations of the kinetics and mechanisms of the decomposition of $OSCN^-$ near physiologically relevant neutral pH conditions, in spite of the well accepted assumption that $OSCN^-$ is a short lived biological oxidizing agent, which can be only effective in the immediate vicinity of its place of production. While it is generally assumed that $OSCN^-$ is the only biologically active species produced from the enzymatic and non-enzymatic oxidations of SCN^-

in vivo, it is clear that many potentially reactive species must be formed during the hydrolytic decomposition cascade of $OSCN^-$ that produces the eventual products CN^-, OCN^-, SO_3^{2-}, and SO_4^{2-} detected in physiological fluids.[115,119] Older reports indicate that the decomposition of $OSCN^-$ is faster at low pH and with high concentrations of SCN^-. Considering the observation that $(SCN)_2$ does not yield $OSCN^-$ when it is hydrolyzed at neutral pH,[94,119,120,121] one might conclude that the comproportionation of HOSCN and SCN^- to give $(SCN)_2$ is involved in the decomposition mechanism of $OSCN^-$ near neutral pH. However, isotopic exchange of the C atoms of $OSCN^-$ and SCN^- is not observed near neutral pH, as might be expected for a reversible comproportionation:[122]

$$HOSCN + S^{14}CN^- + H^+ \rightarrow NCS–S^{14}CN + H_2O \qquad (R2)$$

$$NCS–S^{14}CN + H_2O \rightarrow HOS^{14}CN + SCN^- + H^+ \qquad (R3)$$

It is furthermore noteworthy that $(SCN)_2$ accelerates the decomposition of $OSCN^-$ (i.e., $OSCN^-$ and $(SCN)_2$ react even at neutral pH before the latter species decomposes). When HOSCN is reacted with $^{35}SCN^-$, the SO_4^{2-} that is obtained does not contain the label. While the ^{14}C and ^{35}S tracer studies do not preclude the involvement of NCSCN, O_2SCN^-, O_3SCN^-, and other possible intermediates, they suggest that the reversible equilibrium between $OSCN^-$ and $(SCN)_2$ in the presence of SCN^- (R2 and R3) is not involved in the decomposition mechanism. There is no experimental evidence for the intermediates that might be involved in the decomposition of $OSCN^-$, cyanosulfite (O_2SCN^-)[123,124] and cyanosulfate (O_3SCN^-)[125] have been observed in non-aqueous media but not in water. It has been previously suggested that the mechanism of hydrolysis of HOSCN at neutral pH involves dismutation of HOSCN because second order kinetics has been observed where the production of $(SCN)_2$ in the R2 – R3 equilibrium is not detectable.[94,126] However, others have reported first order kinetics for the decomposition of $OSCN^-$.[122] The picture is further complicated by the fact that CN^-, one of the presumed hydrolysis products of $OSCN^-$, reacts with $OSCN^-$ itself at pH > 7 to produce NCSCN, which subsequently hydrolyzes to produce a 1 : 1 mixture of SCN^- and OCN^-.[127]

4) EXPERIMENTAL METHODS

4.1) Reagents and solutions

Three of the investigated Mn(III) porphyrin complexes (MnTEt-2-PyP^{5+}, MnTnHex-2-PyP^{5+} and MnTTEG-2-PyP^{5+}) were synthesized according to reported procedures[12,13,18] by our collaborators at Duke University.[128] The other Mn(III) porphyrins (MnTMe-4-PyP^{5+} and MnTSPP^{3-}) were purchased from commercial suppliers. All of these complexes were readily soluble in water in the pH range from 0 to 14. The experimental work was typically done with 1 – 100 μM Mn(III) porphyrin solutions. The free Mn^{2+} content of the porphyrin complex stock solutions were measured to be between 1 and 2 % of the analytical concentration of the solutions.[129] Mn(II)TTEG was prepared by reducing MnTTEG-2-PyP^{5+} with excess ascorbic acid in solution under anaerobic conditions.[130] The $\{Mn^{II}NO\}^7$ complex Mn(II)TTEG–NO was prepared by mixing a NO containing solution to the Mn(II)TTEG solution.[130] Homemade NO gas was passed through 6 M NaOH, water, a column of solid NaOH, and finally collected into Ar-purged water.

Sodium thiocyanate (99.9+ %) and Oxone® were purchased from Sigma-Aldrich and used without further purification. The $KHSO_5$ content of Oxone® was regularly checked by iodometric titration. Sodium hypochlorite (NaOCl) stock solutions were prepared by sparging Cl_2 gas (99.5+%) into a 0.3 M solution of NaOH. The process was stopped at a NaOCl concentration less than 0.10 M. The basic NaOCl solutions were standardized by UV-vis spectroscopy[131] and iodometric titration.[132] For stopped-flow measurements, $(SCN)_2$ solutions were generated in situ in the first mixing cycle of the stopped-flow instrument by mixing an acidic (0.2 – 0.4 M $HClO_4$) solution of NaSCN (0.2 – 1.2 M) with a slightly acidified (pH 5 – 6) solution of HOCl (0.5 – 10 mM).[115,119] The reaction is complete within the mixing time. At least a 25-fold excess of NaSCN has to be used to avoid the overoxidation of $(SCN)_2$ by HOCl and get quantitative yields of $(SCN)_2$. The highest concentration of $(SCN)_2$ obtained by this method was 5 mM. Thiocyanogen decomposed with a half-life of some seconds. The analytical concentration of $(SCN)_2$ was determined photometrically, taking into account the formation of $(SCN)_3^-$ in the presence of SCN^-.[133] For analytical measurements, to avoid the high SCN^- background in the samples, $(SCN)_2$ was synthesized in CCl_4 by oxidizing $Pb(SCN)_2$ with Br_2[134,135,136] and was sequentially extracted into a

0.1 M solution of NaOH. Thiocyanogen in CCl_4 was standardized photometrically.[134,136] Solutions of NaOSCN were prepared using three different methods: (1) NaOSCN solutions were generated in situ for stopped-flow measurements in the first mixing cycle of the instruments by mixing a solution of 0.2 – 1.5 M NaSCN in 0.2 – 0.4 M NaOH with a solution of 0.5 – 15 mM NaOCl from pH 11 to 12.[92,134,137] The reaction is complete within 2 s and at least a 50-fold excess of NaSCN is required for a quantitative yield of $OSCN^-$. The maximum concentration of NaOSCN obtained was 7 mM, which was stable for several minutes.[137] (2) Solutions of NaOSCN were generated at pH 7 using the lactoperoxidase system (LPO + NaSCN + H_2O_2)[134,138] when the presence of a high excess of SCN^- was undesirable. For a quantitative yield, a 4-fold excess of SCN^- over H_2O_2 was required. The maximum concentration of $OSCN^-$ obtained by this method was 4 mM.[134,138] The enzyme was not removed from the system before further experiments. (3) Solutions with 1 : 1 SCN^- to $OSCN^-$ ratio were prepared by extracting $(SCN)_2$ in CCl_4 into a solution of 0.1 M NaOH, where $(SCN)_2$ promptly hydrolyzes to $OSCN^-$ and SCN^-.[134,138] Quantitative 1 : 1 mixtures were obtained when the resulting $OSCN^-$ concentration of the aqueous solutions did not exceed 4 mM. Sodium hypothiocyanite solutions were standardized photometrically.[92,110,137]

All other chemicals were purchased from commercial sources in ACS reagent grade or better and used without further purification. Ion exchanged and MILLIPORE ultrafiltered (Milli-Q synthesis A10) water was used to prepare all solutions. Sodium hydroxide solutions were standardized with potassium hydrogen phthalate, and HCl and $HClO_4$ solutions with the standardized NaOH solutions. The pH of the reaction mixture was maintained either by NaOH (from pH 13 to 11, no other additive necessary) or by borate (from pH 10.1 to 8.1), phosphate (from pH 7.8 to 5.8) or acetate (from pH 5.7 to 3.7) buffers. The pH was measured by a Metrohm 6.0234.110 combined glass electrode attached to a Metrohm 721 NET Titrino titrating unit. The electrode was calibrated by two buffers according to the IUPAC recommendations.[139] The ionic strength was adjusted and kept at a fixed value by the addition of $NaClO_4$ (and/or NaSCN). When necessary, the initial concentration of the dissolved O_2 in the reactant solutions ($c_0(O_2)$) was controlled by bubbling O_2 (99+ %) or Ar (99+ %) into the previously aerated solutions. When the required $c_0(O_2)$ was achieved, the reactant solutions were mixed in a sealable

vessel (usually a special quartz cuvette) under air tight conditions. The $c_0(O_2)$ was measured by a YSI 5100 Dissolved Oxygen Meter with a YSI 5010 probe calibrated by following the recommendations of the manufacturer.

4.2) Variable-temperature ^{17}O NMR measurements

^{17}O-enriched water (10 at%, Amersham, UK) was added to the solutions of the studied Mn(III) porphyrins in order to improve sensitivity. Reference solutions were prepared from tetraethylammonium chloride (TEA-Cl) and from $MnCl_2$. The concentration and the pH of the references were the same as that of the porphyrin solutions. Variable temperature ^{17}O NMR measurements were performed using Bruker DRX-400 (9.4 T, 54.2 MHz) or DRX-360 (8.5 T, 48.8 MHz) spectrometers. Homemade air-circulating and Eurotherm temperature control units were used to stabilize the temperature. The sample temperatures were corrected using the "methanol thermometer" method.[140] Longitudinal relaxation rates ($1/T_1$) were obtained by the inversion recovery method[141] and transverse relaxation rates ($1/T_2$) directly from the line widths assuming extreme narrowing limit conditions.

The collected data were analyzed according to Powel and Merbach's previously published procedure.[142] From the measured ^{17}O NMR relaxation rates and angular frequencies of the Mn(III) porphyrin solutions ($1/T_1$, $1/T_2$, and ω) and those of the TEA-Cl reference solutions ($1/T_{1A}$, $1/T_{2A}$, and ω_A) one can calculate the reduced relaxation rates and the chemical shift: $1/T_{1r}$, $1/T_{2r}$, and $\Delta\omega_r$. These may be written as in eqs. 1 – 3, where $1/T_{1m}$ and $1/T_{2m}$ are the relaxation rates in the bound water, $\Delta\omega_m$ is the chemical shift difference between the bound water and bulk water (in the absence of a paramagnetic interaction with the bulk water), P_m is the mole fraction of bound water, and τ_m is the mean residence time (or inverse exchange rate constant, $1/\tau_m = k_{ex}$) of water molecules in the inner coordination sphere. The total outer-sphere contributions to the reduced relaxation rates and chemical shift are represented by the terms $1/T_{1os}$, $1/T_{2os}$, and $\Delta\omega_{os}$.

$$\frac{1}{T_{1r}} = \frac{1}{P_m}\left[\frac{1}{T_1} - \frac{1}{T_{1A}}\right] = \frac{1}{T_{1m} + \tau_m} + \frac{1}{T_{1os}} \qquad (1)$$

$$\frac{1}{T_{2r}} = \frac{1}{P_m}\left[\frac{1}{T_2} - \frac{1}{T_{2A}}\right] = \frac{1}{\tau_m}\frac{T_{2m}^{-2} + \tau_m^{-1}T_{2m}^{-1} + \Delta\omega_m^2}{(\tau_m^{-1} + T_{2m}^{-1})^2 + \Delta\omega_m^2} + \frac{1}{T_{2os}} \qquad (2)$$

$$\Delta\omega_r = \frac{1}{P_m}\left(\omega - \omega_A\right) = \frac{\Delta\omega_m}{\left(1+\tau_m T_{2m}^{-1}\right)^2 + \tau_m^2 \Delta\omega_m^2} + \Delta\omega_{os} \qquad (3)$$

The relaxation rates of the bound water ($1/T_{1m}$ and $1/T_{2m}$) display an Arrhenius-like temperature dependence (eq. 4 with $i = 1$ and 2), where A_{im} is a pre-exponential parameter (in s^{-1}) and the dimensions of $E^{\ddagger}_{im}$ are the energies. The temperature dependence of the difference in chemical shift between the bound water and bulk water ($\Delta\omega_m$) is given by eq. 5, where g_L is the isotropic Landé g factor ($g_L = 2.0$ for Mn^{3+}), S is the electron spin ($S = 4/2$ for Mn^{3+}), $A/\hbar$ is the hyperfine or scalar coupling constant (in s^{-1}), and B is the magnetic field (in T). The exchange rate constant k_{ex} (inverse of mean residence time τ_m) of water molecules in the inner-sphere is assumed to obey the Eyring equation (eq. 6) where $\Delta S^{\ddagger}$ and $\Delta H^{\ddagger}$ are the entropy and enthalpy of activation for the exchange process. The exchange rate constant at 298.15 K (k_{ex}^{298}) can be calculated by substituting this temperature into the Eyring equation.

$$1/T_{im} = A_{im} \exp\left(-\Delta E_{im}^{\neq} / RT\right) \qquad (4)$$

$$\Delta\omega_m = \frac{g_L \mu_B S\left(S+1\right) B}{3k_B T}\frac{A}{\hbar} \qquad (5)$$

$$k_{ex} = \frac{k_B T}{h}\exp\left(-\Delta H^{\neq} / RT\right)\exp\left(\Delta S^{\neq} / R\right) \qquad (6)$$

In order to validate our methodological approach, the exchange rate constant at 298.15 K and the activation parameters of the water exchange reaction of $Mn(II)_{aq}$ in a slightly acidic solution were determined ($Zn(II)_{aq}$ was the reference) and were found to be in good agreement with previously reported data: 2.89×10^7 s^{-1} vs. 3.1×10^7 s^{-1}.[143,144]

4.3) UV-vis photometric pH titration

The pK_a values and the spectra of the differently protonated species of Mn(III)TTEG, Mn(II)TTEG and HU were measured by UV-vis titration. The spectral change was recorded in a spectral probe with 1.0 cm optical path length, which was attached to a Varian Cary 50 scanning spectrophotometer. Anaerobic conditions were maintained by constant Ar purging to avoid the oxidation of the

Mn(II) porphyrin complex.[39] After the stabilization of the pH after each aliquot of the titrant the UV-vis spectrum of the sample was scanned 3 times and averaged to increase the signal to noise ratio.[39]

4.4) Kinetic measurements

The majority of the kinetic experiments in the MnTTEG-2-PyP^{5+} + HU system were carried out in a PerkinElmer Lambda 25 scanning UV-vis photometer. The solutions of HU and MnTTEG-2-PyP^{5+} were loaded into a tandem-cuvette and the reaction was started with hand-mixing which usually introduced a ca. 4 s loss (< 1 %) of kinetic data. The same protocol was used for the measurements with an HP8453 photodiode array (PDA) photometer with adjustable integration time.

Fast kinetic experiments in the MnTTEG-2-PyP^{5+} + HU, in the SCN^- + HSO_5^- and in the MnTMe-4-PyP^{5+} + HSO_5^- reaction systems were carried out in an Applied Photophysics DX-17 MV stopped-flow instrument (Scheme 2) with either a photomultiplier tube (PMT) or a photodiode array (PDA) attached as the detector. Absorbance traces were collected using an optical cell of either 2.0 or 10.0 mm

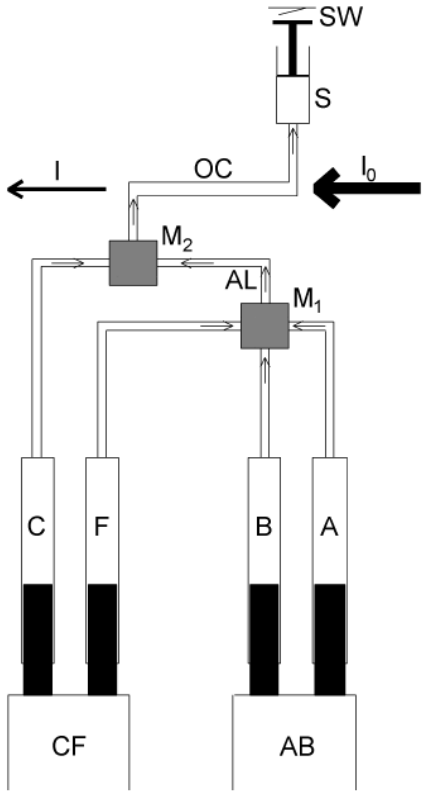

Scheme 2. Applied Photophysics DX 17-MV stopped-flow apparatus.
A, B, C, F: syringes; AB, CF: rams; AL: ageing loop; M1, M2: mixers, OC: optical cell; S: stop syringe; SW microswitch; I_0: incident light beam; I: exiting light beam.

path length. When available, the kinetic runs were run in 2 – 5 parallel duplicates and the recorded signal averaged to increase the signal-to-noise ratio of the kinetic curves. The dead time of the stopped-flow instrument was determined by the reaction of 2,6-dichlorophenol-indophenol (DCIP) with ascorbic acid (AA) under pseudo-first order conditions with AA in excess.[145] The dead time of the instrument was measured to be 1.51 ± 0.03 ms. By plotting the experimentally obtained k_{obs} values against [AA], deviation from linearity is observed above $k_{obs} = 600\ s^{-1}$ as seen in Figure 1, which means that higher k_{obs} values can be determined only with the elevation of relative experimental error. The deviation from linearity can be empirically described by the following equation:[146]

$$k_{obs} = \frac{k_{react} k_{mix} [AA]_T}{k_{react} [AA]_T + k_{mix}} \qquad (7)$$

where k_{react} is the rate constant of the DCIP + AA reaction and k_{mix} describes the rate of mixing the two reactants in the mixing chamber of the instrument. By determining k_{mix} from the calibration measurements it is possible to calculate precisely the theoretical rate constant k_{react} for a given reaction for which the measured k_{obs} is high and significantly deviates from k_{react}. However, the correction

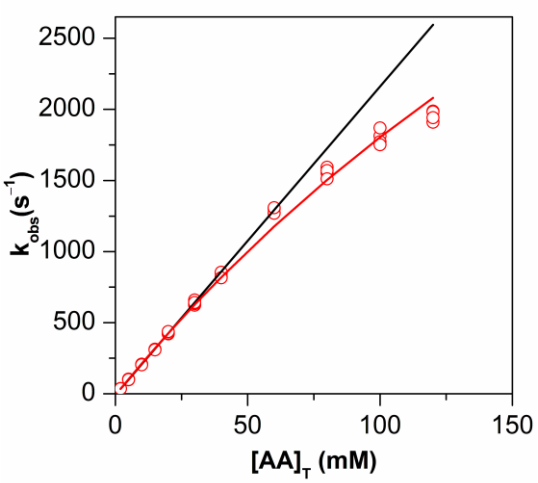

Figure 1. The measured values of the pseudo-first order rate constant (k_{obs}) of the reaction of 2,6-dichlorophenol-indophenol with ascorbic acid (AA). The values of k_{obs} deviate from the predicted linearity when the theoretical values become comparable to the rate of mixing of the two reactants (k_{mix}).

in the case of the current study is only ~10% when $k_{obs} \approx 1000$ s^{-1}. Therefore we avoided the unnecessary manipulation of the experimental data.

Sequential double-mixing stopped-flow experiments were carried out to study the reaction of the higher oxidation state $Mn^{IV/V}$(O)TMe-4-$PyP^{4/5+}$ porphyrins with SCN^-. The Mn(III) porphyrin MnTMe-4-PyP^{5+} was oxidized in the first mixing cycle of the instrument with HSO_5^- and subsequently mixed with SCN^- in the second mixing cycle. Some more sophisticated double-mixing stopped-flow experiments were designed and carried out to study the kinetics of the hydrolytic decomposition of $(SCN)_2$ or $OSCN^-$ at a given pH. The in situ generated acidic or basic reagent solution ($(SCN)_2$ or $OSCN^-$) was mixed with the appropriate buffer in the second mixing cycle. The concentration of the buffer was chosen to be at least in a 100-fold excess over that of the reactant. The resulting pH after the second mixing was always checked independently. Thiocyanate ion was used in high excess and for concentration dependence studies, its concentration was varied in the NaSCN solution used for the generation of the reagents in the first mixing cycle. A 2.0 s aging time before the second mixing ($\Delta\tau_1$) gave the highest yield from the in situ prepared reagents and ensured the excellent reproducibility of the experiments. The reaction of $(SCN)_2$ with HOSCN at pH 1 and pH 4 was also studied by the double-mixing stopped-flow technique. The in situ generated $(SCN)_2$ (pH 0) was reacted with freshly prepared solutions of NaOSCN (pH 13) to produce a reaction mixture with a pH between 0.58 and 0.70. For experiments around pH 4, the solution of NaOSCN was prepared with a sufficient amount of NaOAc for the resulting mixture to be buffered. For these experiments, NaOSCN was synthesized either by the extraction method (from $(SCN)_2$ in CCl_4) or by mixing NaSCN and NaOCl solutions with a hand mixer.

4.5) Electrospray ionization mass spectrometry (ESI-MS)

Mass spectrometric measurements were carried out with a Bruker micrOTOFQ mass spectrometer equipped with a quadrupole and time-of-flight (Q-TOF) analyzer in positive ion mode to follow the kinetics and identify the intermediates of the MnTTEG-2-PyP^{5+} + HU reaction system. The reaction mixture was introduced directly into the ESI source via a gas-tight syringe (Hamilton) and a syringe pump (Cole-Parmer Ins.). The syringe pump was synchronized with the software of the MS instrument, which enabled the precise determination of the

aging time of the reaction mixture at the instance of data recording. With this feature, reaction time resolved ESI-MS spectra were collected. The error of mass measurement was below 0.005 in the *m*/*z* range from 80 to 600. Sample solutions of ionic strength less than 1 mM were introduced into the MS to avoid decrease in the signal-to-noise ratio.

Additional experiments were performed with an Agilent 6538 UHD Accurate-Mass Q-TOF MS with a dual ESI ion source to identify the hydrolysis products of $(SCN)_2$ and $OSCN^-$. The error of the *m*/*z* measurement was less than 7.0 ppm in positive mode and less than 6.0 ppm in negative mode. All samples were diluted 1/10 – 1/50 before introduction to the MS, to avoid complication from the high ionic strength.

4.6) Ion chromatography (IC)

Chromatographic analyses were performed in a Metrohm modular-built IC instrument to quantitatively determine NO_2^- and NO_3^- ions produced in the MnTTEG-2-PyP^{5+} + HU reaction system, and CN^-, SCN^-, OCN^-, SO_3^{2-} and SO_4^{2-} ions produced in the hydrolytic decomposition of $(SCN)_2$ and $OSCN^-$. Nitrite and nitrate ions were measured with a Metrosep Dual 4_25_4.6 functionalized silica anion exchange column (25 mm × 4.6 mm). A cation suppressor column was used in every measurement. The suppressor was regenerated by 0.05 M sulfuric acid solution. Cyanide and thicyanate ions were measured using integrated amperometry detection, and OCN^-, SO_3^{2-} and SO_4^{2-} were measured using conductivity detection. An Ionpac AS16 column was used for the anions detected by integrated amperometry, and an Ionpac AS18 column and an ASRS 2 mm suppressor were used for ions detected by conductivity. Calibration of the methods was performed using a series of standard solutions.

As SCN^- is one of the expected decomposition products of both $(SCN)_2$ and $OSCN^-$, synthetic methods which require an initial large excess of SCN^- were not feasible for the chromatographic experiments. Thiocyanogen was synthesized in CCl_4 and extracted directly to a 50 mM acetate or phosphate buffer, and allowed to decompose for 15 min before the IC analysis. Sodium hypothiocyanite was produced by extracting $(SCN)_2$ synthesized in CCl_4 to a 0.1 M NaOH solution, which was immediately mixed with a phosphate or acetate buffer during constant stirring. These solutions were allowed to decompose completely for 30 min prior to

analysis. To study the effect of initial SCN^- excess, which was present during all the kinetic studies on the decomposition products, additional experiments were performed with buffer solutions containing an initial 8 to 11-fold SCN^- excess over $(SCN)_2$ or $OSCN^-$.

4.7) Data treatment

The raw data sets of the measurements were processed with the instrument controlling softwares. Further necessary data manipulation was typically carried out in MS Excel.

Initial rates in this study were always determined as initial rates of absorbance change of UV-vis traces. In order to emphasize this fact, absorbance unit (AU) is used throughout the text to denominate the unit of the (otherwise dimensionless) physical quantity absorbance. Singular value decomposition calculations for matrix rank analyses of time resolved UV-vis traces were carried out by Mathworks Matlab 4.2 or by Spectrum SpecFit/32[147] softwares. The raw data sets of the UV-vis photometric pH potentiometric titrations were evaluated by SpecFit/32 software using standard matrix algebraic calculations.

The experimental kinetic curves could not always be acceptably evaluated by fitting them one by one to an explicit time-dependent function. In these cases, the proposed kinetic model was directly fitted to multiple sets of kinetic curves recorded under different initial conditions. The simultaneous differential equation sets constructed from the kinetic models were solved with either Micromath Scientist 2.0[148] or with the ZiTa program package[149] using the GEAR algorithm.[150] Micromath Scientist was also universally used for Levenberg-Marquard least-squares fitting procedures. Estimated parameters are always quoted in text with indicating 1σ standard error. Parameters derived from other estimated parameters ("forced parameters") are quoted without indicating error.

5) RESULTS AND DISCUSSION

5.1) Water exchange of selected Mn(III) porphyrins

5.1.1) *Kinetics and mechanism*

The kinetics and mechanism of water exchange have been studied in detail for four selected Mn(III) porphyrins: MnTEt-2-PyP^{5+}, MnTnHex-2-PyP^{5+}, MnTTEG-2-PyP^{5+} and MnTSPP^{3-}. In highly basic (pH 12.0) solutions of these complexes, the ^{17}O relaxation rates and angular frequencies of bulk water were found to be the same as those of the reference solution (TEA-Cl) within experimental error, indicating that the Mn(III) porphyrin complexes show no measurable relaxivity enhancement. An explanation for this phenomenon could be the absence of water molecules from the inner coordination sphere of Mn(III) ions in the complexes under highly basic conditions. Therefore, the proposed dominant porphyrin species at this pH for all the four porphyrins must be the one in which only an oxo ligand is axially coordinated to the central Mn(III) as described in the literature (Mn=O).[38,39] Furthermore, the lack of relaxivity enhancement at pH 12 indicates that the contribution of outer-sphere water molecules to the reduced relaxation rates and the chemical shift must be negligible.

In slightly acidic solutions (pH 6.0), the temperature dependence of the reduced relaxation rates and the chemical shifts for the four Mn(III) porphyrin complexes are shown in Figure 2. The maximum observed in the temperature dependence of $1/T_{2r}$ is characteristic of the changeover from the "fast exchange" regime at high temperature, where T_{2m} is the dominant term in eq. 2, to the "slow exchange" regime at low temperature, where τ_m is the dominant term. The changeover between the fast and the slow exchange limits is also manifested in $\Delta\omega_r$: the maximum in $1/T_{2r}$ corresponds to the point of inflection in $\Delta\omega_r$. The exchange rates at 298.15 K and the activation parameters of the water exchange reactions of the four Mn(III) porphyrins were determined by nonlinear Levenberg-Marquard least-squares fit to the experimental curves and are given in Table 1. The temperature dependence of the reduced relaxation times and the chemical shift of a given Mn(III) porphyrin were fitted simultaneously. As previously explained in the experimental section, we used the full eq. 1 – 6 set, with setting the outer-sphere terms to zero in the analysis. Seven free parameters were left in the global least-squares fit: A_{1m}, $E^{\ddagger}_{1m}$, A_{2m}, $E^{\ddagger}_{2m}$, $A/\hbar$, $\Delta S^{\ddagger}$ and $\Delta H^{\ddagger}$. The fastest exchange rate is

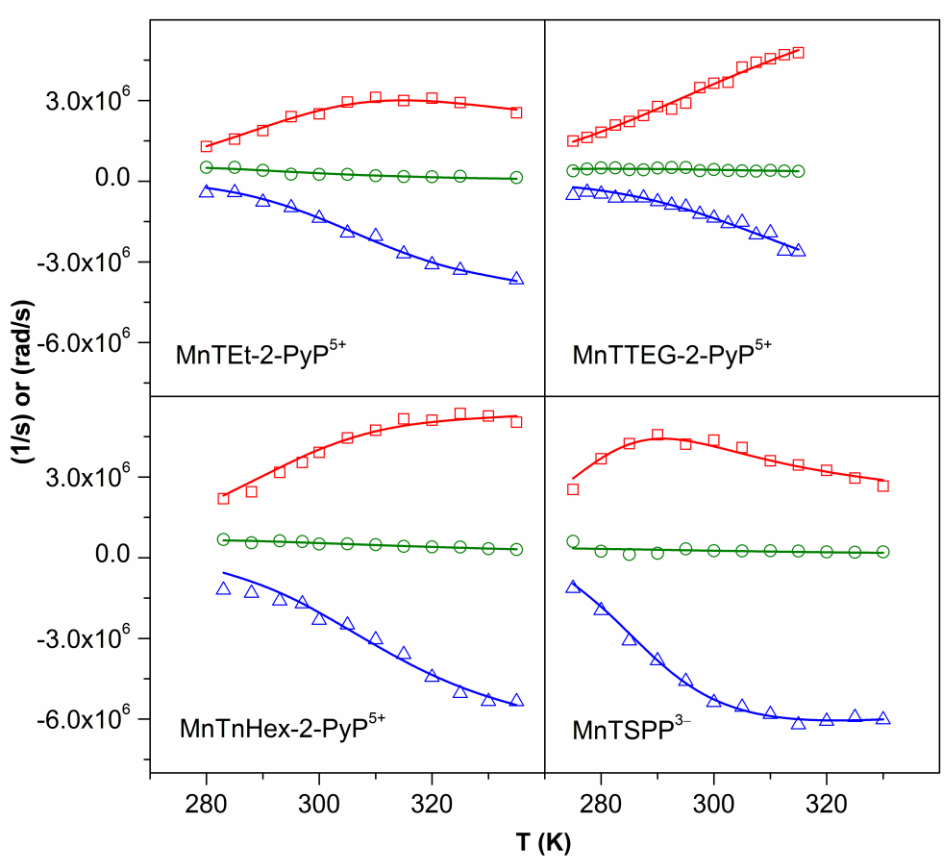

Figure 2. Reduced relaxation rates (circles: $1/T_{1r}$ and squares: $1/T_{2r}$ in s^{-1} units) and chemical shifts (triangles: $\Delta\omega_r$ in rad s^{-1} units) of the Mn(III) complexes studied as a function of temperature at pH 6. The lines are the results of calculation by using eqs. 1 – 6 and the appropriate parameters from Table 1. c(complex) = 10 mM.

observed for the negatively charged $MnTSPP^{3-}$ complex: $k_{ex}^{298} = 2.74 \times 10^7$ s^{-1}. The coordinated water molecules of the positively charged MnTEt-2-PyP^{5+}, MnTnHex-2-PyP^{5+} and MnTTEG-2-PyP^{5+} complexes are definitely less labile with $k_{ex}^{298} = 4.12 \times 10^6$ s^{-1}, $k_{ex}^{298} = 5.73 \times 10^6$ s^{-1} and $k_{ex}^{298} = 4.88 \times 10^6$ s^{-1}, in order. As seen in Table 1 the activation enthalpies of the water-exchange reactions decrease from 54 kJ mol^{-1} ($MnTSPP^{3-}$) to ca. 35 kJ mol^{-1} (positively charged complexes), but it is the effect of the activation entropy that causes the opposite tendency in the exchange rates. Namely, the smaller rate constants observed for the positively charged complexes are due to a significant decrease in $\Delta S^{\ddagger}$ from +79 J K^{-1} mol^{-1} for $MnTSPP^{3-}$ to ca. 0 J K^{-1} mol^{-1} for the positively charged complexes. It is also observed that the rates of the water exchange for Mn(III) porphyrins are almost a

Table 1. Activation parameters and rate constants of water exchange of Mn(III) porphyrin complexes and $Mn(II)_{aq}$ measured at pH 6.

species	k_{ex}^{298} (s^{-1})	$\Delta H^{\ddagger}$ (kJ mol^{-1})	$\Delta S^{\ddagger}$ (J $K^{-1}mol^{-1}$)	reference
$MnTE\text{-}2\text{-}PyP^{5+}$	4.12×10^6	36 ± 3	4 ± 10	*this work*
$MnTnHex\text{-}2\text{-}PyP^{5+}$	5.73×10^6	34 ± 7	–2 ± 23	*this work*
$MnTTEG\text{-}2\text{-}PyP^{5+}$	4.88×10^6	31 ± 5	–13 ± 20	*this work*
$MnTPPS^{3-}$	2.74×10^7	54 ± 5	79 ± 19	*this work*
	1.0×10^8			*50*
$Mn(II)_{aq}$	2.89×10^7	33.1 ± 0.6	9 ± 2	*this work*
	3.1×10^7	33.9	12.2	*144*
	2.1×10^7	32.9	5.7	*144*

magnitude higher than for Fe(III) porphyrins of similar structure and charge.[53]

The large positive value of the activation entropy suggests a limiting dissociative (D) water exchange mechanism for the $MnTSPP^{3-}$, whereas the close to zero obtained entropy values are indicative of the interchange mechanism (I) for the other three complexes. According to van Eldik and his co-workers,[53] the crucial factors that determine the exchange rate for Fe(III) porphyrins are the electron density of the metal center and the steric decompression of the complex. The dissociatively activated water exchange is faster when the electron density on the metal center is increased, weakening the metal–axial ligand (water molecule) bonds, and when the peripheral substituents of the porphyrin are bulky, which sterically hinders the complex and extrudes water molecules from the inner coordination sphere. The peripheral 4-sulfonatophenyl substituents of the $MnTSPP^{3-}$ porphyrin are strong electron donors that increase electron density at the central Mn(III) ion, which in turn labilizes axial water ligands and promotes the limiting dissociative water exchange mechanism similarly to the analogous Fe(III) complex $FeTSPP^{3-}$. In the case of $MnTEt\text{-}2\text{-}PyP^{5+}$, $MnTnHex\text{-}2\text{-}PyP^{5+}$ and $MnTTEG\text{-}2\text{-}PyP^{5+}$, the substituents on the porphyrin rings are among the strongest electron withdrawing groups due to the positively charged aromatic nitrogens in ortho positions. The electron withdrawing effect strengthens the metal–axial water

bonds, whose dissociation must be assisted by an incoming water molecule. The dissociation occurs simultaneously with the approach of an outer-sphere water molecule, i.e. the bond cleavage parallels the new metal–water bond formation. Thus the operative mechanism for the assisted water exchange in the positively charged complexes is an interchange process resulting in a significantly lower reaction rate than observed for the $MnTSPP^{3-}$ complex. The lower activation enthalpies for the reactions of the three positively charged complexes are therefore expected, since the metal–water bond cleavage in the transition state of the interchange mechanism is a concerted process with the formation of a new bond. Accordingly, the overall activation enthalpy must be significantly lower for the reaction following the interchange mechanism characterized by the dissociative mode of activation (I_d) than for the reaction following the limiting dissociative mechanism (D) that is likely to be the water exchange of $MnTSPP^{3-}$. However, it should be noted that, based on our results, a clear distinction between the mechanism characterized by the dissociative (I_d) and associative (I_a) mode of activation cannot be done; but it is rather based on the similarity with the water exchange kinetics of the analogous Fe(III) porphyrin complexes. A rather small difference between the exchange rates of $MnTEt\text{-}2\text{-}PyP^{5+}$ and $MnTnHex\text{-}2\text{-}PyP^{5+}$ complexes can be attributed to the different steric decompression of the two porphyrins. The hexyl side chains hinder the metal center somewhat more than the ethyls do. Therefore, if the associative mode of activation were operating, one would expect a decrease of the exchange rate due to a somewhat more difficult approach of the entering water molecule to the central metal ion. On the other hand, if the dissociative character of the interchange mechanism is proposed, the axial water molecules are expected to be slightly easier expelled from the $MnTnHex\text{-}2\text{-}PyP^{5+}$ complex, which is in agreement with the measured data. Still, the difference between the exchange rates is too small to be taken as a definite criterion for distinction between the I_d and I_a mechanisms. The proposed mechanism of water exchange of $MnTEt\text{-}2\text{-}PyP^{5+}$ and $MnTSPP^{3-}$ are in good agreement with those independently proposed by Ivanović-Burmazović *et. al*. based on variable temperature and high pressure ^{17}O NMR measurements.[33]

The introduction of a porphyrin chelate around the Fe(III) center labilizes the coordinated water molecules in the axial position by inducing electron density on the metal center. It was reported that the water exchange rate constants on the

Fe(III) porphyrins are ca. 10^4 times larger than on the hexa-aqua system.[53] Based on the similarity between the size of the high spin Fe(III) and Mn(III) ions, and the close resemblance of the intimate water exchange mechanisms observed for these two ions, the rate constant of the water exchange on aqua Mn(III) ion can be estimated to be in the range of ca. $10^2 – 10^3$ s^{-1}, depending whether our data on $MnTSPP^{3-}$ are compared to the rate constant of the water exchange on $FeTSPP^{3-}$ reported in ref. 53 or in ref. 54.

In addition, we calculated the residence time of the water coordinated in $MnTSPP^{3-}$ at room temperature to be 36 ns. Thus, the applied 10 ns in the analysis of NMRD curves of relaxivity of water protons has not been far from the reality. Therefore, the interpretation of the anomalous relaxivity of $MnTSPP^{3-}$, which was confirmed by the density functional theory calculations of anomalous spin-polarization mechanism for high-spin Mn(III) porphyrin complexes,[151] is probably correct, or at least it is not the result of the misused water residence time.[49,50]

5.1.2) *Implications to inner-sphere redox reactions*

The second order rate constants of the one electron oxidations of superoxide ion by $MnTEt\text{-}2\text{-}PyP^{5+}$ and $MnTnHex\text{-}2\text{-}PyP^{5+}$ in neutral solution ($k = 5.8 \times 10^7$ and 2.7×10^7 M^{-1} s^{-1}, respectively[13]) are an order of magnitude higher than the obtained first order rate constants for the water exchange of the two porphyrins. This statement is also true for the second order rate constants of the reductions of $ONOO^-$ and $CO_3^{\bullet-}$ by $MnTEt\text{-}2\text{-}PyP^{5+}$, ($k = 3.4 \times 10^7$ and 3.2×10^8 $M^{-1}s^{-1}$, respectively[27]), under in vivo and in vitro accessible concentrations. However, the inner-sphere electron transfer mechanisms for these redox reactions are not precluded by the numerical values of the rates of water exchange reactions. A confirmation of this statement can be invoked by a detailed analysis of the reaction mechanism. The first step in the inner-sphere electron transfer mechanism is assumed to be a fast ion pair formation equilibrium between the reactants, followed by the rate determining step of the aqua ligand substitution on the metal ion center. According to the Fuoss equation, the ion pair formation constant for the 5+ and 1– charged ionic reactants can be calculated as $K_{os} = 200 – 350$ M^{-1} depending on the closest approach of the ions that is usually taken as 0.4 – 0.5 nm when a water molecule separates them.[152] Therefore, the first order rate constants for the substitution of the water molecule by $O_2^{\bullet-}$, $ONOO^-$ and $CO_3^{\bullet-}$ (k ca. $10^5 – 10^6$ s^{-1})

are in a slightly better agreement with the water exchange rate constants obtained in the present study (k_{ex} ca. $10^7 – 10^8$ s^{-1}), but the conformity can still be improved by considering the various oversimplifications applied in the Fuoss equation. For example, the solvation of the complex ions statistically reduces the ligation rate constant by approximately an order of magnitude. Furthermore, it was shown that the aromatic groups of the porphyrins provide a hydrophobic environment that may also change the accessibility of central metal ions to the negatively charged species involved in the above mentioned dismutation and reduction processes.[153] Independently from our study, Ivanović-Burmazović *et. al*. arrived to a similar conclusion regarding the elementary mechanisms of the redox reactions of radicals with Mn(III) porphyrins by investigating the temperature and pressure dependence of water exchange of $MnTEt\text{-}2\text{-}PyP^{5+}$ and $MnTSPP^{3-}$.[33]

5.2) The autoxidation of N-hydroxyurea catalyzed by MnTTEG-2-PyP^{5+}

5.2.1) *Characterization of the reactants*

The pK_a values of the two axially coordinated water molecules of Mn(III)TTEG were determined by UV-vis photometric titration to be pK_{a1} = 10.71 ± 0.03 and pK_{a2} = 11.7 ± 0.1. The measured pK_a values and the individual spectra of each species (Figure 3) are similar to those of analogous Mn(III) porphyrins described in the literature.[39] In the second deprotonation step, the formation of an Mn=O species is assumed in accordance with the literature as discussed earlier in this thesis.[39] The mechanism of water exchange of Mn(III)TTEG at pH 6 is proposed to be the

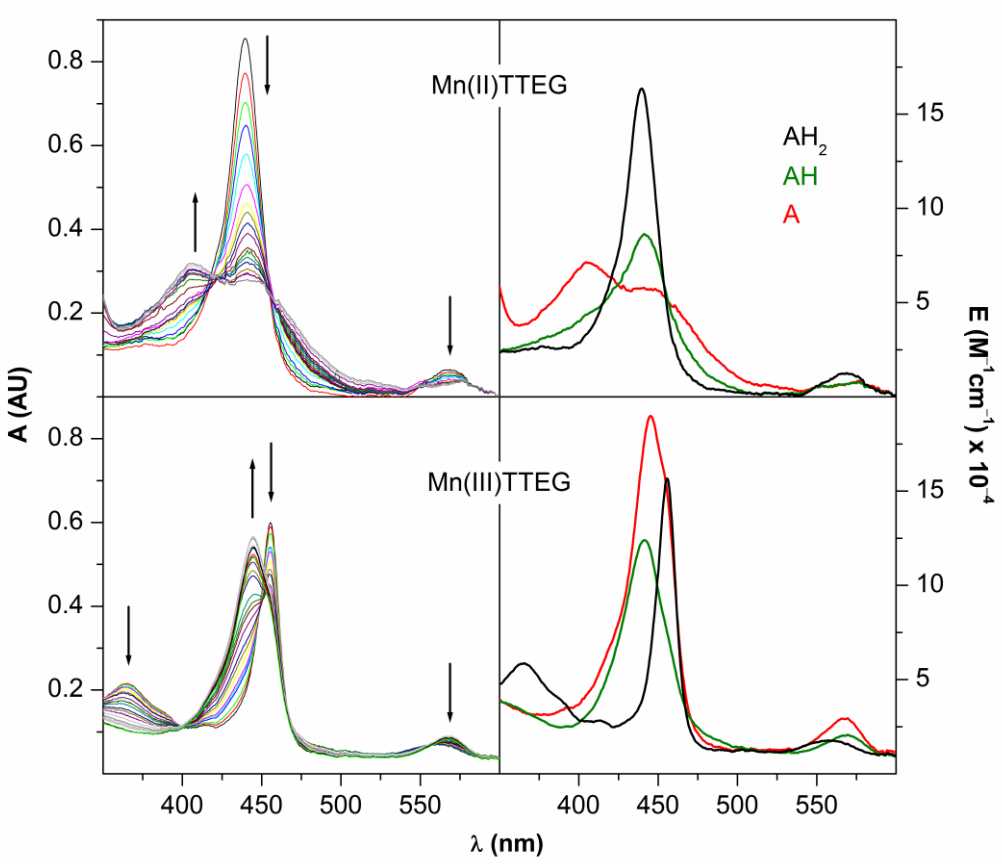

Figure 3. UV-vis titration of Mn(II)TTEG (up) and Mn(III)TTEG (down) from pH 9.3 to pH 12.6. Left: spectral change, the pH increases with the arrows. Right: calculated individual spectra of the protonated (black), the singly deprotonated (green) and the doubly deprotonated (red) species. c(Mn(III)TTEG) = 3.80 μM or c(Mn(II)TTEG) = 5.23 μM, I = 1.0 M, T = 25.0 °C, anaerobic conditions.

dissociative interchange (I_d) as detailed in the previous chapter. A UV-vis photometric titration was carried out under anaerobic conditions also with the reduced complex, Mn(II)TTEG, giving $pK_{a3} = 9.8 \pm 0.1$ and $pK_{a4} = 11.7 \pm 0.1$. The spectra of the corresponding species were calculated (Figure 3).[39] The ESI-MS spectra of Mn(III)TTEG and Mn(II)TTEG were recorded from pH 10.7 solutions.

The pK_a of the –OH group in N-hydroxyurea (HU) was measured to be $pK_{a5} = 10.98 \pm 0.06$ [154,155] and the UV-vis spectra of the protonated and the deprotonated forms were recorded. The stability of the HU stock solution was studied at pH 11.7. Under anaerobic conditions, no change of the UV-vis spectrum was detected in 4 hours. Under aerobic conditions ($c_0(O_2) = 2.5 \times 10^{-4}$ M), the HU signal (c_0(HU) = 50 μM) decays in a pseudo-first order reaction characterized by $k_{obs} = (5.0 \pm 0.5) \times 10^{-4}$ s^{-1} ($k_{obs}/c_0(O_2) = 2$ M^{-1} s^{-1}). This process is interpreted as the direct autoxidation of HU, but it is substantially slower than the catalytic reactions described in this chapter, and its contribution to the overall process was taken into account, as detailed later.

5.2.2) *Effects of pH, dissolved oxygen and light on the kinetics of the reaction*

The UV-vis spectral change observed during the reaction of HU + Mn(III)TTEG at pH 11.7 and the corresponding kinetic curve at 430 nm can be seen in Figure 4. The displayed wavelength and the indicated pH was selected based on an analysis of the spectral effects to give a maximum signal for the first, increasing part of the kinetic curve. In this region, the absorbance first rises then decreases, which is consistent with the formation of an intermediate. It should be emphasized that Figure 4 shows only a few characteristic spectra for clarity, and these may appear to show an isobestic point at around 435 nm. However, the full set of spectra does not show a consistent isobestic point and the apparent constancy of the absorbance around 435 nm was understood to be the consequence of some compensation between molar absorbances and reaction stoichiometries in a multi-step process, a phenomenon known from the literature of kinetics. In any case, the multi-step nature of the studied process is clearly demonstrated by the maximum on the kinetic curves measured at 430 nm. The reaction is faster at higher pH and no reaction is observed within 60 min at pH 6.0 or below. To be able to follow the reaction system conveniently, the majority of the kinetic experiments were run at pH 11.7, where the process is complete in a few minutes.

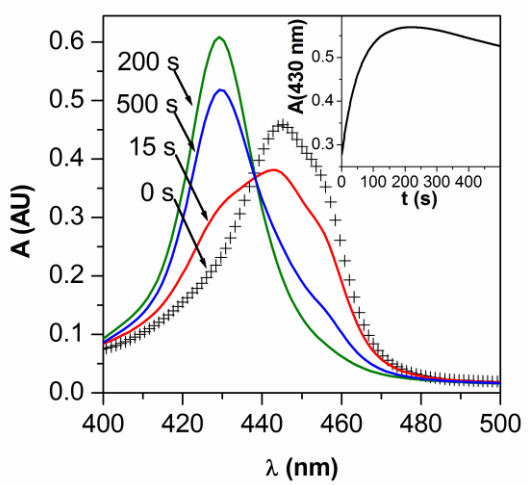

Figure 4. Representative spectral change observed during the reaction of Mn(III)TTEG and HU. The spectrum at 0 s is the sum of the spectra of the reactants recorded before mixing. Inset: kinetic curve recorded at 430 nm, which is the A_{max} of the major intermediate. c_0(Mn(III)TTEG) = 3.75 μM, c_0(HU) = 15.0 μM, pH 11.70, $c_0(O_2)$ = 254 μM, I = 1.0 M, T = 25.0 °C.

The reaction has been found to be significantly faster with higher initial concentrations of dissolved O_2 ($c_0(O_2)$), as detailed later. Under anaerobic conditions, no absorbance increase is observed at 430 nm at pH 12.7 within 60 s. The majority of the kinetic measurements were carried out with solutions initially containing 2.5×10^{-4} M O_2 (i.e., equilibrated with air at 1.0 bar and thereafter sealed from air). The addition of $MnCl_2$ or Na_2EDTA has no effect on the reaction.

The fast steps of the reaction were studied in a stopped-flow apparatus and the slower steps in scanning or diode array photometers. An unusual observation has been made: the kinetic behavior of the reaction varies with the type of instrument used for data recording under otherwise identical conditions. Additional investigation revealed that the reaction is light-sensitive and during the photometric measurements, the instrument-specific illumination of the reaction mixtures altered the kinetics. The light intensity dependence of the reaction was studied by the variation of the exit slit width of the monochromator of the stopped-flow apparatus or the integration time of the diode array photometer.[156] In the case of the stopped-flow measurements, the increase in the spectral bandwidth with increasing slit width was taken into account. Detailed experiments proved that the initial reaction rate at 430 nm (v_0^{430nm}) slightly decreases with the intensity of illumination, and the

intermediate with an A_{max} at 430 nm decays with a rate proportional to the light intensity (Figure 5). Because of the photosensitivity of the reaction system, the majority of kinetic experiments were performed in a scanning photometer where the light intensity was set at its minimum. Only the fastest experiments (milliseconds) were followed by stopped-flow PDA. The photochemical effect is proven to be negligible over such a short timescale.

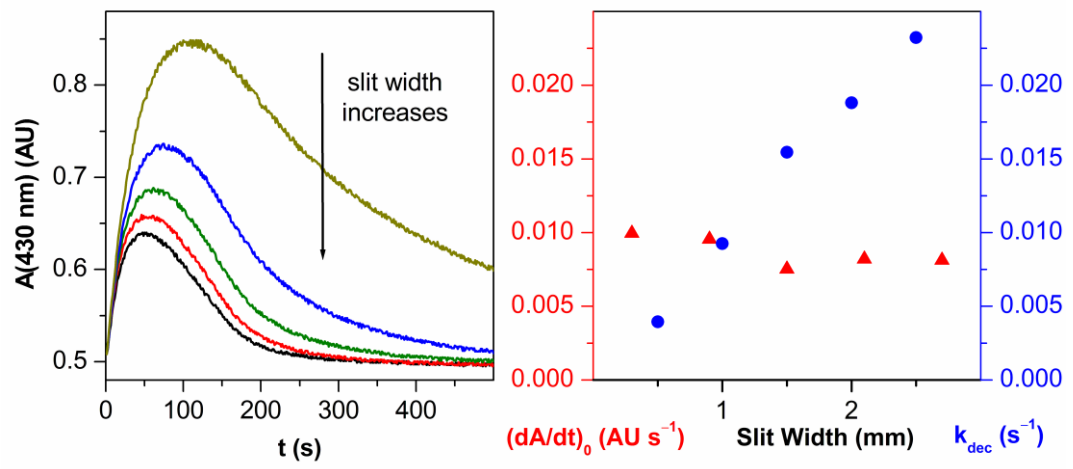

Figure 5. The effect of the intensity of illumination on the reaction of Mn(III)TTEG and HU. The exit slit width of the monochromator in the stopped-flow instrument was varied from 0.5 mm to 2.5 mm in 0.5 mm steps. The light intensity is roughly proportional to the exit slit width. Left panel: Kinetic traces at different slit widths of the monochromator. Right panel: The initial reaction rate of the overall reaction (red triangles) and the pseudo-first order rate constant of the decay of the Mn(II)TTEG–NO (A_{max} at 430 nm) intermediate (blue dots) as functions of the exit slit width of the monochromator. c_0(Mn(III)TTEG) = 7.02 μM, c_0(HU) = 15.0 μM, pH 11.70, $c_0(O_2)$ = 254 μM, I = 1.0 M, T = 25.0 °C.

5.2.3) *Intermediates and products*

The visible part of the UV-vis spectrum of the product solution (60 min after mixing Mn(III)TTEG and HU) is identical to the spectrum of the Mn(III)TTEG reactant. Matrix rank analysis of the time-resolved UV-vis spectra indicates the presence of 4 absorbing species during the course of the reaction at constant pH,[157,158] thus the formation of 3 intermediates are expected. The $\{Mn^{II}NO\}^7$ complex of Mn(II)TTEG, i.e. Mn(II)TTEG–NO was independently prepared in solution, and as seen in Figure 6, its UV-vis spectrum was found to be identical to

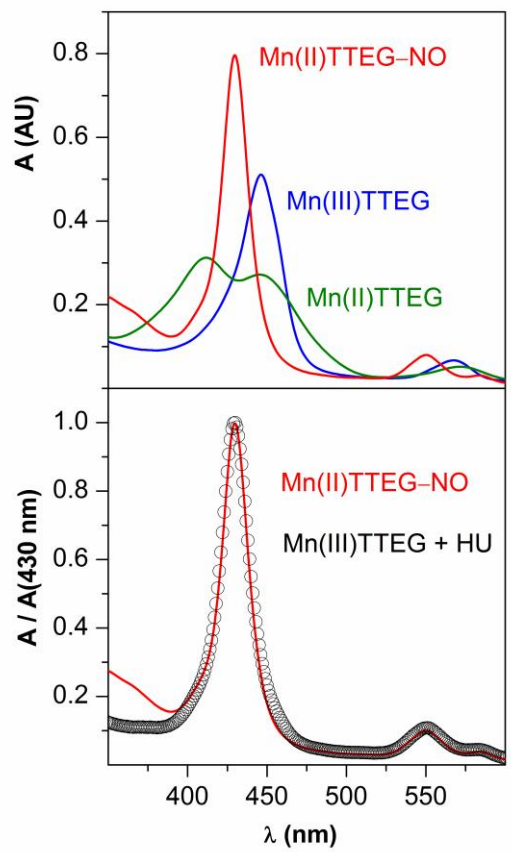

Figure 6. Up: The UV-vis spectra of Mn(III)TTEG, Mn(II)TTEG and Mn(II)TTEG–NO. c(Mn(III)TTEG) = c(Mn(II)TTEG) =c(Mn(II)TTEG–NO) = 3.54 μM, c(NaOH) = 5.0 mM, anaerobic conditions. Down: normalized UV-vis spectra of Mn(II)TTEG–NO and the intermediate of the reaction Mn(III)TTEG + HU recorded 150 s after mixing. c_0(Mn(III)TTEG) = 3.75 μM, c_0(HU) = 150 μM, pH 11.70, $c_0(O_2)$ = 254 μM, I = 1.0 M, T = 25.0 °C.

that of the major intermediate of the reaction (with an A_{max} at 430 nm).

The reaction was also monitored with ESI-MS from ca. 50 s after mixing. The time resolved +ESI-MS spectra of the reaction mixture were compared to the spectra of independently prepared Mn(III)TTEG, Mn(II)TTEG and Mn(II)TTEG–NO solutions. Table 2 shows some identified peaks corresponding to Mn(III)TTEG, Mn(II)TTEG and Mn(II)TTEG–NO. The intensity of the ESI-MS signal of Mn(III)TTEG increases, and the intensities of the signals of Mn(II)TTEG and Mn(II)TTEG–NO decrease in the reaction mixture from 50 s to 400 s after mixing (Figure 7). The +ESI-MS spectrum of the product solution (60 min after

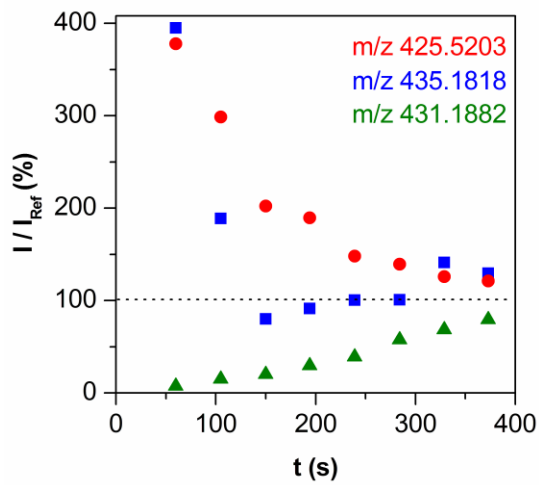

Figure 7. The change of the +ESI-MS signal intensities of Mn(III)TTEG (*m/z* 431.1882), Mn(II)TTEG (*m/z* 425.5203) and Mn(II)TTEG–NO (*m/z* 435.1818) during the reaction of Mn(III)TTEG and HU. The intensities are given in percentage of the measured intensities in a reference solution of Mn(III)TTEG under identical conditions. c_0(Mn(III)TTEG) = 10.0 μM, c_0(HU) = 49.5 μM, pH 10.70, $c_0(O_2)$ = 254 μM, T = 25.0 °C.

Table 2. The identified major +ESI-MS species corresponding to Mn(III)TTEG, Mn(II)TTEG and Mn(II)TTEG–NO. Only the most abundant isotopic peaks are shown in the table.

		m/z	
species	**formula**	**measured**	**calculated**
(Mn(III)TTEG) +2OH$^-$	$C_{68}H_{86}N_8O_{14}Mn^{3+}$	431.1882	431.1876
(Mn(III)TTEG) –H$^+$ +OH$^-$	$C_{68}H_{84}N_8O_{13}Mn^{3+}$	425.1828	425.1841
(Mn(III)TTEG) –2H$^+$	$C_{68}H_{82}N_8O_{12}Mn^{3+}$	419.1799	419.1805
(Mn(II)TTEG) +OH$^-$	$C_{68}H_{85}N_8O_{13}Mn^{3+}$	425.5203	425.5200
(Mn(II)TTEG) –H$^+$	$C_{68}H_{83}N_8O_{12}Mn^{3+}$	419.5144	419.5165
(Mn(II)TTEG-NO) –H$^+$ +OH$^-$	$C_{68}H_{84}N_9O_{14}Mn^{3+}$	435.1818	435.1834
(Mn(II)TTEG-NO) –2H$^+$	$C_{68}H_{82}N_9O_{13}Mn^{3+}$	429.1778	429.1799

mixing Mn(III)TTEG and HU) shows the presence of only Mn(III)TTEG. The quantitative evaluation of the recorded time traces are challenging because the relative sensitivity of the MS instrument slightly changes for each species with the changing composition of the analyte solution. Because of this phenomenon, our MS method was not suitable for monitoring the reaction quantitatively, only the major trends in the changes of concentrations could be detected. It should also be noted that the MS experiments were carried out under conditions that were slightly different from the rest of the kinetic measurements to avoid complications from the high ionic strength.

Based on IC measurements, we found that HU is quantitatively converted to NO_2^- in the Mn(III)TTEG + HU reaction, and the produced NO_2^- undergoes slow autoxidation ($t_{½} \approx 200$ min) to give NO_3^-.

5.2.4) *Effect of reactant concentrations*

The concentration dependence of the reaction was studied by varying the concentration ratio of Mn(III)TTEG to HU from 1 : 0.2 to 1 : 30. First, the experimental kinetic results were evaluated by the initial rate method. The v_0^{430nm} versus initial concentration curves saturate at high relative concentrations of either Mn(III)TTEG or HU in the pH range from 10.7 to 12.7 (Figure 8). If we assume the formation of a reactive adduct (Mn(III)TTEG–HU) from the reactants in a fast pre-equilibrium, with the same mathematical derivation as seen in an earlier literature example,[159] we get:

$$v_0^{430nm} = k_0^{430nm}[\mathrm{Mn^{III}TTEG–HU}]_0 \quad \text{and} \quad K_0 = \frac{[\mathrm{Mn^{III}TTEG–HU}]_0}{[\mathrm{Mn^{III}TTEG}]_0[\mathrm{HU}]_0} \tag{8}$$

$$v_0^{430nm} = \frac{k_0^{430nm}}{2}\left(c_0(\mathrm{Mn^{III}TTEG}) + c_0(\mathrm{HU}) + K_0^{-1}\right) - \frac{k_0^{430nm}}{2}\sqrt{\left(c_0(\mathrm{Mn^{III}TTEG}) + c_0(\mathrm{HU}) + K_0^{-1}\right)^2 - 4c_0(\mathrm{Mn^{III}TTEG})c_0(\mathrm{HU})} \tag{9}$$

where k_0^{430nm} is a wavelength dependent rate constant, K_0 is the equilibrium constant of the adduct formation and the c_0 symbol indicates initial analytical concentrations of the reactants. The protonation state of HU and Mn(III)TTEG changes in the studied pH range, therefore, both k_0^{430nm} and K_0 are pH dependent. Eq. 9 fits to the v_0^{430nm} versus initial concentration curves, and the constants are

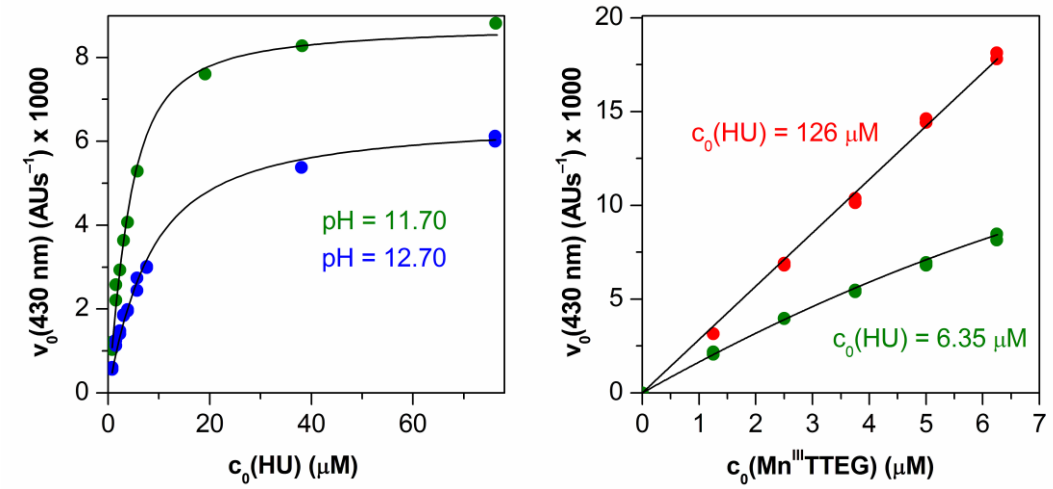

Figure 8. Left panel: dependence of the initial reaction rate on the relative initial concentrations of the Mn(III)TTEG and HU reactants at different pH values. Dots: measured values, lines: fitted curves on the basis of eq. 9. c_0(Mn(III)TTEG) = 3.75 μM, c_0(HU) = from 0.763 μM to 114 μM, $c_0(O_2)$ = 254 μM, I = 1.0 M, T = 25.0 °C. Right panel: the same as left, but, the initial concentration of Mn(III)TTEG was varied while that of HU was kept constant. Dots: measured values, lines: fitted curves. c_0(Mn(III)TTEG) = from 1.25 μM to 6.25 μM, pH 11.70, $c_0(O_2)$ = 254 μM, I = 1.0 M, T = 25.0 °C.

estimated to be the following: k_0^{430nm} = (2.34 ± 0.03) × 10^3 AU M^{-1} s^{-1} and K_0 = (4.1 ± 0.2) × 10^5 M^{-1} at pH 11.70. Stopped-flow measurements with PDA detection proved that the spectrum of the reaction mixture at 100 ms after mixing slightly differs from the sum of the spectra of the reactants. However, the measured effect was too small to be reliably measured and quantified.

The effect of the variation of the initial concentration of dissolved O_2 has been also studied in detail. At constant initial concentrations of Mn(III)TTEG and HU, with HU in high excess v_0^{430nm} reaches a saturation value by increasing $c_0(O_2)$ (Figure 9). Extrapolation to $c_0(O_2)$ = 0 indicates a non-zero reaction rate, which can be interpreted by considering an alternative mechanism under anaerobic conditions (vide infra).

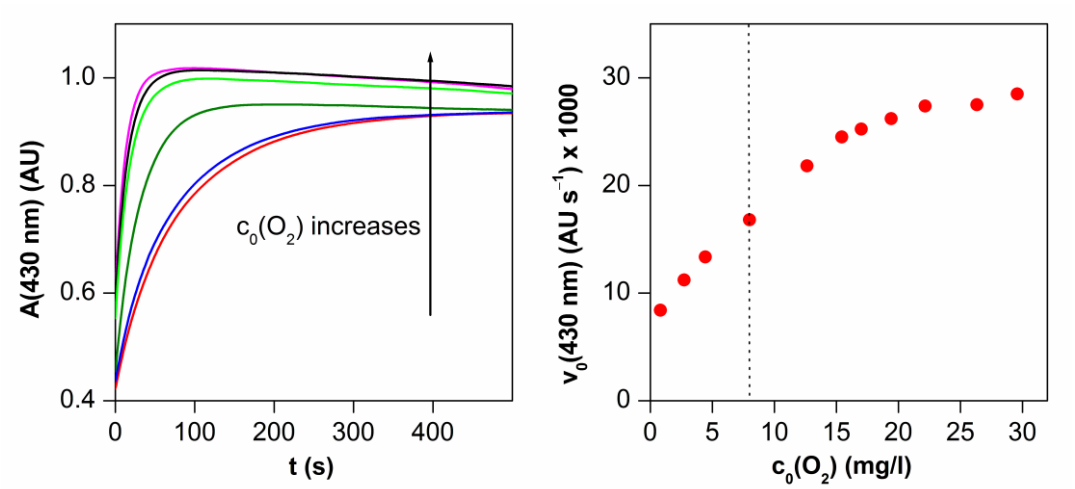

Figure 9. Left panel: kinetic curves recorded at different initial concentrations of dissolved O_2. The initial concentrations of Mn(III)TTEG and HU were kept constant. Right panel: dependence of the initial reaction rate on the initial concentration of O_2. The dotted line indicates the solution saturated with air at atmospheric pressure. c_0(Mn(III)TTEG) = 4.98 μM, c_0(HU) = 101 μM, pH 11.70, $c_0(O_2)$ = from 0.81 mg/L to 7.99 mg/L, I = 1.0 M, T = 25.0 °C.

5.2.5) *Kinetic model and characteristics of the reaction system*

The kinetic model proposed for the Mn(III)TTEG catalyzed autoxidation of HU is summarized in Scheme 3. A more visualized version of the mechanism is shown in Scheme 4. This model provides coherent mechanistic interpretation of the experimental observations in this system at pH 11.70 and, as will be shown later, can also be used with some additions in the pH range from 9 to 13. The overall reaction is initiated by the axial coordination of HU to Mn(III)TTEG (R4, R5). The reversible formation of this adduct is consistent with the noted feature of the initial rate (v_0^{430nm}) with increasing initial concentrations of either reactants. At pH 11.70, the substitution of the axially coordinated OH^- with deprotonated HU is assumed on the Mn(III) center, resulting in a Mn–N(=O)– coordination.[76] The approach to equilibrium between Mn(III)TTEG and Mn(III)TTEG–HU is assumed to be fast as the initial UV-vis spectrum of the reaction mixture recorded 100 ms after mixing is dependent on the initial reactant concentrations. After an electron transfer from HU to the Mn(III) center, the Mn(III)TTEG–HU adduct may dissociate into Mn(II)TTEG and $HU^{\bullet}$ radical (R6). The $HU^{\bullet}$ radical can be afterwards oxidized by O_2 to NO and HNO (R12 and R13).[72,73,154,155] The reactions of NO and HNO with

Scheme 3. Proposed kinetic model for the reaction of Mn(III)TTEG with HU at pH 11.70. Mn(III)TTEG is abbreviated $Mn^{III}P$, and the intermediates consequently. The charges and the protonation states are not indicated in the symbolism. *k*: rate constants. *E*: molar absorbances at 430 nm. (Underlined: detailed kinetics are given in the literature, see the citations in text. Asterix: constants fixed during the fitting procedure.)

R4	$Mn^{III}P + HU \rightarrow (Mn^{III}P–HU)$	$^{*}k_4 = 1.0 \times 10^9\ M^{-1}s^{-1}$
R5	$(Mn^{III}P–HU) \rightarrow Mn^{III}P + HU$	$k_5 = (8.5 \pm 0.3) \times 10^3\ s^{-1}$
R6	$(Mn^{III}P–HU) \rightarrow Mn^{II}P + HU\cdot$	$k_6 = (4.8 \pm 0.1) \times 10^{-2}\ s^{-1}$
R7	$2(Mn^{III}P–HU) + O_2 \rightarrow 2(Mn^{II}P–NO)$	$k_7 = (4.6 \pm 0.1) \times 10^1\ M^{-1}s^{-1}$
R8	$(Mn^{II}P–NO) \rightarrow Mn^{II}P + NO$	$\underline{k}_8 = (8.8 \pm 0.3) \times 10^0\ s^{-1}$
R9	$Mn^{II}P + NO \rightarrow (Mn^{II}P–NO)$	$^{*}\underline{k}_9 = 1.0 \times 10^9\ M^{-1}s^{-1}$
R10	$4(Mn^{II}P–NO) + O_2 \rightarrow 4Mn^{II}P + 4NO_2^-$	$k_{10} = (9.0 \pm 0.1) \times 10^{-1}\ M^{-1}s^{-1}$
R11	$4Mn^{II}P + O_2 \rightarrow Mn^{III}P$	$k_{11} = (1.9 \pm 0.3) \times 10^1\ M^{-1}s^{-1}$
R12	$2HU\cdot + O_2 \rightarrow 2NO$	$k_{12} = (6.2 \pm 0.3) \times 10^0\ M^{-1}s^{-1}$
R13	$4HU\cdot + O_2 \rightarrow 4HNO$	$k_{13} = (6.0 \pm 0.3) \times 10^1\ M^{-1}s^{-1}$
R14	$Mn^{III}P + HNO \rightarrow (Mn^{II}P–NO)$	$^{*}\underline{k}_{14} = 5.0 \times 10^4\ M^{-1}s^{-1}$
R15	$2HNO + O_2 \rightarrow 2NO_2^-$	$^{*}\underline{k}_{15} = 1.0 \times 10^9\ M^{-1}s^{-1}$
R16	$HNO + 2NO \rightarrow NO_2^- + N_2O$	$^{*}\underline{k}_{16} = 4.0 \times 10^6\ M^{-1}s^{-1}$
R17	$2HNO \rightarrow N_2O$	$^{*}\underline{k}_{17} = 8.0 \times 10^6\ M^{-1}s^{-1}$
R18	$4NO + O_2 \rightarrow 4NO_2^-$	$^{*}\underline{k}_{18} = 2.1 \times 10^6\ M^{-2}s^{-1}$
R19	$4HU + O_2 \rightarrow 4HU\cdot$	$^{*}k_{19} = 2.0 \times 10^0\ M^{-1}s^{-1}$
	$Mn^{III}P$	$^{*}E_1 = 80700\ M^{-1}cm^{-1}$
	$[Mn^{III}P–HU]$	$E_2 = 85600 \pm 500\ M^{-1}cm^{-1}$
	$Mn^{II}P$	$^{*}E_3 = 75000\ M^{-1}cm^{-1}$
	$[Mn^{II}P–NO]$	$E_4 = 219600 \pm 300\ M^{-1}cm^{-1}$

Mn(II) and Mn(III) macrocyclic systems have been described earlier.[29,30] We propose that NO and HNO will eventually give Mn(II)TTEG–NO, the former reacting with Mn(II)TTEG (R9) and the latter with Mn(III)TTEG (R14).[76,130] Similar findings are reported with strongly electron-accepting Fe(II) porphyrins.[160] Mn(II)TTEG–NO can alternatively be produced in the autoxidation of Mn(III)TTEG–HU (R7). As described in the literature,[74,75,161] NO and HNO will rapidly react with each other (R16, R17) or with O_2 (R15, R18) to give N_2O and/or

NO_2^-. The autoxidation of Mn(II)TTEG (R11) plays an important role: R11 replenishes Mn(III)TTEG. Therefore, the overall course of the reaction Mn(III)TTEG + HU is closed into a catalytic cycle in which the autoxidation of HU is catalyzed by Mn(III)TTEG. The slow uncatalyzed autoxidation of HU yielding a $HU^{\bullet}$ radical (R19) was also taken into account in the calculations.

Scheme 4. Proposed kinetic model for the catalytic autoxidation of HU.

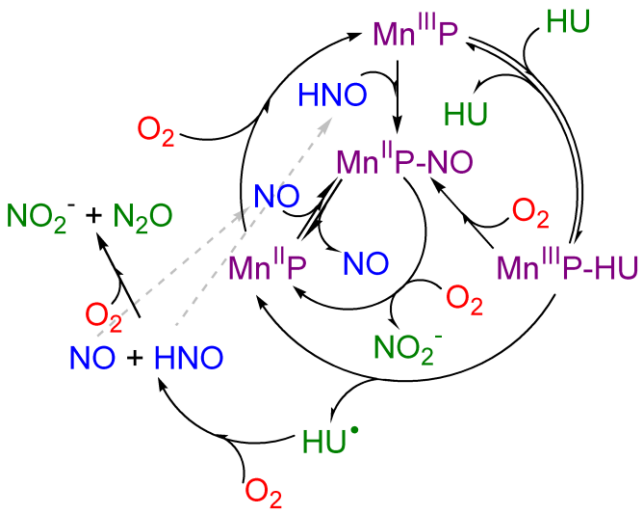

A global data fit[162] using the kinetic model in Scheme 3 was performed with some rate constants and molar absorbances held fix: k_9, k_{14}, k_{15}, k_{16}, k_{17}, k_{18} (literature values);[76,130,74,75,161] k_4, k_{19}, E_1, E_3 (determined or approximated independently). Eleven kinetic curves were fitted globally in the relative initial concentration range of Mn(III)TTEG : HU from 1 : 0.2 to 1 : 30 at pH 11.70. The depletion of the dissolved O_2 during the reaction was taken into account. As seen in Figure 10, the results are satisfactory; the estimated values of the rate constants and molar absorbances are listed in Scheme 3.

The presence of an anaerobic mechanism is suggested for the formation of Mn(II)TTEG-NO by the nonzero reaction rate at $c_0(O_2) \approx 0$. The anaerobic formation of NO and/or HNO from $HU^{\bullet}$ were, however, excluded from the detailed kinetic model because the corresponding reaction steps proved to be negligible during the global fitting procedure to the aerobic experiments. The significance of

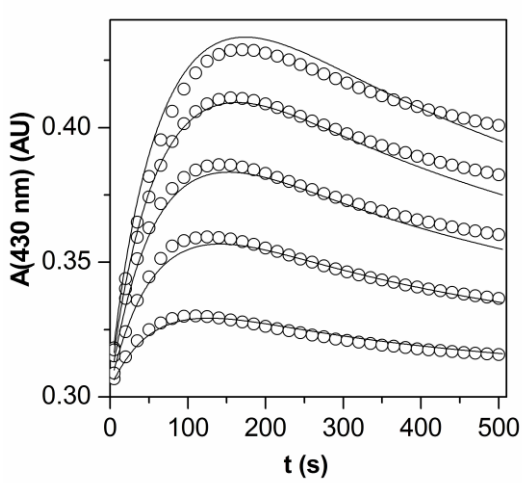

Figure 10. Representative experimental kinetic curves (circles) of the reaction of Mn(III)TTEG and HU and the corresponding simulation (lines) using the kinetic model from Scheme 3. (Only 5% of the experimental data points are shown.) c_0(Mn(III)TTEG) = 3.75 μM, c_0(HU) = from 0.76 μM to 5.71 μM, pH 11.70, $c_0(O_2)$ = 254 μM, I = 1.0 M, T = 25.0 °C.

these pathways could be mapped by collecting concentration dependence data under anaerobic conditions and globally fitting them to the extended kinetic model.

The thermodynamic stability of the complexes Mn(III)TTEG–HU and Mn(II)TTEG-NO are high with apparent stability constants of $k_4/k_5 = 1.2 \times 10^5\ M^{-1}$ and $k_9/k_8 = 1.1 \times 10^8\ M^{-1}$, respectively. The value of the stability constant of Mn(III)TTEG–HU calculated from the results of the global fit is lower than that of determined by fitting the initial rates to eq. 9 ($K_0 = 4.1 \times 10^5\ M^{-1}$). This contradiction can be resolved by considering reaction R11, which can be relevant in replenishing the concentration of Mn(III)TTEG even in the initial part of the catalytic cycle. Thus, the stability constant measured by the initial rate method cannot be attributed to only a single equilibrium and the pre-equilibrium approximation overestimates the relevant equilibrium constant. The intermediate Mn(III)TTEG–HU is consumed by two reactions, the electron transfer reaction R6 and the autoxidation R7. When $c(O_2) \approx 2.5 \times 10^{-4}$ M during the reaction, $c(O_2) \times k_{10} \approx 2.3 \times 10^{-4}\ s^{-1}$, which is two orders of magnitude lower than k_6. Because the autoxidation of the $HU^{\bullet}$ radical formed in R6 is also fast, the ligand-to-metal electron transfer reaction R6 is assumed to be a major pathway for the catalytic oxidation of HU. Kinetic simulations show that the formation of HNO in

the autoxidation of HU radical is faster than the formation of NO, although the accumulation of HNO cannot occur because of its fast subsequent autoxidation (R15) and dimerization (R17). Consequently, the majority of Mn(II)TTEG–NO is produced by the reaction of Mn(II)TTEG + NO (R9) and not in the reaction of Mn(III)TTEG + HNO (R14). Similar mechanistic conclusions were drawn in the study on the reactions of analogous Mn(III) porphyrins with NO- and HNO-donor reactants.[76] The rate constants describing the two ways of oxidation of the HU radical with O_2 (k_{12}, k_{13}) were determined indirectly in this study for the first time and seem to be reasonable compared to previous reports on the reactivity of HU radical.[163,164]

Another important feature of the reaction between Mn(III)TTEG and HU is that the concentration of the free NO remains low during the whole course of the process, because of the high thermodynamic stability of Mn(II)TTEG–NO. The photochemical release of the coordinated NO from Mn(II)–NO porphyrins analogous to Mn(II)TTEG–NO was reported previously.[165] Therefore, under intensive illumination (e.g. with the lamp of a diode array photometer), the decreasing lifetime of the Mn(II)TTEG–NO intermediate of the reaction is not unexpected. The novelty of our measurements is that we were able to investigate the photoreaction in simple spectrophotometers using them simultaneously as photoreactors and detectors.[156]

5.2.6) *pH dependence*

The pH dependence of the reaction has been studied in the range of pH from 9.1 to 12.7 at high excess of HU over Mn(III)TTEG (where v_0^{430nm} is independent of c_0(HU)). Moving further down with the pH results in very small absolute change in the absorbance signals, which was difficult to measure reliably. It is reasonable to assume that after the fast formation of the Mn(III)TTEG–HU adduct, only one pseudo-first order reaction takes place in the initial 10% of the overall process where the decomposition of the Mn(II)TTEG–NO intermediate is negligibly slow compared to its formation:

$$\text{Mn(III)TTEG–HU} \rightarrow \text{Mn(II)TTEG–NO} \quad k_{obs} \qquad (R_{init})$$

Quantitative comparison of the kinetic experiments recorded at different pH values is complicated without approximations because the absorbing reactants, and

presumably the intermediates, have at least one pK_a in the studied pH range. Proton exchange reactions between the corresponding acid–base pairs are presumably diffusion controlled and can be treated as fast pre-equilibria. The deprotonation of the axially coordinated water molecule of Mn(III)TTEG–HU and Mn(II)TTEG–NO can be described with the constants K_{a6} and K_{a7}, respectively:

$$\text{Mn(III)TTEG–HU} \rightleftharpoons \text{(Mn(III)TTEG–HU)H}_{-1} + \text{H}^+$$

$$K_{a6} = \frac{[(\text{Mn}^{\text{III}}\text{TTEG–HU})\text{H}_{-1}][\text{H}^+]}{[\text{Mn}^{\text{III}}\text{TTEG–HU}]} \tag{10}$$

$$\text{Mn(II)TTEG–NO} \rightleftharpoons \text{(Mn(II)TTEG–NO)H}_{-1} + \text{H}^+$$

$$K_{a7} = \frac{[(\text{Mn}^{\text{II}}\text{TTEG–NO})\text{H}_{-1}][\text{H}^+]}{[\text{Mn}^{\text{II}}\text{TTEG–NO}]} \tag{11}$$

At a given pH, the kinetic traces can be interpreted based on R_{init}:

$$A^{430\text{nm}} = E_{\text{I}} c_0 \exp(-k_{\text{obs}} t) + E_{\text{II}} c_0 \left(1 - \exp(-k_{\text{obs}} t)\right) \tag{12}$$

where E_{I} and E_{II} are the pH dependent molar absorbances at 430 nm of Mn(III)TTEG–HU and Mn(II)TTEG–NO, respectively, k_{obs} is the pH dependent pseudo-first order rate constant and c_0 is the initial Mn(III)TTEG concentration. Fitting the first 10% of the experimental kinetic curves to eq. 12 gives the values of E_{I}, E_{II} and k_{obs}. The pH dependent values of these parameters are shown in Figure 11. The pH dependencies of the molar absorbances, E_{I}, E_{II}, are given by eq. 13:

$$E_{\text{I}} = \frac{E_{\text{I}}^{\text{prot}}[\text{H}^+] + E_{\text{I}}^{\text{deprot}} K_{a6}}{[\text{H}^+] + K_{a6}} \quad \text{and} \quad E_{\text{II}} = \frac{E_{\text{II}}^{\text{prot}}[\text{H}^+] + E_{\text{II}}^{\text{deprot}} K_{a7}}{[\text{H}^+] + K_{a7}} \tag{13}$$

where E_{prot} and $E_{d\text{eprot}}$ are the molar absorbances at 430 nm of the corresponding protonated and deprotonated species, respectively, and K_a is the deprotonation constant. k_{obs} can be fitted to the following expression:

$$k_{\text{obs}} = \frac{k_{\text{obs}}^{0\text{H}} + k_{\text{obs}}^{1\text{H}} \frac{[\text{H}^+]}{K_{a7}} + k_{\text{obs}}^{2\text{H}} \frac{[\text{H}^+]^2}{K_{a6}K_{a7}}}{1 + \frac{[\text{H}^+]}{K_{a7}} + \frac{[\text{H}^+]^2}{K_{a6}K_{a7}}} \tag{14}$$

where k^{0H}_{obs}, k^{1H}_{obs} and k^{2H}_{obs} are the rate constants for the 3 different possible protonation states of the initial reaction R_{init} (deprotonated adduct and intermediate, protonated adduct or intermediate, protonated adduct and intermediate, respectively). As seen in Figure 11, simultaneous fitting of the 3 curves (ε_I, ε_{II} and k_{obs} versus pH) to eqs. 13 and 14 yields reasonably good results. The studied initial reaction is the fastest in the intermediate protonation state when only either Mn(III)TTEG–HU or Mn(II)TTEG–NO is protonated. The constants E_I^{deprot} = 85000 ± 2000 $M^{-1}cm^{-1}$ and E_{II}^{deprot} = 221000 ± 6000 $M^{-1}cm^{-1}$ are in good agreement with E_2 and E_4, the calculated molar absorbances of Mn(III)TTEG–HU and Mn(II)TTEG–NO at pH 11.70 (see Scheme 3). Thus, the global approach utilized to deduce the detailed kinetic model at pH 11.70 is consistent with the results of the pH dependence study. The deprotonation constant of the axially coordinated water molecules of Mn(III)TTEG–HU and Mn(II)TTEG–NO are calculated to be $pK_{a6} < 9.0$ and $pK_{a7} = 11.4 \pm 0.4$, respectively.

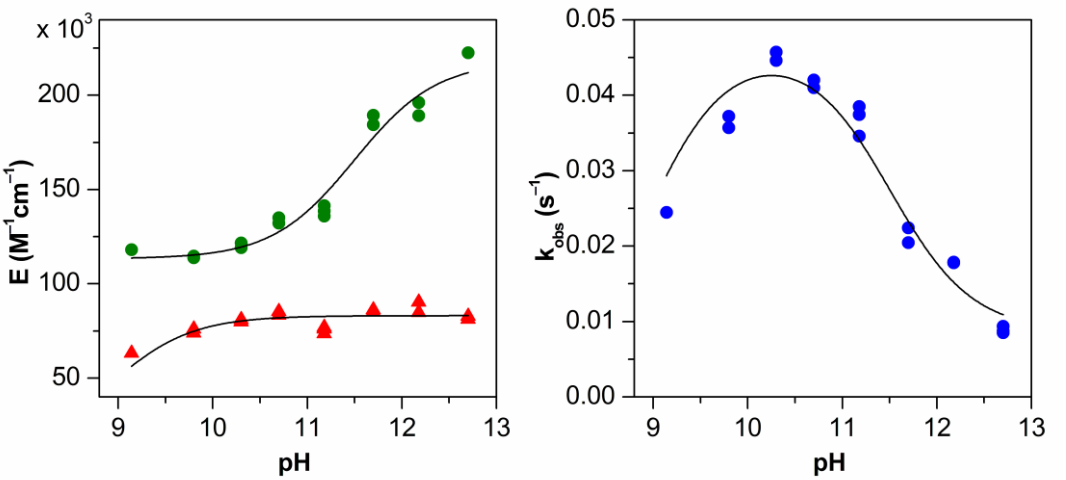

Figure 11. Left panel: pH dependence of the calculated molar absorbances of Mn(III)TTEG–HU (triangles) and Mn(II)TTEG–NO (dots) in the initial part of the reaction of Mn(III)TTEG and HU (in borate buffer and NaOH solutions). Right panel: pH dependence of the pseudo-first order rate constant of formation of Mn(II)TTEG–NO in the initial part of the reaction. Solid lines represent fitted results as discussed in the text. c_0(Mn(III)TTEG) = 2.04 μM, c_0(HU) = 15.3 μM, c(buffer) = from 0.80 mM to 7.5 mM, $c_0(O_2)$ = 254 μM, I = 1.0 M T = 25.0 °C.

5.3) The oxidation of SCN^- by HSO_5^-

5.3.1) *Experiments at pH 13*

For the sake of simplicity, we studied the reaction of HSO_5^- with SCN^- at pH 13.5 first, where HSO_5^- is fully deprotonated ($pK_a(HSO_5^-)$ = 8.35 at I = 1.0 M [110]), and hypothiocyanite ($OSCN^-$), the expected product of an oxygen transfer to SCN^-, is stable for hours.[137] We studied the reaction under high excess of SCN^- ($[SCN^-]_0$ = 50.0 mM – 500 mM) over SO_5^{2-} ($[KHSO_5]_0$ = 5.0 mM). The reaction is complete in a few seconds under the conditions applied and additional kinetic effects are not observed on longer timescales. Kinetic traces were recorded at various wavelengths in the range of 350 – 500 nm (Figure 12) and analyzed by singular value decomposition analysis (Table 3) in order to determine the number of absorbing species in the system.[157,158] Based on the mathematical evaluation, we found that the increase in absorbance during the reaction at around 375 nm can be attributed to the formation of a single species, no absorbing intermediates were detected. The observed product was unambiguously identified as $OSCN^-$ with an A_{max} at 376 nm.[134] $OSCN^-$ was also detected in the reaction mixture with ESI-MS. In subsequent experiments, the kinetic curves were exclusively recorded at 376 nm, where neither the reactants nor other products contribute to the absorbance.

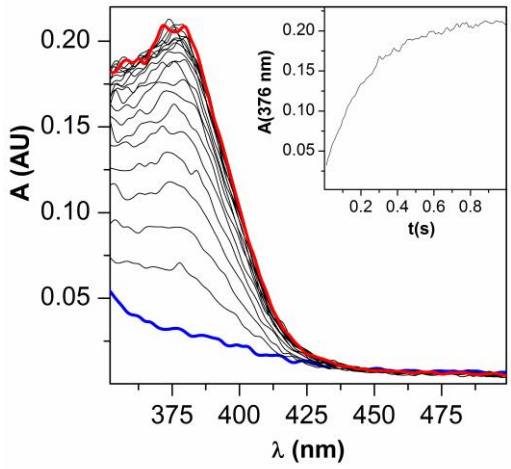

Figure 12. UV-vis spectral change recorded in the SO_5^{2-} + SCN^- reaction system at pH 13.5. The absorbance maximum at 376 nm is characteristic of $OSCN^-$. The first (blue) and last (red) spectra are highlighted. Inset: kinetic curve recorded at 376 nm. $[KHSO_5]_0$ = 5.0 mM, $[NaSCN]_0$ = 500 mM, pH 13.5, I = 1.0 M, T = 25.0 °C.

Table 3. The first 5 singular values of the time-resolved UV-vis absorbance matrices of the $(H)SO_5^-$ + SCN^- reaction system, recorded under the given conditions. According to references 157 and 158, only the first value belongs to real signal in every case, the other non-zero values represent noise.

pH 6.84 5.0 mM HSO_5^- 50 mM SCN^-	pH 6.84 5.0 mM HSO_5^- 500 mM SCN^-	pH 13.5 5.0 mM SO_5^{2-} 50 mM SCN^-	pH 13.5 5.0 mM SO_5^{2-} 500 mM SCN^-
SV	**SV**	**SV**	**SV**
2.201	3.100	5.407	7.770
0.081	0.111	0.313	0.182
0.042	0.059	0.072	0.067
0.039	0.056	0.068	0.058
0.026	0.036	0.031	0.045

All kinetic traces (Figure 13 left panel) can be fitted to a single exponential function within the precision of the experimental data ($R^2 > 0.98$) and show the following characteristics: the final absorbance readings reach a limiting value by increasing $[SCN^-]_0$, and the experimental pseudo-first order rate constant (k_{obs}) is linearly dependent on $[SCN^-]_0$ with non-zero intercept (Figure 13 left panel). At high SCN^- excess, $OSCN^-$ is produced following a 1 : 1 $OSCN^-$ to SO_5^{2-} stoichiometry. From the highest final absorbance $[OSCN^-]_{max} = 5.1$ mM was calculated using the literature value of the molar absorbance of $OSCN^-$ at 376 nm ($26.5\ M^{-1}cm^{-1}$).[134] Phenomenologically, such observations can be explained by an equilibrium reaction between the reactants (R1), which is pseudo-first order in both directions[166] (these conditions are fulfilled because SCN^- and SO_4^{2-} were in large excess[167] over the limiting reagents):

$$SO_5^{2-} + SCN^- \rightleftharpoons SO_4^{2-} + OSCN^- \qquad (R1)$$

A similar equilibrium ($R1^H$) was proposed previously in the kinetic model of the reaction of SCN^- + HSO_5^- under acidic conditions.[113,114] However, considering that the backward reaction of R1 is hardly feasible thermodynamically,[168] and that the kinetics of the SO_5^{2-} + SCN^- reaction system proved to be indifferent to the change

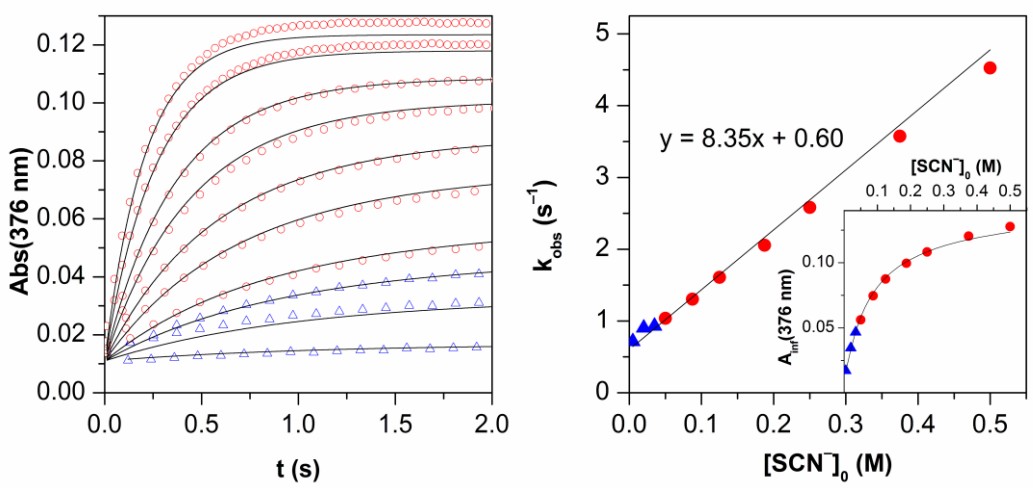

Figure 13. The reaction of SCN^- with SO_5^{2-} at pH 13.5. Left panel: experimental pseudo-first order kinetic curves, only 5 % of the recorded points are shown for clarity. Right panel: pseudo-first order rate constant as a function of the initial SCN^- concentration. Inset: the final absorbance at 376 nm as a function of the initial SCN^- concentration. The symbols are the same for the two panels: Dots: experimental points with SCN^- in high excess. Triangles: comparable $[SCN^-]_0$ and $[SO_5^{2-}]_0$. Lines: result of global fit to the kinetic model of Scheme 5. $[KHSO_5]_0$ = 5.0 mM, $[NaSCN]_0$ = from 5.0 mM to 500 mM, pH 13.5, I = 1.0 M, T = 25.0 °C.

in $[SO_4^{2-}]_0$, the existence of equilibrium R1 is definitely ruled out. An alternative kinetic model was constructed, keeping in mind that the rate of oxidation of $OSCN^-$ by peroxo compounds is expected to be about the same order of magnitude as the rate of oxidation of SCN^-.[79,81,94] In the kinetic model shown in Scheme 5, SCN^- and its first-step oxidation product $OSCN^-$ are competing for the remaining SO_5^{2-} in reactions R20 and R21, in order. With an increasing excess of SCN^-, the relative rate of the oxidation of $OSCN^-$ decreases, thus the surviving amount of $OSCN^-$ increases. The stoichiometry of the production of $OSCN^-$ becomes 1 : 1 ($OSCN^-$ to SO_5^{2-}) at high $[SCN^-]_0$. The oxidation product of $OSCN^-$ (i.e., O_2SCN^-) is known to decompose in fast reactions (R22–R25, adopted from the literature[115,119]) to yield the final mixture of stable anions: SO_4^{2-}, SO_3^{2-}, CN^- and OCN^-.[95,115,119] The production of SO_4^{2-}, CN^- and OCN^- during the oxidation of SCN^- by HSO_5^- at acidic pH has been described earlier.[112] The presence of CN^- and OCN^- in the basic SCN^- + SO_5^{2-} reaction mixture was verified by ESI-MS. As detailed later in the thesis, SO_3^{2-} is the decomposition product of $OSCN^-$ at neutral

pH. The experimental kinetic data set recorded at pH 13.5 can be fitted globally to the kinetic model of Scheme 5 utilizing the ZiTa software and assuming that both R20 and R21 are first order for each species involved. The actual rates of reactions R22 and R23 are considered to be comparable and much faster than those of the rate determining steps (R20 and R21) over the entire course of the reaction, thus, not affecting the stoichiometry of the depletion of $OSCN^-$. The fit is excellent even at comparable initial concentrations of SCN^- and SO_5^{2-} (Figure 13). The calculated rate constants are $k_{20} = 8.08 \pm 0.02\ M^{-1}\ s^{-1}$ and $k_{21} = 164.8 \pm 0.5\ M^{-1}\ s^{-1}$.

Scheme 5. Kinetic model for the oxidation of SCN^- by SO_5^{2-}. Valid around pH 13. Although $k_{20} << k_{21}$, at high concentrations of SCN^-, the first oxidation step (R20) can compete with the faster second step (R21), thus $OSCN^-$ can accumulate. Reaction steps marked with italic numbers (*R22*, *R23*, *R24* and *R25*) are adopted from the literature[115,119] and assumed to be much faster than R20 and R21.

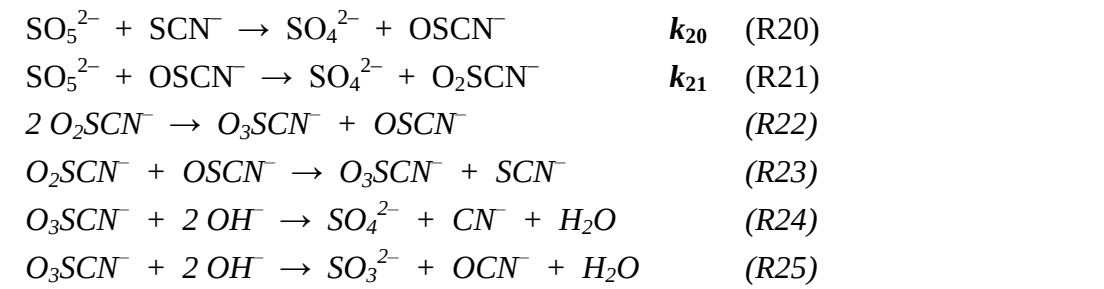

A derivation on the basis of the system of simultaneous differential equations defined by Scheme 5 yields the following approximate expression for the concentration change of $OSCN^-$ as a function of time:

$$[OSCN^-] = \frac{k_{20}[SCN^-][SO_5^{2-}]_0}{k_{20}[SCN^-] + k_{21}[SO_5^{2-}]_0}\left(1 - \exp\left(-(k_{20}[SCN^-] + k_{21}[SO_5^{2-}]_0)t\right)\right) \qquad (15)$$

Although Scheme 5 does not predict a simple first order kinetic trace in a strict mathematical sense, eq. 15 implies that the actual solution is close to an exponential curve with a pseudo-first order rate constant $k_{obs} = k_{21}[SO_5^{2-}]_0 + k_{20}[SCN^-]_0$. This explains why the kinetic traces can be fitted to a simple first-order expression with reasonable accuracy. The k_{obs} versus $[SCN^-]_0$ plot in Figure 13 (right panel) can be fitted to $k_{obs} = m[SCN^-]_0 + a$ acceptably, yielding $m =$

$8.351 \pm 0.001\ M^{-1}\ s^{-1}$ and $a = 0.601 \pm 0.001\ s^{-1}$ at constant $[SO_5^{2-}]_0 = 5.0$ mM. A comparison with eq. 15 gives $k_{20} = 8.35\ M^{-1}\ s^{-1}$ and $k_{21} = 120\ M^{-1}\ s^{-1}$. These rate constants are in good agreement with those estimated by globally fitting the experimental data set to the kinetic model of Scheme 5 without approximations. These results lend further support to the kinetic model proposed in Scheme 5.

5.3.2) *Experiments at pH 7*

The HSO_5^- + SCN^- reaction has been also studied in detail at pH 6.89, where the singly protonated form of the oxidant, HSO_5^-, is predominant over SO_5^{2-}, but $OSCN^-$ is still deprotonated (pK_a(HOSCN) = 4.93 at $I = 1.0$ M [95]). In the first 100 ms after mixing the reactants, the kinetic behavior of the reaction is similar to that observed at pH 13.5 (Figure 14). Thus, the findings can be interpreted using the kinetic model of Scheme 5 by replacing SO_5^{2-} with HSO_5^-:

$HSO_5^- + SCN^- \rightarrow SO_4^{2-} + OSCN^- + H^+$ $\quad \boldsymbol{k_{20}^H}$ $\quad$ (R20^H)

$HSO_5^- + OSCN^- \rightarrow SO_4^{2-} + O_2SCN^- + H^+$ $\quad \boldsymbol{k_{21}^H}$ $\quad$ (R21^H)

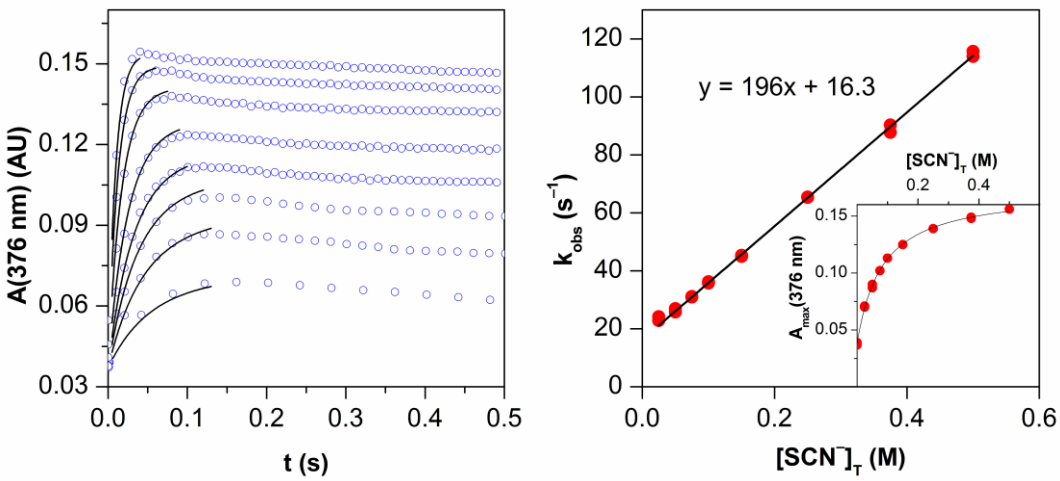

Figure 14. The reaction of SCN^- with HSO_5^- at pH 6.89. Left panel: experimental kinetic curves. Two kinetically separated phases are shown (a third slower step is not included in the figure). The faster process can be described with the kinetic model of Scheme 5. Right panel: pseudo-first order rate constant as a function of the initial SCN^- concentration. Inset: the extrapolated final absorbance at 376 nm as a function of the initial SCN^- concentration. Dots: experimental points. Lines: results of the global fit of the first part of the kinetic traces to the kinetic model of Scheme 5. $[KHSO_5]_0 = 5.0$ mM, $[NaSCN]_0$ = from 25 mM to 500 mM, pH 6.89, I = 1.0 M, T = 25.0 °C.

The values of the rate constants have been estimated by globally fitting the first part of the kinetic curves with ZiTa: k_{20}^{H} =203 ± 1 M^{-1} s^{-1} and k_{21}^{H} = (3.44 ± 0.03) × 10^3 M^{-1} s^{-1} (Figure 14). On a longer timescale (> 100 ms), two additional kinetically independent reaction steps are observed. The second process (Figure 14) is characterized by a small decrease in absorbance at 376 nm in a few seconds, and according to matrix rank analysis of the multiwavelength measurements (Table 3), it does not involve the formation of any new absorbing species. A semi-quantitative observation was made, that the amplitude of the absorbance change during the second process significantly decreases with increasing $[SCN^-]_0$ and even vanishes at high $[SCN^-]_0$. This phenomenon makes the quantitative description of this reaction step challenging, but on the other hand, leads to the assumption that the second process is probably attributed to the reaction of $OSCN^-$ with CN^-:

$$CN^- + OSCN^- \rightarrow\rightarrow OCN^- + SCN^- \qquad \text{(R26)}$$

Cyanide ion is formed in reaction R24 (Scheme 5) after the oxidation of $OSCN^-$ by HSO_5^- ($R21^H$). With increasing $[SCN^-]_0$, the produced amount of CN^- decreases as the relative rate of oxidation of $OSCN^-$ ($R21^H$) decreases. Similar observations were made previously regarding the role of CN^- in the reaction system of SCN^- + HSO_5^- at highly acidic pH.[112,113] The CN^- + $OSCN^-$ reaction (R26) has been already investigated in detail in a wide range of pH by directly mixing the two reactants,[127] and known to be reasonably fast only at pH < 7, which explains the absence of this process in the SO_5^{2-} + SCN^- reaction system at pH 13.5. The inclusion of R26 in the kinetic model of Scheme 5 is not necessary, because the SCN^- + HSO_5^- and the $OSCN^-$ + CN^- reactions are kinetically independent in the applied pH range. The third and slowest process observed at pH 6.89 results in the complete depletion of $OSCN^-$ in minutes. This last and slowest process was identified as the hydrolytic decomposition of $OSCN^-$ to give simple inorganic anions, which will be described later in this thesis.

5.3.3) *pH dependence*

The pH dependence of the $(H)SO_5^-$ + SCN^- reaction has been studied in the pH range from 6.9 to 13.5. The useful pH range is limited because HOSCN rapidly decomposes at 2 < pH < 6 and HOSCN and SCN^- rapidly comproportionate to give $(SCN)_2$ at pH < 2.[115] In order to determine the apparent rate constants for the

oxidation of both SCN^- (k_{20}^{app}) and $OSCN^-$ (k_{21}^{app}) at a given pH, the kinetic experiments were run in duplicates at two different $[SCN^-]_0$ values. The two rate constants can be computed by simultaneously fitting these pairs of experimental kinetic curves to the kinetic model of Scheme 5. The values of both k_{20}^{app} and k_{21}^{app} decrease in a sigmoid fashion with increasing pH as seen in Figure 15. An excellent description of these pH profiles could be given by taking into account the reactivity difference between HSO_5^- and SO_5^{2-}:

$$k_{20}^{app} = k_{20}^{H} \frac{[H^+]}{K_a + [H^+]} + k_{20} \frac{K_a}{K_a + [H^+]} \quad (16)$$

$$k_{21}^{app} = k_{21}^{H} \frac{[H^+]}{K_a + [H^+]} + k_{21} \frac{K_a}{K_a + [H^+]} \quad (17)$$

where K_a is the acid dissociation constant of HSO_5^-, and rate constants k_{20}, k_{20}^{H}, k_{21}, k_{21}^{H} are defined in previous sections. In the final calculations, all kinetic traces recorded at various reactant concentrations and pH values have been fitted simultaneously to the kinetic model of Scheme 5 taking into account the pH dependence of the system. These estimated values for k_{20}, k_{20}^{H}, k_{21}, k_{21}^{H} are listed

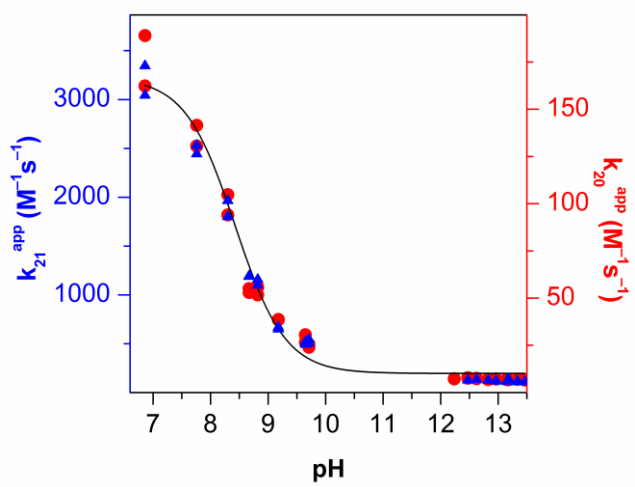

Figure 15. The pH dependence of the SCN^- + $(H)SO_5^-$ reaction system. Dots (right y-scale): apparent rate constants for the oxidation of SCN^- with $(H)SO_5^-$. Triangles (left y-scale): apparent rate constants for the oxidation of $OSCN^-$ with $(H)SO_5^-$. Line: result of a simultaneous fit to eqs. 16 and 17. The y-scales are normalized to each other. $[KHSO_5]_0$ = 5.0 mM, $[NaSCN]_0$ = 50.0 mM or 500 mM, I = 1.0 M, T = 25.0 °C.

in Table 4, and the excellent fit between the experimental results and the calculated data is illustrated in Figure 15. The estimate for $pK_a(HSO_5^-) = 8.43 \pm 0.05$ (I = 1.0 M) is in good agreement with previously published values.[110] The apparent rate constants k_{20}^{app} and k_{21}^{app} decrease linearly with decreasing $[H^+]$ in the pH range from 12.3 to 13.5, where $[H^+] << K_a(HSO_5^-)$ and both eqs. 16 and 17 are simplified to linear correlations. This observation, together with the results of the full-scale pH dependence study, are strong evidence against the presence of any acid/base catalyzed processes in the $(H)SO_5^- + SCN^-$ reaction system.

Table 4. Calculated rate constants and activation parameters in the reaction system $(H)SO_5^- + SCN^-$.

reaction	studied at pH	$k^{298\ K}$ ($M^{-1}\ s^{-1}$)	$\Delta H^{\ddagger}$ (kJ mol^{-1})	$\Delta S^{\ddagger}$ (J K^{-1} mol^{-1})
R20	13.5	$(1.0 \pm 0.2)\times10^1$	35.2 ± 0.5	-108 ± 2
R21	13.5	$(1.6 \pm 0.1)\times10^2$		
$R20^H$	6.9	$(2.0 \pm 0.2)\times10^2$	26 ± 1	-112 ± 3
$R21^H$	6.9	$(3.3 \pm 0.1)\times10^3$	30 ± 2	-77 ± 5

5.3.4) *Temperature dependence*

The temperature dependence of the $HSO_5^- + SCN^-$ reaction has been studied in phosphate buffer at pH 6.54 (measured at 25.0 °C), where the rates of the reactions R20 and R21 are negligible compared to those of $R20^H$ and $R21^H$, respectively. The pH was chosen to be far (at least 1.5 units away) from the pK_a values of both HSO_5^- and HOSCN at 25.0 °C, and phosphate buffer was chosen because its pH shows less than a -0.05 unit / +10 K dependence on temperature.[169] Thus, all complications arising from the possible temperature dependent shifting of the protolytic equilibria in the reaction system were averted by carefully choosing the experimental conditions. In order to obtain information on the temperature dependence of the rate of reactions $R20^H$ (k_{20}^H) and $R21^H$ (k_{21}^H), the same approach was used as in the pH dependence study: two duplicate kinetic experiments were run at two different $[SCN^-]_0$ at a given temperature. The calculated rate constants

k_{20}^{H} and k_{21}^{H} are shown in Figure 16 in the temperature range from 5.0 °C to 45.0 °C. As both R20^{H} and R21^{H} are elementary reactions, the Eyring equation (previously written as eq. 6) can be used to calculate the activation parameters by utilizing a non-linear least squares fitting algorithm:[170]

$$k_{\text{element}} = \frac{k_b T}{h} \exp\left(\frac{\Delta S^{\neq}}{R}\right) \exp\left(-\frac{\Delta H^{\neq}}{RT}\right) \qquad (18)$$

where k_b is the Boltzmann constant, h is the Planck constant, R is the universal gas constant, and $\Delta S^{\ddagger}$ and $\Delta H^{\ddagger}$ are the activation entropy and enthalpy. The resulting activation parameters are listed in Table 4. The temperature dependence of the oxidation of SCN^- with SO_5^{2-} (R20) was also studied at pH 13.5. The excess of SCN^- used in these kinetic experiments ($[SO_5^{2-}]_0$ = 5.0 mM and $[SCN^-]_0$ = 750 mM) was chosen to be high to avoid the oxidation of $OSCN^-$ by SO_5^{2-} (R21). In other words, because the rate of reaction R21 is negligible compared to R20 under the applied experimental conditions, k_{20} could be measured directly. With this approach, we lost the possibility of determining the activation parameters of R21, but excluded the possibility of any systematic error arising from the

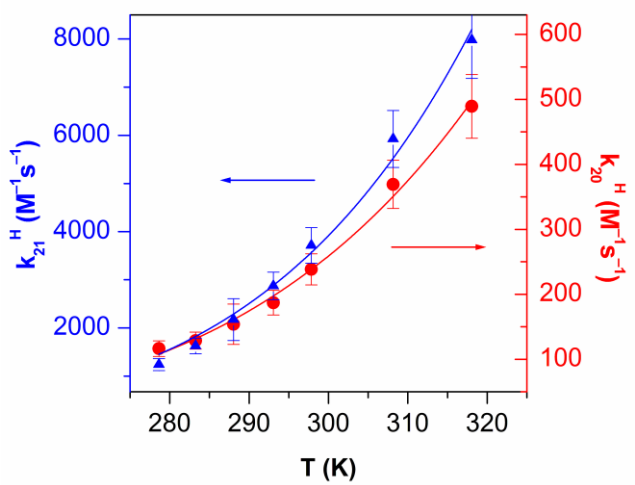

Figure 16. Temperature dependence of the reaction between SCN^- and HSO_5^- at pH 6.54. Red dots (right y-scale): rate constant of the oxidation of SCN^- with HSO_5^- (R20^{H}), blue triangles (left y-scale): rate constant of the oxidation of $OSCN^-$ with HSO_5^- (R21^{H}). Lines: results of nonlinear fits to the Eyring-equation. $[KHSO_5]_0$ = 5.0 mM, $[NaSCN]_0$ = 50.0 mM or 500 mM, I = 1.0 M, pH 6.54 (measured at 25.0 °C).

complicated simultaneous evaluation of two sets of kinetic data. The Eyring equation was used to evaluate the activation parameters from the temperature dependent measurements, and the results are listed in Table 4. The entropies of activation of reactions $R20^H$, R20 and also $R21^H$ are large negative values close to -100 J mol^{-1} K^{-1}. Similar entropies of activation have been measured in the reactions of HSO_5^- with halide ions (Cl^-, Br^-, I^-).[110] The analogy between the oxidation of halides and SCN^- is not surprising, taking into account the well established classification of SCN^- as a pseudo-halide ion. With the methodology presented in ref. 110, one can conclude that the rate determining step in the HSO_5^- + SCN^- ($R20^H$) elementary reaction cannot be a one electron transfer step. At pH 7, the formal potential of the $HSO_5^-/SO_4^{\bullet-}$ couple is (1.19 + 0.0591 × $lg10^{-7}$) V = 0.78 V,[110] whereas the standard reduction potential of the $SCN^{\bullet}/SCN^-$ couple is 1.63 V.[171] Thus the free energy of the possible one electron HSO_5^- + SCN^- ($R20^H$) elementary step would be ((1.63 - 0.78) × 96.485) kJ mol^{-1} = 82 kJ mol^{-1}, which is much higher than the measured free energy of activation at 298 K: (26 + 298 × 0.112) kJ mol^{-1} = 59 kJ mol^{-1}. Therefore, similarly to the reactions of halide ions, the HSO_5^- + SCN^- ($R20^H$) elementary step is more likely to proceed through an initial two electron oxidation, probably involving concerted heterolytic O–O bond cleavage and S–O bond formation. This mechanism is expected to involve much more geometric reorganization, and characterized by higher activation entropy than a one electron transfer rate-determining step, which does not include atom transfer before the transition state. In accordance with the concluding thoughts of ref. 110; a generalization is risky without a sufficiently high number of reliably measured activation parameters in the literature for the reactions of HSO_5^- and SO_5^{2-}. Still the -80 – -110 J $mol^{-1}K^{-1}$ activation entropies of $R20^H$, R20 and $R21^H$ seem to suggest that all of these processes proceed through two electron transfer rate determining steps rather than one electron transfer steps.

5.3.5) *Catalysis by MnTMe-4-PyP^{5+}*

The oxidation of MnTMe-4-PyP^{5+} by HSO_5^- at pH 7.4 has been described in earlier literature.[118] The first step in this process is the formation of the Mn^V(O) porphyrin in a second order reaction (k_{27}^{litr} = 6.9 × 10^5 M^{-1} s^{-1}). However, the Mn^V(O) porphyrin is not stable in water and decomposes in a pseudo-first order

reaction to give the $Mn^{IV}(O)$ porphyrin, which has a significantly longer lifetime under the conditions applied:

$HSO_5^- + Mn^{III}TMe \rightarrow SO_4^{2-} + Mn^{V}(O)TMe + H^+$ $\quad k_{27}$ (R27)

$Mn^{V}(O)TMe \rightarrow\rightarrow Mn^{IV}(O)TMe$ $\quad k_{28}$ (R28)

When the initial concentrations of HSO_5^- and MnTMe-4-PyP^{5+} are comparable, R27 becomes rate limiting, and the formation of the intermediate $Mn^{V}(O)$ porphyrin becomes barely detectable because of its fast decomposition in R28.[118] We carried out stopped-flow experiments to validate these findings at pH 6.81. In the initial concentration range of $[Mn^{III}TMe]_0 = 50$ μM and $[HSO_5^-]_0$ = from 5.0 to 500 μM, the recorded kinetic curves show pseudo-second order behavior ($k_{27}^{meas} = (6.5 \pm 0.1) \times 10^5$ M^{-1} s^{-1}) accompanied by the formation of a relatively stable product with an A_{max} at 425 nm (Figure 17). This band is characteristic of $Mn^{IV}(O)$TMe-4-PyP^{5+}. Furthermore, the stoichiometry was determined to be 1 : 1 regarding the formation of the $Mn^{IV}(O)$ porphyrin in the reaction between MnTMe-4-PyP^{5+} and HSO_5^- (Figure 17), which is also consistent with the presence of the consecutive reactions R27 and R28.

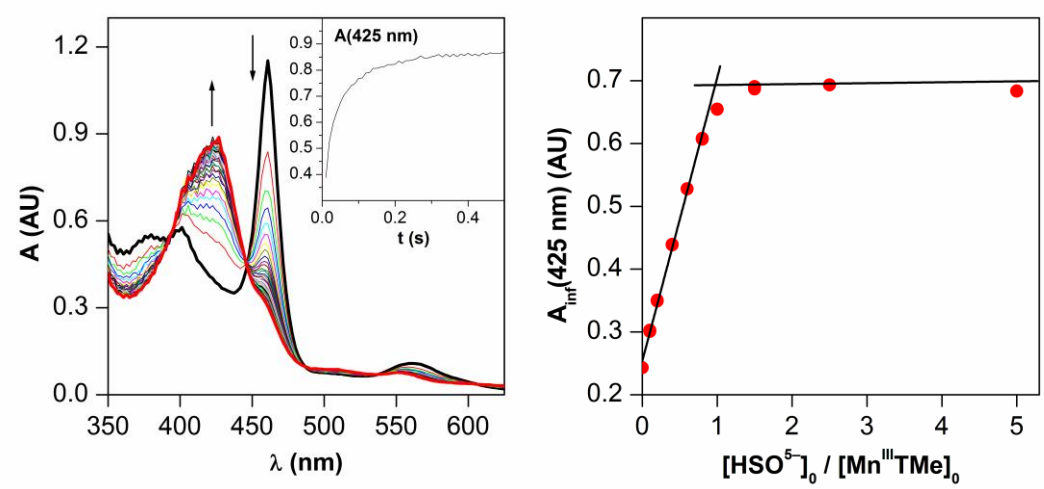

Figure 17. Left panel: UV-vis spectral change recorded in the reaction of HSO_5^- + MnTMe-4-Pyp^{5+} at pH 6.81. Inset: the kinetic curve at 425 nm. Right panel: the stoichiometry of the HSO_5^- + MnTMe-4-Pyp^{5+} reaction was determined to be 0.96 by plotting the final absorbance readings of the kinetic curves versus the reactant ratios. $[KHSO_5]_0$ = from 5.0 μM to 500 μM, $[Mn^{III}TMe]_0$ = 50 μM, I = 0.5 M, pH 6.81, T = 25.0 °C, optical path length: 2.00 mm.

The possible catalytic effect of MnTMe-4-PyP^{5+} in the reaction of HSO_5^- + SCN^- has been studied at pH 6.84 by single-mixing stopped-flow experiments. A buffered solution of HSO_5^- was mixed with a solution containing both MnTMe-4-PyP^{5+} and SCN^-. The concentration range of the kinetic study had to be chosen carefully in order to minimize the rate of the direct HSO_5^- + SCN^- reaction (R20^H) and to be optimal for following the kinetics of the processes. The UV-vis absorbance of the various MnTMe-4-PyP^{5+} species suppress all other signals in the wavelength range from 350 nm to 650 nm, even when [MnTMe-4-PyP^{5+}]$_0$ is present in only 5 % compared to [HSO_5^-]$_0$ and [SCN^-]$_0$. For these reasons, kinetic traces were recorded only in the relatively narrow concentration range of [HSO_5^-]$_0$ = 50 μM, [Mn^{III}TMe]$_0$ = 50 μM and [SCN^-]$_0$ = from 25 to 1000 μM. The reaction was studied on a timescale from 5 ms to 2 s. As demonstrated in Figure 18 (left panel), no spectral change occurs when the initial concentration of HSO_5^- is lower than the initial concentration of SCN^- ([HSO_5^-]$_0$ < [SCN^-]$_0$). When the initial concentration of HSO_5^- is higher than that of SCN^-, the absorbance increases at 425 nm, which is consistent with the formation of Mn^{IV}(O)TMe-4-PyP^{4+}. In those

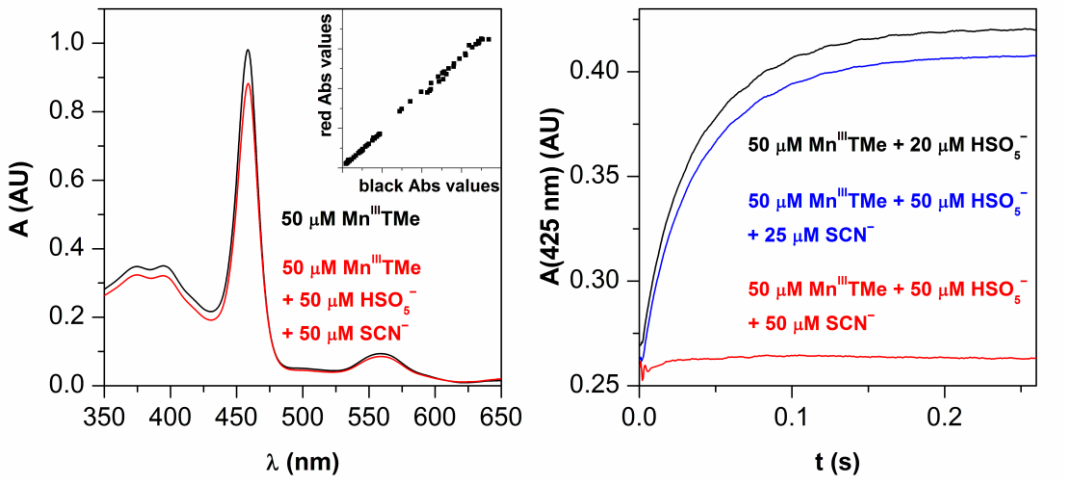

Figure 18. Left panel: the spectrum of MnTMe-4-Pyp^{5+} and the final spectrum of the HSO_5^- + SCN^- + MnTMe-4-Pyp^{5+} reaction mixture recorded 0.10 s after mixing. Inset: the two sets of absorbance values are plotted versus each other in every wavelength, demonstrating that the two spectra are identical. Right panel: the production of the Mn^{IV}(O) porphyrin was followed at 425 nm. In the presence of equimolar SCN^- and HSO_5^- no accumulation of the Mn^{IV}(O) complex took place. I = 1.0 M, pH 6.84, T = 25.0 °C, optical path length: 2.00 mm.

cases when the formation of the Mn^{IV}(O) porphyrin takes place, it follows the same kinetics as observed in some control runs when no SCN^- was present in the solution (Figure 18, right panel). At a particular [MnTMe-4-PyP^{5+}]$_0$, the kinetic curve corresponding to a given [HSO_5^-]$_0$ and [SCN^-]$_0$ approximately overlaps with the kinetic curve recorded at a different [HSO_5^-]$_0$* in the absence of SCN^- where the following is true: [HSO_5^-]$_0$* ≈ ([HSO_5^-]$_0$ – [SCN^-]$_0$). These observations can be summarized as follows. In the HSO_5^- + SCN^- + MnTMe-4-PyP^{5+} reaction mixture, apparently, the Mn(III) porphyrin is not involved in any reactions until SCN^- is present in excess over HSO_5^- ([HSO_5^-]$_0$ < [SCN^-]$_0$). At HSO_5^- excess ([HSO_5^-]$_0$ > [SCN^-]$_0$), the undisturbed accumulation of the Mn^{IV}(O) porphyrin takes place possibly by reactions R27 and R28. These observations can be explained, first by considering that under identical conditions the oxidation of SCN^- by HSO_5^- (k_{20}^{H} = 203 M^{-1} s^{-1}) is much slower than the oxidation of MnTMe-4-PyP^{5+} by HSO_5^- (k_{27}^{meas} = 6.5 × 10^5 M^{-1} s^{-1}). Therefore in the same reaction mixture the consumption of HSO_5^- by SCN^- cannot be faster than the reaction of HSO_5^- with MnTMe-4-PyP^{5+}. It is logical to assume that HSO_5^- oxidizes the Mn(III) porphyrin, but the higher oxidation states thus formed are rapidly reduced back to MnTMe-4-PyP^{5+} by SCN^- and the formation of a catalytic cycle takes place. At [HSO_5^-]$_0$ > [SCN^-]$_0$, this cycle is rapidly terminated by the depletion of SCN^-, and only the subsequent formation of Mn^{IV}(O)TMe-4-PyP^{4+} is apparently followed by stopped-flow spectrometry, similarly to the case when SCN^- is not even initially present is the solution. The facts that no change in the absorbance signal is detectable at [HSO_5^-]$_0$ < [SCN^-]$_0$, and that no induction period is observed in the kinetic curves at [HSO_5^-]$_0$ > [SCN^-]$_0$ further suggest that, when initially present, the depletion of SCN^- is complete in the mixing time of the stopped-flow instrument. The proposed mechanism of the catalytic oxidation of SCN^- is shown in Scheme 6. To collect experimental evidence for deciding whether the Mn^{IV}(O) or the Mn^{V}(O) porphyrin species is capable for the rapid oxidation of SCN^-, the direct oxidation of SCN^- by Mn^{IV}(O)TMe-4-PyP^{4+} (R29) has been studied in detail with double-mixing stopped-flow technique. The Mn^{IV}(O) porphyrin (50 μM) was in situ prepared in the first mixing cycle of the instrument by the reaction of HSO_5^- + MnTMe-4-PyP^{5+} with 1.0 s aging time ($\Delta\tau_1$), and then it was mixed with a large excess of SCN^- (from 50 to 500 mM). The reduction of Mn^{IV}(O)TMe to MnTMe-4-PyP^{5+} took place in a pseudo-first order reaction under the conditions

Scheme 6. Proposed kinetic model for the MnTMe-4-Pyp^{5+} catalyzed oxidation of SCN^- by HSO_5^- at pH 6.8. The rate constants are in the following relationship: $k_{29} < k_{20}^{H} << k_{27} << k_{30}$; therefore reactions R20^H and R29 are not significant regarding the catalytic cycle. Reaction R28 consumes the important intermediate Mn^V(O)TMe-4-Pyp^{5+} and therefore degrades the catalytic efficiency. MnTMe-4-PyP^{5+} is abbreviated as Mn^{III}TMe and the higher oxidation state species accordingly.

$HSO_5^- + Mn^{III}TMe \rightarrow SO_4^{2-} + Mn^{V}(O)TMe + H^+$	$\boldsymbol{k_{27}}$	(R27)
$Mn^{V}(O)TMe \rightarrow\rightarrow Mn^{IV}(O)TMe$	$\boldsymbol{k_{28}}$	(R28)
$HSO_5^- + SCN^- \rightarrow SO_4^{2-} + OSCN^- + H^+$	$\boldsymbol{k_{20}^{H}}$	(R20^H)
$Mn^{IV}(O)TMe + SCN^- \rightarrow\rightarrow Mn^{III}TMe + O_xSCN^-$	$\boldsymbol{k_{29}}$	(R29)
$Mn^{V}(O)TMe + SCN^- \rightarrow\rightarrow Mn^{III}TMe + O_xSCN^-$	$\boldsymbol{k_{30}}$	(R30)

applied, no signs of more complicated kinetics have been observed (Figure 19). The rate constant of this reaction ($k_{29} = 112 \pm 3$ M^{-1} s^{-1}), however, was found to be even lower than that of the direct oxidation of SCN^- by HSO_5^- ($k_{20}^{H} = 203$ M^{-1} s^{-1}), thus too low to account for the formation of a catalytic cycle in the HSO_5^- + SCN^- + MnTMe-4-PyP^{5+} system. Consequently, after excluding every other logical possibilities, we propose that the catalytic effect can be attributed to intermediate Mn^V(O)TMe-4-PyP^{5+}. The relevant reactions in the cycle are assumed to be the direct oxidation of MnTMe-4-PyP^{5+} by HSO_5^- to Mn^V(O)TMe-4-PyP^{5+} (R27) and the rapid subsequent reduction of the Mn^V(O) porphyrin to MnTMe-4-PyP^{5+} by SCN^- (R30). It is theoretically possible to study the SCN^- + Mn^V(O)TMe-4-PyP^{5+} reaction independently in sequential-mixing experiments by first generating Mn^V(O)TMe-4-PyP^{5+} with *m*-chloroperoxybenzoic acid (*m*-CPBA), and then subsequently mixing it with SCN^- within some milliseconds. These experiments, however, have not been completed until the writing of this thesis. Based on previously investigated analogous reactions with halide ions,[116,172] we propose that the rate constant of reaction R30 should be around two magnitudes higher than that of R27: $k_{27}^{meas} = 6.5 \times 10^5$ M^{-1} s^{-1} << $k_{30} \approx 10^7$ M^{-1} s^{-1}. This correlation of the rate constants would also ensure that, according to the kinetic model of Scheme 6, the accumulation of neither the intermediates Mn^V(O) nor Mn^{IV}(O) porphyrins can take place while SCN^- is present in the system, which is in agreement with our experimental observations. Reaction R28 consumes the important intermediate Mn^V(O)TMe-4-PyP^{5+} and therefore degrades the catalytic efficiency.

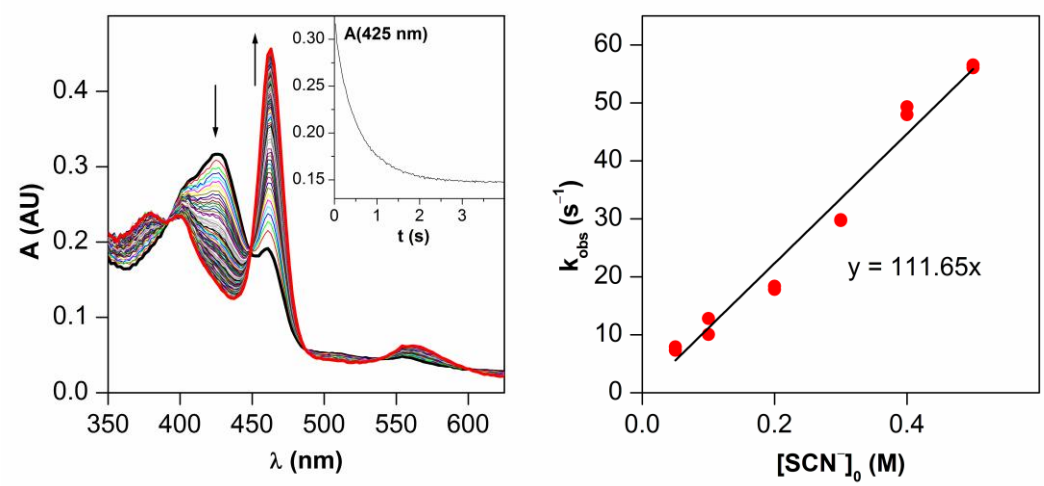

Figure 19. Left panel: UV-vis spectral change recorded in double-mixing experiments in the Mn^{IV}(O)TMe-2-PyP^{4+} + SCN^- reaction system at pH 6.87. Inset: the kinetic curve at 425 nm. Right panel: the observed pseudo-first order rate constant was found to be directly proportional to the initial concentration of SCN^-. $[Mn^{IV}(O)TMe]_0$ = 25 μM, $[NaSCN]_0$ = from 50 mM to 500 mM, I = 1.0 M, pH 6.87, T = 25.0 °C, optical path length: 2.00 mm.

The oxidation product of SCN^- in the catalytic system could not be identified from the multiwavelength UV-vis measurements, as no systematic increase of absorbance was detected at 376 nm (Figure 18 left panel), which could have been attributed to the formation of $OSCN^-$. The half-life of the decomposition of $OSCN^-$ is only a few minutes at pH 6.84 and consequently, the independent analysis of the reaction mixture was found to be challenging by spectroscopic or separation methods. The formation of $OSCN^-$ is probable in the catalytic cycle because the oxidation of SCN^- by Mn^V(O)TMe-4-PyP^{5+} most likely involves oxygen transfer, similarly to the reaction with Br^-.[116] Nevertheless, we assigned a general structure (O_xSCN^-) to the oxidation product of SCN^- in Scheme 6 as $OSCN^-$ has not yet been unambiguously identified.

5.3.6) *Practical implications*

Peroxomonosulfate ion oxidizes SCN^- to $OSCN^-$ in the range of pH from 6.9 to 13.5 (k_{20}^{H} = 2.0 × 10^2 M^{-1} s^{-1} at pH 6.89). The oxidation of $OSCN^-$ by HSO_5^- (k_{21}^{H} = 3.3 × 10^3 M^{-1} s^{-1} at pH 6.89) also takes place in the reaction system of HSO_5^- + SCN^-. Because the rate constant of the oxidation of $OSCN^-$ is an order of magnitude higher than that of SCN^-, these two compounds compete for the oxidant

HSO_5^-, and the quantitative conversion of SCN^- to $OSCN^-$ is possible only by minimizing the relative rate of the "overoxidation" reaction, using at least a 100-fold excess of SCN^- over HSO_5^-. A simple kinetic model has been validated under neutral and basic conditions in the $SCN^- + HSO_5^-$ reaction system, which excludes the equilibrium step between $SCN^- + HSO_5^-$ and $OSCN^- + SO_4^{2-}$ ($R1^H$) presented in the Smith and Wilson model.[113,114] Quantitative information is presented on the kinetics of the oxidation of the antimicrobial $OSCN^-$ by a peroxo compound, which seems to have no precedent in the literature. If the relative reactivities of SCN^- and $OSCN^-$ are expected to be similar towards HSO_5^- and H_2O_2, it is reasonable to assume that the in vivo accumulation of $OSCN^-$ during the defensive peroxidase catalyzed $SCN^- + H_2O_2$ reaction is limited by the presence of H_2O_2 itself. Notably, MnTMe-4-PyP^{5+} was confirmed to catalyze the oxidation of SCN^- by HSO_5^-. The catalytic cycle is assumed to be constructed with the participation of the $Mn^V(O)$ porphyrin as the relevance of the $Mn^{IV}(O)$ porphyrin was excluded.

The high rate of the $HSO_5^- + SCN^-$ reaction might make Oxone® an attractive choice for technologies aiming the oxidative removal of SCN^- from metallurgical wastewater, keeping in mind that method optimization is required to completely avoid the formation of the toxic CN^- as a product.

We assume that during the oxidative thiocyanation of aromatic and aliphatic compounds the in situ formation of the protonated HOSCN (hypothiocyanous acid) takes place in the fast reaction of $HSO_5^- + SCN^-$. In this case, the SCN moiety may act as an S- electrophile reagent because the high electronegativity of oxygen atom significantly lowers the electron density of the soft sulfur atom. By the protonation of HOSCN to H_2OSCN^+, even the formation of ^+SCN is predictable after water elimination. The formation of an electrophile during the in situ oxidation of SCN^- can account for the success of this polarity inversion (*umpolung*) thiocyanation strategy among activated aromatic and α-acidic oxo compounds.

5.4) Hydrolytic decomposition of $(SCN)_2$ and $OSCN^-$

5.4.1) *Decomposition of $OSCN^-$ at pH 4 and at pH 7*

The kinetics of the hydrolytic decomposition of HOSCN has been studied in the pH range from 4.3 to 6.0 by double-mixing stopped-flow technique. The mixture of HOSCN and $OSCN^-$ is present in solution in this pH range because the pK_a of HOSCN is 4.85.[173] As detailed in the experimental section, $OSCN^-$ can be synthesized conveniently only at a high excess of SCN^- present over the oxidizing agent. Thus the resulting $OSCN^-$ solution also contains the remaining SCN^-. The decomposition of HOSCN was monitored photometrically at multiple wavelengths from 290 to 705 nm where two spectral features are observed: a shoulder at 306 nm and the global A_{max} at 376 nm, as seen in Figure 20. At constant SCN^- concentration (see the experimental section) and pH, matrix rank analysis of the collected time-resolved spectra showed that no absorbing intermediates are present at detectable quantities during the decomposition over wide ranges of [SCN^-] and pH. According to the singular value decomposition analysis of time-resolved multi-wavelength data with SpecFit/32 software, the reaction follows strict pseudo-first order kinetics when the precursor SCN^- is in excess over HOSCN. Second order kinetics has never been observed during the experiments.[115,119] The half-life of the hydrolysis of HOSCN is ca. 0.5 s, depending on the actual conditions (Figure 20).

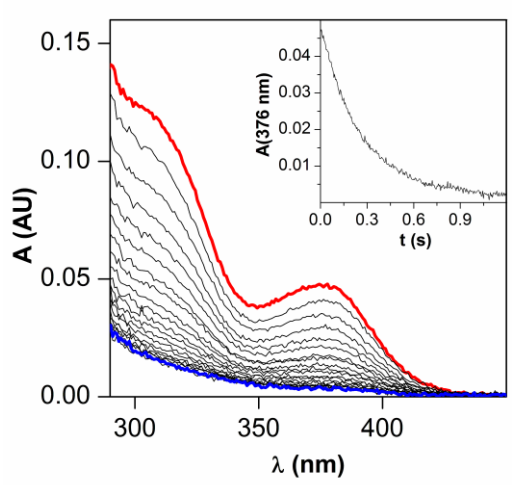

Figure 20. UV-vis spectral change recorded in the decomposition of HOSCN/$OSCN^-$ at pH 4.93 under high SCN^- excess. Inset: kinetic curve at 376 nm. $[HOSCN]_{T,0}$ = 3.5 mM, [SCN^-] = 0.25 M, [HOAc] + [OAc^-] = 0.50 M, pH 4.93, I = 1.0 M, T = 25.0°C.

The measured pseudo-first order rate constant (k_{obs}) was found to be invariable to the buffer concentration and to the initial analytical HOSCN concentration written as $[HOSCN]_{T,0} = [HOSCN]_0 + [OSCN^-]_0$. The observed pseudo-first order rate constant is directly proportional to $[SCN^-]$ over an order of magnitude change in $[SCN^-]$, with a negligible ordinate intercept, as shown in Figure 21.

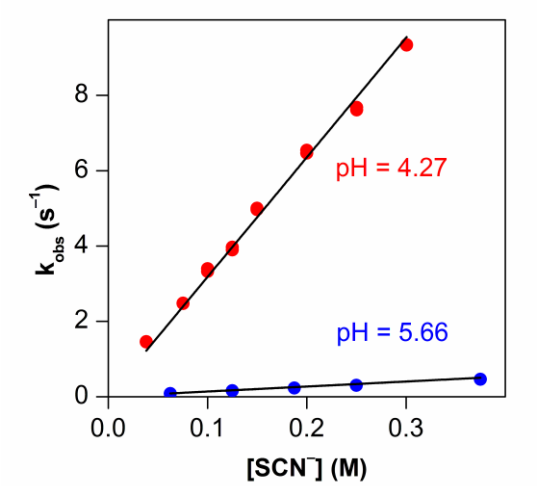

Figure 21. Measured $[SCN^-]$ dependence of the observed pseudo-first order rate constant of the decomposition of HOSCN/$OSCN^-$ at pH 4.27 and pH 5.66. Dots: experimental data, Lines: the result of the global fit. $[HOSCN]_{T,0}$ = 3.5 mM, $[SCN^-]$ = from 0.05 to 0.40 M, I = 1.0 M,T = 25.0 °C.

The $[H^+]$ dependency of the hydrolytic reaction is complex. At constant $[SCN^-]$, the initial spectrum of the reactant solution recorded 0.75 ms after the jump to the desired pH (second mixing) is pH dependent as seen in Figure 22. The series of the initial spectra recorded at different pH values can be successfully analyzed by taking into account only the protolytic equilibrium between HOSCN (with an A_{max} at 306 nm) and $OSCN^-$ (with an A_{max} at 376 nm) (Figure 22). The left panel of Figure 22 shows how k_{obs} increases with $[H^+]$. The k_{obs} versus $[H^+]$ curve is sigmoidal, and it can be fitted to the following function:

$$k_{obs} = \frac{\xi_1'[H^+]^2}{\xi_2 + \xi_3[H^+] + [H^+]^2} \qquad (19)$$

where ξ'_1, ξ_2 and ξ_3 are pH-independent constants and are listed in Table 5. If we take into account that k_{obs} is directly proportional to [SCN^-], the following rate law is deduced to describe the hydrolysis of HOSCN at pH 4:

$$v = -\frac{\mathrm{d}[\mathrm{HOSCN}]_T}{\mathrm{d}t} = \frac{\xi_1[H^+]^2[SCN^-]}{\xi_2 + \xi_3[H^+] + [H^+]^2}[\mathrm{HOSCN}]_T \qquad (20)$$

where ξ_1, ξ_2 and ξ_3 are constants and $[\mathrm{HOSCN}]_T$ is the time-dependent analytical concentration of HOSCN + $OSCN^-$ in the reaction mixture.

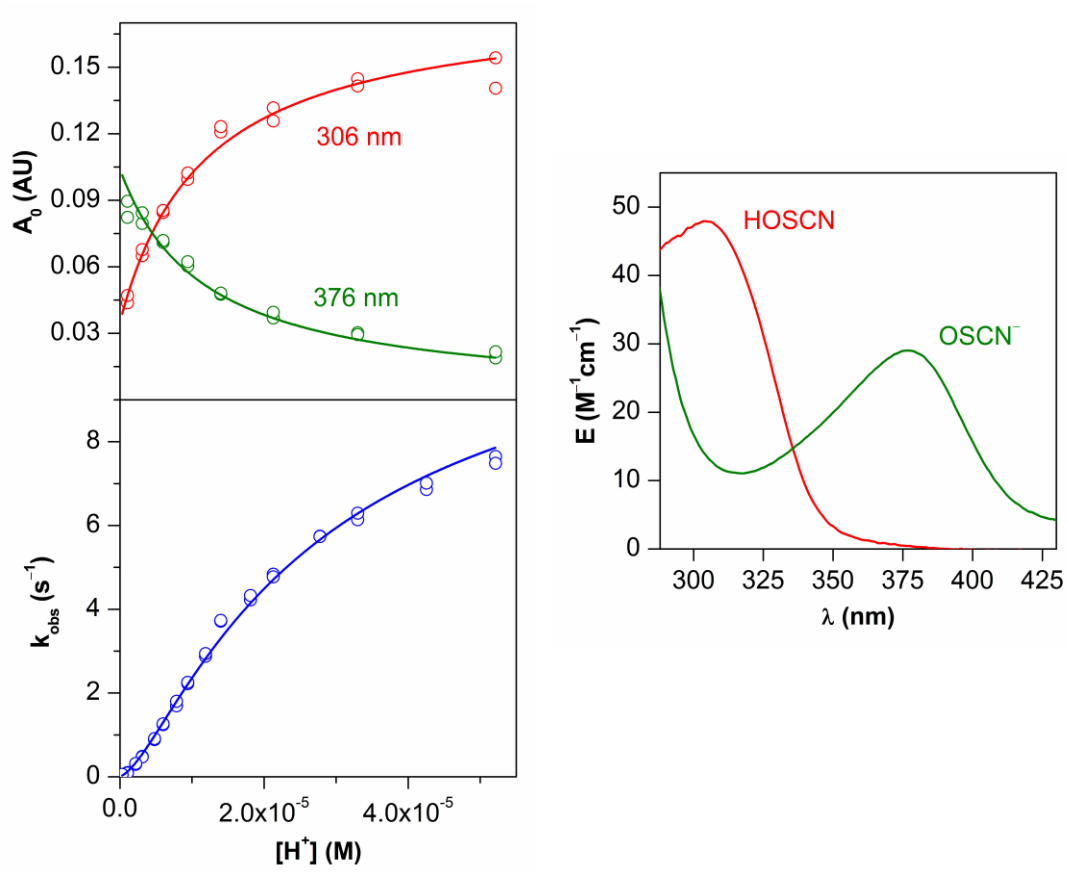

Figure 22. Left panel: pH dependence of the initial absorbance (A_0, top) and the observed pseudo-first order rate constant (k_{obs}, bottom) of the decomposition of HOSCN/$OSCN^-$ in the pH range from 4.37 to 5.66. Markers: measured data (A_0: red – 306 nm, blue – 376 nm). Lines: results of the global data fit. Right panel: calculated spectra of HOSCN (red) and $OSCN^-$ (green). $[\mathrm{HOSCN}]_{T,0}$ = 3.5 mM, [SCN^-] = 0.25 M, [HOAc] + [OAc^-] = 0.50 M, from pH 4.28 to pH 5.98, I = 1.0 M, T = 25.0°C.

Mass spectrometric experiments have provided evidence for the formation of CN^-, OCN^-, SO_4^{2-} and traces of SO_3^{2-} during the hydrolytic decomposition of HOSCN around pH 4. Hypothiocyanite ion was also identified by ESI-MS from the basic stock solution of NaOSCN. The species from *m*/*z* 50 to *m*/*z* 250 present in the MS spectra of the above mentioned analyte solutions are exclusively singly charged ion-clusters. In positive mode, the most common are: $Na_2C_2H_3O_2^+$, $Na_2H_2PO_4^+$, Na_2SCN^+, $Na_2ClO_4^+$, Na_2Cl^+, Na_2CN^+, Na_2OCN^+ and Na_2OH^+. In negative mode ClO_4^- containing species are more abundant in the spectra: $NaClO_4C_2H_3O_2^-$, $Na_2PO_4^-$, $Na(SCN)_2^-$, $Na(ClO_4)_2^-$, $NaClO_4Cl^-$, $NaClO_4CN^-$, $NaClO_4OCN^-$ and $NaClO_4OH^-$ depending on the actual analyte. Larger clusters simultaneously containing multiple different anions and/or cations (when K^+ was also present) were also detected. The species were identified based on their accurate masses ($\Delta m/z = \pm 3 - 7$ ppm, see Table 6). The charge distribution inside a cluster is not unambiguous. However, all of those detected could be constructed from simple ions. Thus, we propose that the decomposing solution of HOSCN contains only small anions and the accompanying alkali cations.

The concentrations of the identified hydrolysis products of HOSCN were measured by IC. The amount of these anions relative to $[HOSCN]_{T,0}$ are given in Table 7. According to control experiments when $OSCN^-$ was synthesized from stoichiometric amounts of SCN^-, the quantity of the hydrolytic products are invariable to the presence of excess SCN^- during the decomposition.

Table 5. Estimated empirical constants for the experimentally determined rate laws.

constant	estimated value	constant	estimated value
ξ'_1	$10.3 \pm 0.3\ s^{-1}$	ξ_{11} (pH 3.9)	$0.34 \pm 0.18\ M^{-1}$
ξ_1	$41 \pm 1\ M^{-1}s^{-1}$	ξ_{10} (pH 4.4)	$882 \pm 29\ s^{-1}$
ξ_2	$(1.5 \pm 0.1) \times 10^{-10}\ M^2$	ξ_{11} (pH 4.4)	$0.31 \pm 0.13\ M^{-1}$
ξ_3	$(1.7 \pm 0.2) \times 10^{-5}\ M$	ξ_{12}	$(5.6 \pm 0.1) \times 10^{12}\ s^{-1}$
ξ_4	$(1.03 \pm 0.03) \times 10^{-1}\ M^{-1}s^{-1}$	ξ_{13}	$(3.1 \pm 0.1) \times 10^{9}\ M^{-1}$
ξ_5	$(6.7 \pm 0.8) \times 10^{-3}\ s^{-1}$	ξ_{14}	$(2.8 \pm 0.2) \times 10^{3}\ AU^{-1}s^{-1}$
ξ_6	$(1.70 \pm 0.02) \times 10^{5}\ M^{-1}s^{-1}$	ξ_{15}	$-(1.9 \pm 0.2) \times 10^{3}\ s^{-1}$
ξ_7	$(4.6 \pm 0.8) \times 10^{-3}\ s^{-1}$	ξ_{16}	$(6.2 \pm 0.3) \times 10^{12}\ M^{-1}s^{-1}$
ξ_8	$(6.8 \pm 0.7) \times 10^{4}\ M^{-2}s^{-1}$	ξ_{17}	$0.54 \pm 0.19\ M^{-1}$
ξ_9	$(4.8 \pm 0.5) \times 10^{-3}\ s^{-1}$	ξ_{18}	$(3.0 \pm 0.2) \times 10^{9}\ M^{-1}$
ξ_{10} (pH 3.9)	$362 \pm 10\ s^{-1}$		

Table 6. List of ion clusters identified by ESI-MS from various analyte solutions.

	+species	m/z		difference (ppm)
		measured	theoretical	
$OSCN^-$	$Na_2(OSCN)^+$	119.9495	119.9491	-3.3
CN^-	$Na_2(CN)^+$	71.9826	71.9821	-6.9
OCN^-	$Na_2(OCN)^+$	87.9776	87.9770	-6.8
SO_3^{2-}	$Na_3(SO_3)^+$	148.9253	148.9256	2.0
SO_4^{2-}	$Na_3(SO_4)^+$	164.9195	164.9205	6.1
S_3	HS_3^+	96.9228	96.9235	7.2
	–species			
$OSCN^-$	$NaClO_4OSCN^-$	195.9077	195.9089	6.1
CN^-	$NaClO_4CN^-$	147.9414	147.9419	3.4
OCN^-	$NaClO_4OCN^-$	163.9363	163.9368	3.0
SO_3^{2-}	$Na(SO_3)^-$	102.9476	102.9471	-4.9
SO_4^{2-}	$Na(SO_4)^-$	118.9419	118.9420	0.8

Table 7. Results of the ion chromatographic analyses of the hydrolysis products of $(SCN)_2$ and HOSCN/$OSCN^-$. The values given are relative to the concentration of the initial reactant ($(SCN)_2$ or $OSCN^-$). Brackets: calculated values based on the proposed stoichiometry of the reactions (Scheme 7 and 8) and on the indicated contribution to the total consumption of the reactants of the HOSCN + CN^- pathway (Scheme 9, R46).

reactant and pH of hydrolysis	**relative concentration (%)**					HOSCN + CN^- pathway
	OCN^-	**CN^-**	**SO_3^{2-}**	**SO_4^{2-}**	**SCN^-**	
$OSCN^-$	11 ± 2	8 ± 2	2 ± 1	20 ± 6	69 ± 6	
pH 4.33	(17)	(11)	(3)	(25)	(71)	14%
$OSCN^-$	53 ± 8	0	5 ± 2	17 ± 4	55 ± 8	
pH 6.82	(27)	(0)	(8)	(19)	(73)	19%
$(SCN)_2$	12 ± 2	23 ± 5	4 ± 1	22 ± 2	159 ± 7	
pH 3.89	(12)	(19)	(4)	(27)	(169)	8%
$(SCN)_2$	59 ± 6	0	7 ± 2	18 ± 1	144 ± 9	
pH 6.90	(28)	(0)	(10)	(18)	(172)	17%

The kinetics of the hydrolytic decomposition of the deprotonated $OSCN^-$ has been studied in the pH range from 6.1 to 7.2. The reaction is strictly pseudo-first order when SCN^- is in a large excess over $OSCN^-$, with a half-life of ca. 20 s. Matrix rank analysis of time-resolved photometric data revealed only one detectable absorbing species (with an A_{max} at 376 nm) during the reaction. The measured values of the observed pseudo-first order rate constant (k_{obs}) are independent of the initial $OSCN^-$ concentration and the buffer concentration, and k_{obs} is proportional to [SCN^-] with a non-zero intercept (Figure 23):

$$k_{obs} = \xi_4[SCN^-] + \xi_5 \qquad (21)$$

where ξ_4 and ξ_5 are [SCN^-]-independent constants (Table 5). The initial spectrum of the reactant solution recorded 0.75 ms after pH-jump is independent of [H^+] in this pH range, although k_{obs} is proportional to [H^+] with a non-zero ordinate intercept (Figure 23):

$$k_{obs} = \xi_6[H^+] + \xi_7 \qquad (22)$$

where ξ_6 and ξ_7 are pH-independent constants (Table 5). As seen in Table 5 a simple calculation leads to: $\xi_4 / [H^+] = \xi_6 / [SCN^-]$ and $\xi_5 = \xi_7$. Thus, the rate law for the decomposition of $OSCN^-$ at pH 7 is:

$$v = -\frac{d[HOSCN]_T}{dt} = \left(\xi_8[H^+][SCN^-] + \xi_9\right)[HOSCN]_T \qquad (23)$$

where ξ_8 and ξ_9 are constants, $\xi_8 = \xi_4 / [H^+] = \xi_6 / [SCN^-]$, and $\xi_9 = \xi_5 = \xi_7$. Consequently, $[HOSCN]_T$ is the time-dependent analytical concentration of $HOSCN + OSCN^-$ in the reaction mixture.

The ions OCN^-, SO_4^{2-} and SO_3^{2-} were identified in the ESI-MS spectrum of the sample solution produced during the decomposition of $OSCN^-$ around pH 7. Evidence was also found for the presence of traces of elementary sulfur in the product solution, as HS_3^+ (m/z = 96.9228) was identified in the +ESI-MS spectrum of that.

According to IC measurements, the proportions of the product ions are significantly different from that observed in acetate buffer, as seen in Table 7. The measured product distribution around pH 7 has been found to be independent of whether $OSCN^-$ is generated from $(SCN)_2$ or by the LPO/SCN^-/H_2O_2-system. Accordingly, no effect of excess SCN^- is observed on the product distribution.

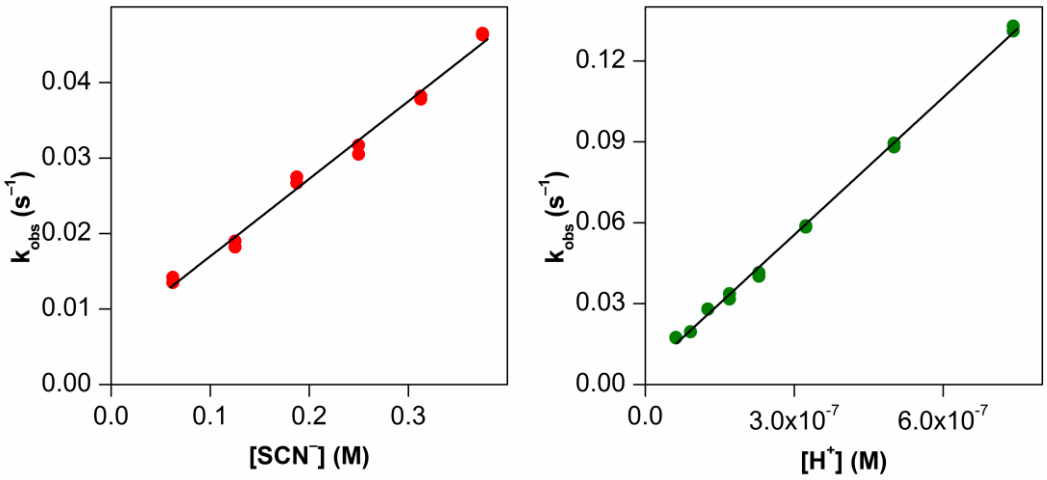

Figure 23. The obtained $[SCN^-]$ dependence (at pH 6.78) and pH dependence (at $[SCN^-]$ = 0.25 M) of the observed pseudo-first order rate constant of hydrolysis of $OSCN^-$. Dots: measured data, lines: individual fits. $[HOSCN]_{T,0}$ = 2.4 mM, $[SCN^-]$ = from 0.05 to 0.40 M, from pH 6.13 to pH 7.21, I = 1.0 M,T = 25.0°C.

5.4.2) *Decomposition of $(SCN)_2$ at pH 4 and at pH 7*

Double-mixing stopped-flow experiments were performed to study the hydrolytic decomposition of $(SCN)_2$ from pH 3.8 to 4.7. Under the applied conditions $(SCN)_2$ and its precursor, SCN^-, give $(SCN)_3^-$ in equilibrium.[115] This equilibrium is established in the mixing time over the entire range of pH. The majority of the kinetic experiments were followed at 300 nm, which is the A_{max} of $(SCN)_3^-$.[115,119,133] Based on the UV-vis and MS spectra (vide infra) of the resulting solution, the hydrolysis product of $(SCN)_2$ is not $OSCN^-$ at pH 4. The hydrolysis of $(SCN)_2$ follows first-order kinetics in the presence of a large excess of SCN^- with a half-life of 2 – 4 ms, depending on the actual conditions (Figure 24). The kinetic curves recorded at high $[(SCN)_2]_{T,0}$ cannot be fitted to second order kinetic functions, and the least-squares residuals are the same for single exponential and biexponential fits. As expected, the observed pseudo-first order rate constant (k_{obs}) was found to be generally independent of $[(SCN)_2]_{T,0}$. However, for $[(SCN)_2]_{T,0}$ lower than ca. 200 – 300 μM, k_{obs} decreases with decreasing $[(SCN)_2]_{T,0}$ (Figure 25). The obtained photometric data are exceptionally low quality under these conditions because the measured absolute change is only about 0.03 AU, which is comparable to the level of noise in the first few milliseconds of the measurements as a consequence of the shock of the stopped-flow apparatus.

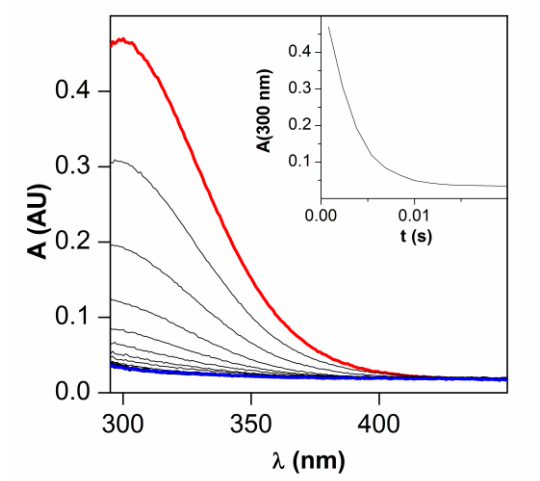

Figure 24. UV-vis spectral change recorded during the hydrolytic decomposition of $(SCN)_2$ at pH 3.88 under high SCN^- excess. Inset: kinetic curve at 300 nm. $[(SCN)_2]_{T,0}$ = 1.0 mM, $[SCN^-]$ = 0.25 M, pH 3.88, I = 1.0 M, T = 25.0 °C.

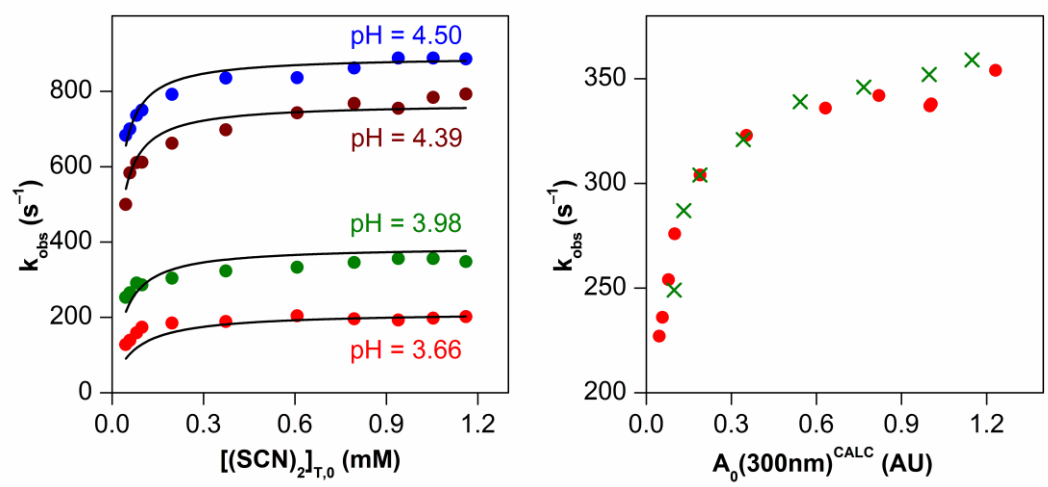

Figure 25. Effect of $[(SCN)_2]_{T,0}$ (the total initial concentration of $(SCN)_2$ + $(SCN)_3^-$ + $HO(SCN)_2^-$) on the observed pseudo-first order rate constants of hydrolysis of $(SCN)_2$. Left panel: experiments in the pH range from 3.66 to 4.50 (indicated in the plot). The kinetics of the reaction deviates from pseudo-first order at low $[(SCN)_2]_{T,0}$. Markers: measured data. Lines: result of global data fit. $[SCN^-]$ = 0.25 M, I = 1.0 M, T = 25.0 °C. Right panel: note, that the calculated initial absorbance (A_0^{CALC}) is directly proportional to $[(SCN)_2]_{T,0}$ at constant pH and $[SCN^-]$. Dots: $[HOCl]_0$ was varied to get different concentrations of $(SCN)_2$. Crosses: $(SCN)_2$ was aged for different extents before the second mixing ($\Delta\tau_1$ variation). $[(SCN)_2]_{T,0}$ = from 0.1 mM to 0.1 mM, $[SCN^-]$ = 0.25 M, pH 3.90, I = 1.0 M, T = 25.0°C.

Nonetheless, least-squares fits of these kinetic curves still give better results with first order than with second order kinetic functions. The applied $[(SCN)_2]_{T,0}$ was established by two different means: (1) by changing the concentration of HOCl in the first mixing cycle and (2) at constant $[HOCl]_0$ by changing the aging-time before the second mixing cycle ($\Delta\tau_1$), thus allowing the in situ generated $(SCN)_2$ to decompose at pH 0.7 to various extents. The independent sets of experiments gave identical results (Figure 25 right panel). The kinetic curves recorded at low $[(SCN)_2]_{T,0}$ match the end of the kinetic curves recorded at high $[(SCN)_2]_{T,0}$ under the same conditions. However, when starting at high $[(SCN)_2]_{T,0}$ the theoretical error of treating the whole course of decomposition as one pseudo-first order process and calculating k_{obs} accordingly is negligible, as only the last 5 – 10% of the data deviates significantly from the single exponential function which fits the majority of the curve. The following results were obtained at high $[(SCN)_2]_{T,0}$

unless stated otherwise. Matrix rank analysis of time-resolved multi-wavelength photometric data revealed that, at constant [SCN^-] and [H^+], only one absorbing species (A_{max} at 300 nm) is present in the hydrolysis reaction in the wavelength range from 290 nm to 705 nm. This also means that the distinctive spectral features of HOSCN are not detectable during the hydrolysis of $(SCN)_2$ at pH 4. The pseudo-first order kinetic curves measured at 300 nm can be extrapolated to the zero-point in the absolute time scale of the reaction using single exponential functions and taking into account the dead time of the instrument. This calculated zero-time absorbance at 300 nm (A_0^{CALC}) increases sigmoidally with [SCN^-] at constant [H^+] (Figure 26 left panel). Two effects are evident in the A_0^{CALC} vs. [SCN^-] curve: (1) shifting of the $(SCN)_2/(SCN)_3^-$ rapid equilibrium, and (2) the rate of decomposition of the in situ generated $(SCN)_2$ shows an inverse second order dependence on [SCN^-] [115,119] at pH 0.7 in the first mixing cycle, thus at lower [SCN^-], we get less $[(SCN)_2]_{T,0}$ after the $\Delta\tau_1$ first aging-time, quantitatively expressed as follows:

$$[(SCN)_2]_{T,0} = \frac{1}{2}\left(\frac{[(SCN)_2]_{T,0}^{fm}}{1 + k_{disp}\left([SCN^-]^{fm}\right)^{-2}[(SCN)_2]_{T,0}^{fm}\Delta\tau_1} \right) \qquad (24)$$

where $[SCN^-]^{fm}$ and $[(SCN)_2]^{fm}_{T,0}$ are the analytical concentrations of SCN^- and $(SCN)_2$ in the first mixing cycle, $\Delta\tau_1$ is the ageing time after the first mixing (usually 2.0 s), k_{disp} is the pseudo-second order rate constant of the decomposition of $(SCN)_2$ at pH 0.7 and $[(SCN)_2]_{T,0}$ is the initial analytical concentration of $(SCN)_2$ in the reaction mixture after the second mixing. The multiplier ½ represents the dilution factor in the second mixing cycle. From separate [SCN^-] dependent stability experiments $k_{disp} = 11 \pm 3\ M^{-1}s^{-1}$ has been estimated at pH 0.70. At pH 4, data recorded at high and low $[(SCN)_2]_{T,0}$ show consistency, i.e., k_{obs} is inversely dependent on [SCN^-] (Figure 26 right panel):

$$k_{obs} = \frac{\xi_{10}}{1 + \xi_{11}[SCN^-]} \qquad (25)$$

where both ξ_{10} and ξ_{11} are [SCN^-]-independent constants. The constant ξ_{10} increases with increasing pH and ξ_{11} slightly decreases with increasing pH (Table 5). At constant [SCN^-], independently from $[(SCN)_2]_{T,0}$, A_0^{CALC} increases to saturation with increasing pH. The initial spectrum (t = 1.5 ms) of the $(SCN)_2$ containing reaction mixture recorded at different pH values displays only one

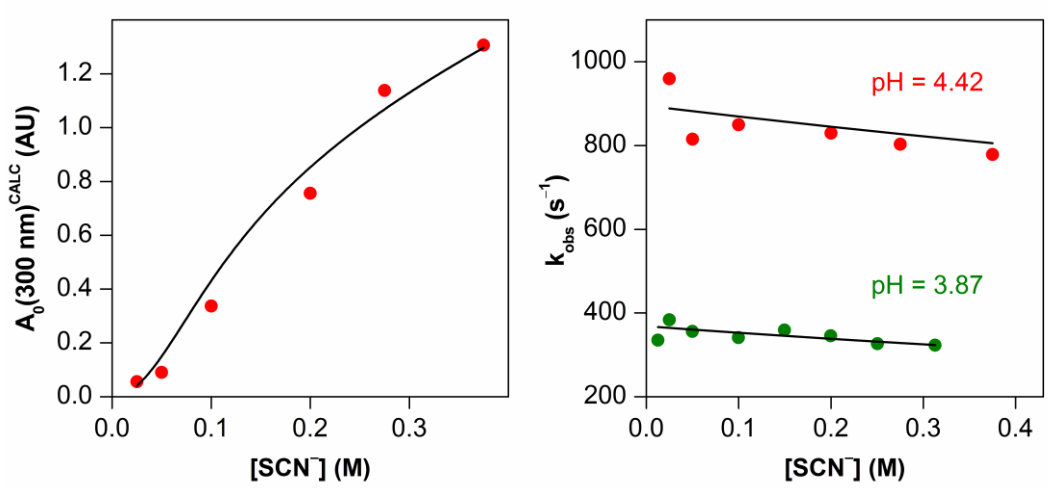

Figure 26. Left panel: dependence of the calculated initial absorbance at 300 nm (A_0^{CALC}) on [SCN^-] recorded at pH 4.42. Right panel: observed [SCN^-] dependence of the pseudo-first order rate constant of hydrolysis of $(SCN)_2$ at pH 4.42 and 3.87. Dots: experimental points. Lines: result of global data fit. $[(SCN)_2]_{T,0}$ = 1.0 mM, [SCN^-] = from 0.01 M to 0.40 M, I = 1.0 M,T = 25.0°C.

peak at 300 nm, thus the fast hydrolytic equilibrium which yields $OSCN^-$ + SCN^- cannot be relevant under the conditions employed.[115,119] As illustrated in Figure 27, k_{obs} approaches saturation with increasing pH, and A_0^{CALC} and k_{obs} are proportional to one another. These curves can be fitted to the following functions both at high and low $[(SCN)_2]_{T,0}$:

$$k_{obs} = \frac{\xi_{12}[OH^-]}{1+\xi_{13}[OH^-]} \tag{26}$$

$$k_{obs} = \xi_{14} A_0^{CALC} + \xi_{15} \tag{27}$$

where ξ_{12}, ξ_{13}, ξ_{14} and ξ_{15} are pH-independent constants (Table 5), although dependent on $[(SCN)_2]_{T,0}$. Thus, from eqs. 25 and 26, the rate law describing the hydrolysis of $(SCN)_2$ at pH 4 at high $[(SCN)_2]_{T,0}$ is the following:

$$v = -\frac{d[(SCN)_2]_T}{dt} = \frac{\xi_{16}[OH^-]}{1+\xi_{17}[SCN^-]+\xi_{18}[OH^-]}[(SCN)_2]_T \tag{28}$$

where ξ_{16}, ξ_{17}, ξ_{18} are constants (Table 5) and $[(SCN)_2]_T$ is the time-dependent analytical concentration of $(SCN)_2$ + $(SCN)_3^-$.

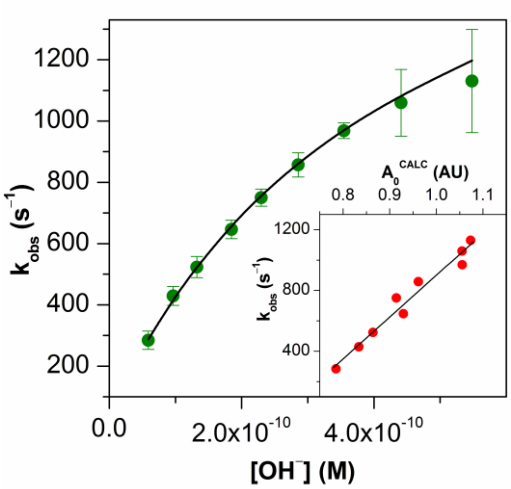

Figure 27. Observed pH dependence of the pseudo-first order rate constant of hydrolysis (k_{obs}) and initial absorbance of $(SCN)_2$ studied in the pH range from 3.77 to 4.74. Inset: k_{obs} is shown to be proportional to the calculated initial absorbance (A_0^{CALC}) of the same experiment at 300 nm. $[(SCN)_2]_{T,0}$ = 1.0 mM, $[SCN^-]$ = 0.25 M, I = 1.0 M,T = 25.0°C.

Mass spectrometric data provided evidence that CN^-, OCN^-, SO_4^{2-} and SO_3^{2-} are produced during the decomposition of $(SCN)_2$ at pH 4. The measured stoichiometry of hydrolysis, relative to $[(SCN)_2]_{T,0}$, is displayed in Table 7. An excess of SCN^- present in the solution during the hydrolytic decomposition has no observable effect on the relative amounts of products.

No kinetic information could be obtained on the decomposition of $(SCN)_2$ around pH 7, as the reaction is complete in the mixing time of the stopped-flow instrument. However, based on UV-vis and MS measurements, $OSCN^-$ is excluded from the products of hydrolysis of $(SCN)_2$ at pH 7. The eventual products at pH 7 (OCN^-, SCN^-, SO_3^{2-} and SO_4^{2-}) were identified by MS and quantified by IC and the stoichiometric results are given in Table 7.

5.4.3) *Reaction of $OSCN^-$ with $(SCN)_2$*

The reaction of HOSCN/$OSCN^-$ and $(SCN)_2$ has been studied in double-mixing stopped-flow experiments at pH 1 and at pH 4. Hypothiocyanite solutions were prepared independently for these experiments and mixed with $(SCN)_2$ solutions made in situ in the first mixing cycle of the stopped-flow instrument. Figure 28 illustrates representative results for the reaction of $(SCN)_2$ with $OSCN^-$. When the

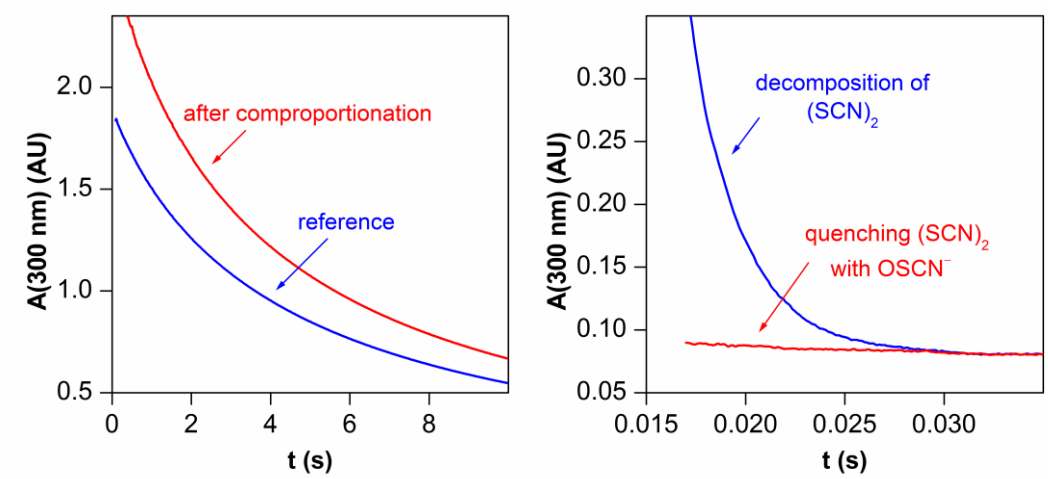

Figure 28. Observed absorbance change at 300 nm after directly mixing solutions of $(SCN)_2$ and $OSCN^-$ at pH 0.70 (left panel) and at pH 3.89 (right panel). At pH 0.70, HOSCN comproportionates with SCN^- to give $(SCN)_2$ which decomposes in a homogeneous second order reaction. $[(SCN)_2]_{T,0}$ = 1.4 mM, $[HOSCN]_{T,0}$ = 1.1 mM, $[SCN^-]$ = 0.25 M, $[HClO_4]$ = 0.20 M, I = 1.0 M, T = 25.0 °C. Blue line: reference ($[HOSCN]_{T,0}$ = 0). Red line: experiment. At pH 3.89, HOSCN quenches $(SCN)_2$. $[(SCN)_2]_{T,0}$ = 1.4 mM, $[HOSCN]_{T,0}$ = 1.2 mM, $[SCN^-]$ = 0.25 M, I = 1.0 M, T = 25.0 °C Blue line: reference ($[HOSCN]_{T,0}$ = 0). Red line: experiment.

two reactants are mixed at pH 0.70 and at high $[SCN^-]$ with $(SCN)_2$ in small excess over HOSCN, an elevation of the absorbance is observed at 300 nm which corresponds to the production of $(SCN)_2$ / $(SCN)_3^-$ in the comproportionation of HOSCN and SCN^-.[115] The production of $(SCN)_2$ is complete within 100 ms, and as seen in Figure 28 it decomposes with homogeneous second-order kinetics.[115,119] When $(SCN)_2$ is mixed with HOSCN at pH 3.89 and at high $[SCN^-]$, the absorbance decreases at 300 nm, 306 nm and 376 nm wavelengths (compared to those of the reference) and the reaction is over within the mixing time. This observation implies the depletion of both HOSCN/$OSCN^-$ and $(SCN)_2$ when they are simultaneously present in solution at pH 4. Although, we have not been able to describe the kinetics of the process in detail to verify the direct reaction of $(SCN)_2$ with HOSCN at pH 4, as maintaining the reaction conditions for a series of experiments proved to be technically challenging. However, a semi-quantitative observation was made that when $[(SCN)_2]_{T,0}$ is varied from 0.1 to 0.3 mM with $[HOSCN]_{T,0}$ = 0.5 mM, the kinetics shows biphasic characteristics (a first step of

1 – 2 ms half-life and a second step with a 0.4 – 0.5 s half-life) with a decrease in absorbance at 300 nm where both $(SCN)_2$ and HOSCN absorb (Figure 29). The chromatographic analysis of the product solution was not successful as all of the experiments were carried out in the presence of high concentrations of SCN^-.

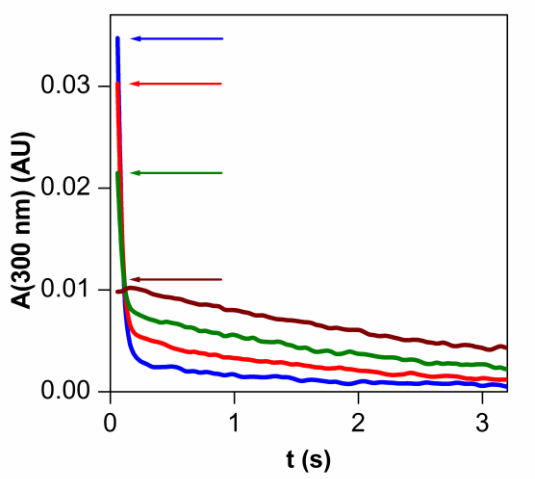

Figure 29. Experimental kinetic curves recorded when $(SCN)_2$ was mixed to excess HOSCN at pH 4.79. At the instance of addition of HOSCN the absorbance signal of $(SCN)_2$ at 300 nm dropped. Brown line: reference $[(SCN)_2]_{T,0} = 0$. Green line: $[(SCN)_2]_{T,0} = 0.1$ mM. Red line: $[(SCN)_2]_{T,0} = 0.2$ mM. Blue line: $[(SCN)_2]_{T,0} = 0.3$ mM. $[HOSCN]_{T,0} = 0.49$ mM, $[SCN^-] = 0.10$ M, I = 1.0 M, T = 25.0°C.

5.4.4) *Mechanism of hydrolysis of $(SCN)_2$ and $OSCN^-$ between pH 4 and 7*

The mechanism proposed to describe the hydrolytic decomposition of HOSCN in the pH range from 4 to 7 is illustrated in Scheme 7. This hydrolysis mechanism is in close intercorrelation with that of $(SCN)_2$ illustrated in Scheme 8. As no second order kinetic behavior was observed during the hydrolysis of HOSCN, the reaction of two HOSCN/$OSCN^-$ molecules[115,119] cannot be a major hydrolysis pathway under the conditions described in the thesis. As seen in Scheme 7, the reactive species is assumed to be the protonated HOSCN both at higher and lower pH. As the first step, we propose the formation of a previously unknown intermediate, $HO(SCN)_2^-$, from HOSCN and SCN^- in equilibrium. Thiocyanate ion is regarded as a pseudo-halide ion and $(SCN)_2$ as a pseudo-halogen based on their chemical reactivity.[82,93,115,119,133,174] The role of I_2OH^- in the hydrolysis chemistry

Scheme 7. Mechanism of decomposition of $OSCN^-$ in the pH range from 4 to 7. The proposed stoichiometry is with $X \leq 1$. The following k_{-32}, k_{-33}, and k_{-34} are the rate constants of the backward reactions of R32, R33 and R34, respectively; italicized reactions occur after the rate-determining R36 step.

$HOSCN \rightleftharpoons OSCN^- + H^+$ — $\boldsymbol{K_{31}}$ fast equilibrium (R31)

$HOSCN + SCN^- \rightleftharpoons HO(SCN)_2^-$ — $\boldsymbol{k_{32}}$ & $\boldsymbol{k_{-32}}$ ($\boldsymbol{K_{32}} = \boldsymbol{k_{32}}/\boldsymbol{k_{-32}}$) (R32)

$HO(SCN)_2^- \rightleftharpoons (SCN)_2 + OH^-$ — $\boldsymbol{k_{33}}$ & $\boldsymbol{k_{-33}}$ ($\boldsymbol{K_{33}} = \boldsymbol{k_{33}}/\boldsymbol{k_{-33}}$) (R33)

$HO(SCN)_2^- + H^+ \rightleftharpoons (SCN)_2 + H_2O$ — $\boldsymbol{k_{34}}$ & $\boldsymbol{k_{-34}}$ ($\boldsymbol{K_3} = \boldsymbol{k_{34}}/\boldsymbol{k_{-34}}$) (R34)

$(SCN)_2 + SCN^- \rightleftharpoons (SCN)_3^-$ — $\boldsymbol{K_{35}}$ fast equilibrium (R35)

$OSCN^- + (SCN)_2 \rightarrow \mathit{NCS(=O)SCN} + \mathit{SCN^-}$ — $\boldsymbol{k_{36}}$, rate determining step (R36)

$\mathit{NCS(=O)SCN} + \mathit{H_2O} \rightarrow \mathit{O_2SCN^-} + \mathit{SCN^-} + \mathit{2H^+}$ *(R37)*

$\mathit{O_2SCN^-} + \mathit{HOSCN} \rightarrow \mathit{O_3SCN^-} + \mathit{SCN^-} + \mathit{H^+}$ *(R38)*

$\mathit{O_3SCN^-} + \mathit{H_2O} \rightarrow \mathit{SO_4^{2-}} + \mathit{HCN} + \mathit{H^+}$ *(R39)*

$\mathit{O_3SCN^-} + \mathit{H_2O} \rightarrow \mathit{SO_3^{2-}} + \mathit{OCN^-} + \mathit{2H^+}$ *(R40)*

$3HOSCN + H_2O \rightarrow XSO_4^{2-} + XHCN + (1\text{-}X)SO_3^{2-} + (1\text{-}X)OCN^- + 2SCN^- + (5\text{-}X)H^+$ (R41)

Scheme 8. Mechanism of decomposition of $(SCN)_2$ at pH 4. The proposed stoichiometry is with $X \leq 1$. To be consistent with the definitions in Scheme 7, k_{-32}, k_{-33} and k_{-34} are the forward rate constants and k_{33}, k_{34} and k_{32} are the backward rate constants of reactions -R32, -R33 and -R34, respectively.

$(SCN)_2 + SCN^- \rightleftharpoons (SCN)_3^-$ — $\boldsymbol{K_{35}}$ fast equilibrium (R35)

$(SCN)_2 + OH^- \rightleftharpoons HO(SCN)_2^-$ — $\boldsymbol{K_{-33}} = \boldsymbol{k_{-33}}/\boldsymbol{k_{33}}$ fast equilibrium (-R33)

$(SCN)_2 + H_2O \rightleftharpoons HO(SCN)_2^- + H^+$ — $\boldsymbol{K_{-34}} = \boldsymbol{k_{-34}}/\boldsymbol{k_{34}}$ fast equilibrium (-R34)

$HO(SCN)_2^- \rightleftharpoons HOSCN + SCN^-$ — $\boldsymbol{k_{-32}}$ & $\boldsymbol{k_{32}}$ ($\boldsymbol{K_{-32}} = \boldsymbol{k_{-32}}/\boldsymbol{k_{32}}$) (-R32)

$HOSCN \rightleftharpoons OSCN^- + H^+$ — $\boldsymbol{K_{31}}$ fast equilibrium (R31)

$(SCN)_2 + OSCN^- \rightarrow \mathit{NCS(=O)SCN} + \mathit{SCN^-}$ — $\boldsymbol{k_{36}}$, rate determining step (R36)

$\mathit{NCS(=O)SCN} + \mathit{H_2O} \rightarrow \mathit{O_2SCN^-} + \mathit{SCN^-} + \mathit{2H^+}$ *(R37)*

$\mathit{O_2SCN^-} + \mathit{HOSCN} \rightarrow \mathit{O_3SCN^-} + \mathit{SCN^-} + \mathit{H^+}$ *(R38)*

$\mathit{O_3SCN^-} + \mathit{H_2O} \rightarrow \mathit{SO_4^{2-}} + \mathit{HCN} + \mathit{H^+}$ *(R39)*

$\mathit{O_3SCN^-} + \mathit{H_2O} \rightarrow \mathit{SO_3^{2-}} + \mathit{OCN^-} + \mathit{2H^+}$ *(R40)*

$3(SCN)_2 + 4H_2O \rightarrow XSO_4^{2-} + XHCN + (1\text{-}X)SO_3^{2-} + (1\text{-}X)OCN^- + 5SCN^- + (8\text{-}X)H^+$ (R42)

of I_2 has been previously described in the literature in detail.[175,176,177] Accordingly, we propose the existence of equilibria R32 – R34 (Schemes 7 and 8). The next step in the hydrolysis of HOSCN is the dissociation of $HO(SCN)_2^-$ to $(SCN)_2$ (R33), which is assumed to be proton catalyzed at lower pH (R34). The hydrolysis of $(SCN)_2$ to give $OSCN^-$ is well defined both at high and at low pH, but not at pH 4 to 7 as $(SCN)_2$ does not hydrolyze to $OSCN^-$ from pH 4 to 7 as demonstrated before. Instead, $(SCN)_2$ is proposed to be an intermediate in the hydrolysis of HOSCN in the pH range from 4 to 7. We propose that the reaction of $(SCN)_2$ with the deprotonated reactant $OSCN^-$ is the key step in the decomposition mechanism. Indirect evidence was found for the existence of the reaction of $(SCN)_2$ + $OSCN^-$ (R36) at pH 4 during the study of the decomposition of $(SCN)_2$ at low $[(SCN)_2]_{T,0}$, i.e., we observed limiting second order behavior. Direct evidence was obtained by mixing the two reactants in independent experiments and confirming their disappearance. Thus, the general rate law describing the hydrolysis of HOSCN/$OSCN^-$ under the applied conditions is deduced from the kinetic model of Scheme 7 by assigning R36 to be the rate limiting reaction step:

$$v = -\frac{\mathrm{d}[\mathrm{HOSCN}]_\mathrm{T}}{\mathrm{d}t} = k_{36}[(\mathrm{SCN})_2][\mathrm{OSCN}^-] \qquad (29)$$
$$[\mathrm{HOSCN}]_\mathrm{T} = [\mathrm{HOSCN}] + [\mathrm{OSCN}^-]$$

Furthermore we assume that some equilibria, marked in Scheme 7, are fast:

$$[\mathrm{HOSCN}] = \frac{[\mathrm{H}^+][\mathrm{HOSCN}]_\mathrm{T}}{K_{31} + [\mathrm{H}^+]} \quad \text{and} \quad [\mathrm{OSCN}^-] = \frac{K_{31}[\mathrm{HOSCN}]_\mathrm{T}}{K_{31} + [\mathrm{H}^+]} \qquad (30)$$

Furthermore, we propose the steady state approximation to be valid for the time-dependent concentrations of the intermediates ($[HO(SCN)_2^-]$ and $[(SCN)_2]$). Both $HO(SCN)_2^-$ and $(SCN)_2$ are proposed to be produced slowly and consumed rapidly. As demonstrated before, their concentrations never exceed low μM that would result in a detectable signal as both $(SCN)_3^-$ (R36) and $HO(SCN)_2^-$ have orders of magnitude higher molar absorbances than HOSCN/$OSCN^-$. Applying these approximations to the simultaneous differential equation system defined by Scheme 7 and substituting to eq. 29 gives:

$$v = \frac{\alpha(1-\alpha)k_{32}k_{36}\left(k_{33}+k_{34}[H^+]\right)[SCN^-][HOSCN]_T^{\,2}}{k_{-32}\left(k_{-33}[OH^-]+k_{-34}\right)+(1-\alpha)k_{36}\left(k_{-32}+k_{33}+k_{34}[H^+]\right)[HOSCN]_T} \qquad (31)$$

$$\alpha = \frac{[H^+]}{K_{31}+[H^+]}$$

At the same time, the following equation is valid:

$$k_{-32}(K_{31}+[H^+])(k_{-33}[OH^-]+k_{-34}) << K_{31}k_{36}(k_{-32}+k_{33}+k_{34}[H^+])[HOSCN]_T \qquad (32)$$

Eq. 31 and 32 lead to the following rate law:

$$v = \frac{k_{32}(k_{33}+k_{34}[H^+])[H^+][SCN^-]}{(k_{-32}+k_{33}+k_{34}[H^+])(K_{31}+[H^+])}[HOSCN]_T \qquad (33)$$

At pH 7, $k_{34}[H^+] << k_{33}$ and $[H^+] << K_{31}$ are valid, therefore eq. 33 can be simplified:

$$v = \frac{k_{32}k_{33}[H^+][SCN^-]}{K_{31}\left(k_{-32}+k_{33}\right)}[HOSCN]_T \qquad (34)$$

The experimentally determined and the deduced limiting rate laws agree both at pH 4 (eq. 20 and eq. 33) and at pH 7 (eq. 23 and eq. 34). However, the proposed mechanism of hydrolysis of HOSCN does not account for the observed intercepts of the k_{obs} vs. $[SCN^-]$ and k_{obs} vs. $[H^+]$ curves at pH 7 (Figure 23 and parameter ξ_9 in Table 5), which clearly indicates the presence of an alternative mechanism at pH $\geq$ 7 and $[SCN^-]_0 \leq [HOSCN]_{T,0}$. The disproportionation of $OSCN^-$ in a bimolecular reaction is a feasible explanation.[115,119] However, at pH > 11, $OSCN^-$ is known to hydrolyze to thiocarbamate S-oxide.[137]

A global data fit has been performed to validate our kinetic model: the complete experimental kinetic data set ($[SCN^-]$- and pH dependence at pH 4 and pH 7) has been fitted to the proposed model, with k_{obs} and the initial absorbances at 306 and 376 nm defined as dependent parameters, $[H^+]$ and $[SCN^-]$ defined as independent parameters, and k_{32}, k_{-32}, k_{33}, k_{34}, ξ_9, K_{31}, and E_5, E_6, E_7, E_8 as floating constants. The parameters E_5, E_6, E_7, E_8 are defined as the molar absorptivities of HOSCN at 306 and 376 nm and the molar absorptivities of $OSCN^-$ at 306 and 376 nm, respectively. The initial absorbances are calculated as follows:

$$A_0(306\text{nm}) = E_5[HOSCN]_0 + E_7[OSCN^-]_0$$

and (35)

$$A_0(376\text{nm}) = E_6[HOSCN]_0 + E_8[OSCN^-]_0$$

The kinetic model at Scheme 7 provides an excellent fit to the experimental data set. The resulting calculated constants are given in Table 8.

According to the intercorrelation between the hydrolysis of HOSCN and $(SCN)_2$, several identical steps are proposed in the two hydrolysis mechanisms. Scheme 8 illustrates the mechanism of decomposition of $(SCN)_2$. We account for the pH dependence of the initial spectrum of the $(SCN)_2$ solution around pH 4 by the protolytic equilibria -R33 and -R34, which are considered fast under the applied conditions. The equilibria -R33 and -R34 are competitive with the formation of

Table 8. Constants resulting from globally fitting the kinetic data of the hydrolysis of $(SCN)_2$ and $OSCN^-$ in the pH range from 4 to 7. The value of k_{-33} is overestimated, as the limiting rate of diffusion is ca. 10^{10} $M^{-1}s^{-1}$ in water.
\$Reference values can be found in the literature $K_{31} = 1.41 \times 10^{-5}$ M, $K_{35} = 0.43$ M^{-1}, $E_8 = 26.5$ M^{-1} cm^{-1}, $E_9 = 75 M^{-1}$ cm^{-1} and $E_{10} = 7500$ M^{-1} cm^{-1}. *: held fixed during the global data fit. #: calculated from other constants.

constant	estimated value	constant	estimated value
K_{31}	$(1.17 \pm 0.4) \times 10^{-5}$ M \$	$E_5\{HOSCN\}_{306nm}$	51 ± 2 $M^{-1}cm^{-1}$
K_{32}	50.0 ± 0.9 $M^{-1}s^{-1}$	$E_6\{HOSCN\}_{376nm}$	0 *
k_{-32}	$(2.07 \pm 0.09)\times10^3$ s^{-1}	$E_7\{OSCN^-\}_{306nm}$	13 ± 1 $M^{-1}cm^{-1}$
K_{32}	2.4×10^{-2} M^{-1} #	$E_8\{OSCN^-\}_{376nm}$	29 ± 1 $M^{-1}cm^{-1}$ \$
K_{33}	137 ± 23 s^{-1}	$E_9\{(SCN)_2\}_{300nm}$	75 $M^{-1}cm^{-1}$ \$*
k_{-33}	3.6×10^{11} $M^{-1}s^{-1}$ #	$E_{10}\{(SCN)_3^-\}_{300nm}$	7500 $M^{-1}cm^{-1}$ \$*
K_{-33}	$(2.65 \pm 0.3) \times 10^9$ M^{-1}	$E_{11}\{OH(SCN)_2^-\}_{300nm}$	1.6×10^3 $M^{-1}cm^{-1}$ #
K_{34}	$(1.29 \pm 0.07) \times 10^8$ $M^{-1}s^{-1}$		
k_{-34}	3.4×10^3 s^{-1} #		
K_{-34}	2.7×10^{-5} M #		
K_{35}	0.54 ± 0.1 M^{-1} \$		
K_{36}	$(4.01 \pm 0.3) \times 10^6$ $M^{-1}s^{-1}$		

$(SCN)_3^-$ in R35. Because limiting second order behavior is expected at low $[(SCN)_2]_T$, and limiting first order behavior is observed at high $[(SCN)_2]_T$, a reversible first-order step is proposed to precede a second-order step in the mechanism. We suggest that $OSCN^-$ is produced in the dissociation of $HO(SCN)_2^-$ in -R32 and that it subsequently reacts with $(SCN)_2$ in the rate limiting step R36. The simplest explanation for the undetectably low steady-state concentration of $OSCN^-$ under our experimental conditions is that $(SCN)_2$ reacts with $OSCN^-$ faster than the complete hydrolysis of $(SCN)_2$ can take place. The protonation state of the reacting species in R36 cannot be determined based on our kinetic experiments, because we were not able to measure the pH dependence of the hydrolysis of $(SCN)_2$ under second-order conditions, and all measurements were carried out at least 0.3 pH units below the pK_a of HOSCN (K_{31}). The properties of reaction R36 are discussed in detail later. In deriving the general rate law from the kinetic model of Scheme 8 describing the hydrolysis of $(SCN)_2$ at pH 4, equilibrium -R34 is omitted because $K_{-34} = K_{-33} \times K_w$ and because the deprotonated $OSCN^-$ is assumed to react with $(SCN)_2$ (R36). The fast equilibria are described as follows:

$$[(SCN)_2] = \frac{[(SCN)_2]_T}{1 + K_{35}[SCN^-] + K_{-33}[OH^-]}$$

and

$$[(SCN)_3^-] = \frac{K_{35}[SCN^-][(SCN)_2]_T}{1 + K_{35}[SCN^-] + K_{-33}[OH^-]} \qquad (36)$$

and

$$[OH(SCN)_2^-] = \frac{K_{-33}[OH^-][(SCN)_2]_T}{1 + K_{35}[SCN^-] + K_{-33}[OH^-]}$$

By defining R36 to be the rate limiting step and applying the steady-state approximation for $[HOSCN]_T$ in the simultaneous differential equation system of Scheme 8 we get the following:

$$v = -\frac{d[(SCN)_2]_T}{dt} = k_{36}[(SCN)_2][OSCN^-] \qquad (37)$$

$$[(SCN)_2]_T = [(SCN)_2] + [(SCN)_3^-] + [OH(SCN)_3^-]$$

$$v = \frac{(1-\alpha)k_{-32}k_{36}K_{-33}[\mathrm{OH^-}][(\mathrm{SCN})_2]_T^{\,2}}{\left(\alpha k_{32}[\mathrm{SCN^-}] + \frac{(1-\alpha)k_{36}[(\mathrm{SCN})_2]_T}{1+K_{-33}[\mathrm{OH^-}]+K_{35}[\mathrm{SCN^-}]}\right)\left(1+K_{-33}[\mathrm{OH^-}]+K_{35}[\mathrm{SCN^-}]\right)^2} \quad (38)$$

$$\alpha = \frac{[\mathrm{H^+}]}{K_{31}+[\mathrm{H^+}]}$$

For high $[(SCN)_2]_T$:

$$k_{32}(1+K_{-33}[\mathrm{OH^-}]+K_{35}[\mathrm{SCN^-}])[\mathrm{H^+}][\mathrm{SCN^-}] << k_{36}K_{31}[(\mathrm{SCN})_2]_T \quad (39)$$

and the limiting rate law is:

$$v = \frac{k_{-32}K_{-33}[\mathrm{OH^-}]}{1+K_{-33}[\mathrm{OH^-}]+K_{35}[\mathrm{SCN^-}]}[(\mathrm{SCN})_2]_T \quad (40)$$

Thus, reaction -R32 is rate-limiting when $[(SCN)_2]_T$ is high. The deduced rate law (eq. 40) is the same as the experimentally obtained rate law at high $[(SCN)_2]_{T,0}$ (see eq. 28). A global data fit has been performed: the experimental data set recorded at high $[(SCN)_2]_{T,0}$ was fitted to the limiting first order model (eq. 40) with k_{obs} and A_0^{CALC} as dependent variables, and $[SCN^-]$ and $[OH^-]$ as independent variables, and k_{-32}, K_{-33}, K_{35}, and E_9, E_{10}, E_{11} as floating constants. The last three constants are the molar absorbances of $(SCN)_2$, $(SCN)_3^-$ and $HO(SCN)_2^-$, in order, at 300 nm. The calculated initial molar absorbance at 300 nm is described by the following expression:

$$A_0^{CALC}(300\mathrm{nm}) = E_9[(\mathrm{SCN})_2]_0 + E_{10}[(\mathrm{SCN})_3^-]_0 + E_{11}[\mathrm{OH(SCN)_2^-}]_0 \quad (41)$$

The parameter k_{36} is approximated by fitting the following equation to the k_{obs} vs. $[(SCN)_2]_{T,0}$ curves recorded at different pH values (Figure 26):

$$k_{obs} = \frac{(1-\alpha)k_{-32}k_{36}K_{-33}[\mathrm{OH^-}][(\mathrm{SCN})_2]_{T,0}}{\left(\alpha k_{32}[\mathrm{SCN^-}] + \frac{(1-\alpha)k_{36}[(\mathrm{SCN})_2]_{T,0}}{1+K_{-33}[\mathrm{OH^-}]+K_{35}[\mathrm{SCN^-}]}\right)\left(1+K_{-33}[\mathrm{OH^-}]+K_{35}[\mathrm{SCN^-}]\right)^2} \quad (42)$$

$$\alpha = \frac{[\mathrm{H^+}]}{K_{31}+[\mathrm{H^+}]}$$

The experimental data set fits well to the proposed kinetic model and the obtained constants are listed in Table 8.

In spite of the high quality of the above presented global fits, the limiting rate laws and therefore the obtained parameters can be regarded only as approximations as seen for example in the value of k_{-33}, which exceeds 10^{10} $M^{-1}s^{-1}$. Although taking into consideration that numerous independently recorded data sets have been analyzed simultaneously without considering the error of the independent variables (i.e. initial concentrations and pH), the results are satisfactory. By substituting the values of Table 8 using $k_{-33} = 10^{10}$ $M^{-1}s^{-1}$ into to eqs. 32 and 39, we can predict that the limiting rate laws, i.e., eqs. 33 and 40 are valid at $[HOSCN]_T >> 2 \times 10^{-5}$M and at $[(SCN)_2]_T >> 1 \times 10^{-4}$M at pH 4.0, respectively.

The rate-limiting step in the decomposition of HOSCN and $(SCN)_2$ involves the reaction of $OSCN^-$ with $(SCN)_2$ (R36). In principle, the product of such a reaction could be the oxo derivative of the previously characterized $(SCN)_3^-$. Accordingly, we have described the reaction of $OSCN^-$ with $(SCN)_2$ (R36) as a substitution to give $O(SCN)_2$. The reaction is assumed to take place as a formal SCN^- for $OSCN^-$ substitution because $OSCN^-$ is not known to react as a direct O-donor.[127,173,178] Evidence for an asymmetric intermediate has been previously provided by radio-labeling studies, which demonstrated that SO_4^{2-} in a solution of $OSCN^-$ and SCN^- is derived exclusively from $OSCN^-$ at pH 7, indicating the conservation of the O–S bond. We therefore propose that the intermediate is NCS(=O)SCN. The proposed mechanism for the hydrolysis of NCS(=O)SCN as seen in Schemes 7 and 8 (R37 – R40) is based on an analogy with the halogens,[82,93,174] as no kinetic data are available for these fast reactions that take place after the rate limiting steps. We propose that NCS(=O)SCN can be formed over a wide range of pH (0 to 8), where $(SCN)_2$ and $OSCN^-$ coexist for some milliseconds, long enough for their reaction. However at high $[H^+]$ and $[SCN^-]$, reaction R36 becomes reversible and shifts towards the initial compounds. At lower $[H^+]$, the rapid hydrolysis of NCS(=O)SCN is assumed. At high $[OH^-]$, $(SCN)_2$ is quantitatively converted to $HO(SCN)_2^-$. Thus, the relative rate of formation of NCS(=O)SCN becomes negligible compared to the relative rate of formation of $OSCN^-$. No spectroscopic evidence was found for the production of the intermediate $HO(SCN)_2^-$ during the previous investigations of the hydrolysis of $(SCN)_2$ and the comproportionation of HOSCN and SCN^- in the pH range from 0 to 2.[115,119] The most probable explanation for this is that $HO(SCN)_2^-$ cannot exist at pH < 3 as $K_{-4} = 2.65\times10^{-5}$ ($pK_a((SCN)_2) = 4.58$). The intermediate $HO(SCN)_2^-$ can only be a minor transient

species in the hydrolysis of $(SCN)_2$ to give $OSCN^-$ at pH > 8 because -R33 is a fast equilibrium, and -R32 is shifted to the left with the deprotonation of HOSCN.

The stoichiometry of the hydrolytic decomposition of HOSCN and $(SCN)_2$ determined by IC (Table 7) differs significantly from the predicted stoichiometry given in Schemes 7 and 8. We propose that as the concentration of CN^- increases during decomposition, its reaction with HOSCN becomes competitive among the fast reactions (Scheme 9, R44-R45). The pH dependent rate of R44 is maximal around pH 7, which predicts the observed increase in the OCN^- production in the hydrolysis.[127] Some calculated values in Table 7 indicate the contribution of R46 to the overall decomposition of $(SCN)_2$ and $OSCN^-$. At pH 7, the SCN^- production is smaller and the OCN^- production is larger than anticipated, which is another piece of evidence for an alternative hydrolysis pathway under these conditions. The stoichiometry of the reactions at pH 7 can only be balanced with the inclusion of the production of elementary sulfur (which was detected only by ESI-MS), however, the mechanism of its formation is not clear.

Scheme 9. Mechanism of the reaction of $OSCN^-$ with HCN below pH 7.

$HOSCN \rightleftharpoons OSCN^- + H^+$	fast equilibrium	(R31)
$HCN \rightleftharpoons CN^- + H^+$	fast equilibrium	(R43)
$HOSCN + CN^- \rightarrow NCSCN + OH^-$	$\boldsymbol{k_{44}} = 7.5\times10^7\ M^{-1}s^{-1}$	(R44)
$NCSCN + OH^- \rightarrow OCN^- + SCN^- + H^+$	$\boldsymbol{k_{45}} < 100\ M^{-1}s^{-1}$ (pH < 7), r.d.s.	(R45)
$HOSCN + HCN \rightarrow OSCN^- + SCN^- + 2\ H^+$		(R46)

5.4.5) *Biological relevance*

Several important conclusions can be drawn with respect to the biological relevance of the results described herein. First, it is difficult to imagine $(SCN)_2$ playing a significant role as a biological reactive intermediate at neutral pH in an aqueous environment. The usual pathway to produce $(SCN)_2$, comproportionation of $OSCN^-$ and SCN^-, is magnitudes slower[115] than the reaction of $(SCN)_2$ with $OSCN^-$. Thus, as soon as $(SCN)_2$ is formed, it is already consumed through its reaction with $OSCN^-$, which process also depletes the concentration of $OSCN^-$. Furthermore, if other pathways exist for producing $(SCN)_2$, it is unlikely that $(SCN)_2$ plays a role in aqueous environments where the concentration of $OSCN^-$ is significant (as a consequence of the facile reaction R36), especially in the mucosae where the steady-state concentration of $OSCN^-$ can achieve high micromolar concentrations. Second, we have shown that no mechanistic proposals which involve $(SCN)_2$ as a precursor can be feasible for the formation of $OSCN^-$ at neutral pH[94,122,138,179,180,181,182] because these species are nor in dynamic equilibrium neither the product of hydrolysis of $(SCN)_2$ is $OSCN^-$. Furthermore, $OSCN^-$ and $(SCN)_2$ cannot coexist longer than a few milliseconds at neutral pH, thus previous mechanistic proposals for the formation of HOSCN in the LPO-system that invoke $(SCN)_2$ as an intermediate during the enzymatic oxidation of SCN^- with H_2O_2 cannot be correct. Based on these conclusions, the biochemical role of $(SCN)_2$ is questionable. Third, based on the kinetic data, we have confirmed that relatively short-lived derivatives of $OSCN^-$ are produced during the decomposition of $OSCN^-$, including the $O(SCN)_2$, which we have formulated as NCS(=O)SCN. It is unlikely that $O(SCN)_2$ contains a symmetrical –S–O–S– linkage, as has been suggested in some early literature in the field.[183] Fourth, we found that a high relative concentration of OCN^- is produced during the decomposition of $OSCN^-$ at neutral pH. This raises the question of whether the observed MPO-catalyzed carbamylation of proteins in sites of inflammation is caused by OCN^- as a direct product of the enzymatic oxidation of SCN^-, or whether the OCN^- concentration is elevated because of the decomposition of the excess $OSCN^-$ present.[184]

6) SUMMARY

The activation parameters and the rate constants of the water exchange reactions of MnTE-2-PyP^{5+} (Mn(III) meso-tetrakis(N-ethylpyridinium-2-yl)porphyrin) as cationic, MnTnHex-2-PyP^{5+} (Mn(III) meso-tetrakis(N-n-hexylpyridinium-2-yl)-porphyrin) and MnTTEG-2-PyP^{5+} (Mn(III) meso-tetrakis(N-tri(ethyleneglycol)-pyridinium-2-yl)porphyrin) as sterically shielded cationic, and MnTSPP^{3-} (meso-tetrakis(4-sulfonatophenyl)porphyrin) as anionic Mn(III) porphyrins have been determined from the temperature dependence of ^{17}O NMR relaxation rates. On the basis of the determined entropies of activation, an interchange-dissociative mechanism (I_d) was proposed for the cationic complexes ($\Delta S^{\ddagger}$ = ca. 0 J K^{-1} mol^{-1}) whereas a limiting dissociative mechanism (D) was proposed for MnTSPP^{3-} complex ($\Delta S^{\ddagger}$ = +79 J K^{-1} mol^{-1}). The obtained water exchange rate of MnTSPP^{3-} corresponded well to the previously assumed value used by Koenig et al. to simulate the ^{1}H NMRD curves, therefore the measured value supports the theory developed for explaining the anomalous relaxivity of MnTSPP^{3-} complex. The magnitude of the obtained water exchange rate constants further confirms the suggested inner-sphere electron transfer mechanism for the reactions of the two positively charged Mn(III) porphyrins with the described biologically important oxygen and nitrogen reactive species.

We found that the *in vitro* autoxidation of N-hydroxyurea (HU) is catalyzed by MnTTEG-2-PyP^{5+}, which is also a potent mimic of the enzyme superoxide dismutase. The detailed mechanism of the reaction is deduced from kinetic studies under basic conditions mostly based on data measured at pH 11.7 but also including some pH dependent observations in the pH range from 9 to 13. The major intermediates were identified by UV-vis spectroscopy and electrospray ionization mass spectrometry. The reaction starts with a fast axial coordination of HU to the metal center of MnTTEG-2-PyP^{5+}, which is followed by a ligand-to-metal electron transfer to get Mn^{II}TTEG-2-PyP^{4+} and the free radical derived from HU (HU$^{\bullet}$). Nitric oxide (NO) and nitroxyl (HNO) are minor intermediates. The major pathway for the formation of the most significant intermediate, the {Mn^{II}NO}^{7} complex of Mn^{II}TTEG-2-PyP^{4+}, is the reaction of Mn^{II}TTEG-2-PyP^{4+} with NO. We have confirmed that the autoxidation of the intermediates open alternative reaction channels, and the process finally yields NO_2^- and the initial

Mn^{III}TTEG-2-PyP^{5+}. The photochemical release of NO from the $\{Mn^{II}NO\}^7$ intermediate was also studied. Kinetic simulations have been performed to validate the deduced rate constants.

We reported a detailed mechanistic investigation on the multistep oxidation of excess SCN^- with peroxomonosulfate ion (HSO_5^- in the form of Oxone®) in the pH range from 6.5 to 13.5. Hypothiocyanite ion ($OSCN^-$) was detected to be the intermediate of this reaction under the above conditions, and a kinetic model is proposed. Furthermore, by kinetically separating the consecutive reaction steps, the rate constant of the direct oxidation of $OSCN^-$ by HSO_5^- was determined. A critical evaluation of the estimated activation parameters of the elementary steps has revealed that the oxidations of SCN^- as well as the consecutive $OSCN^-$ by HSO_5^- are more likely to proceed via two electron transfer steps. The catalytic effect of MnTMe-4-PyP^{5+} on the $HSO_5^- + SCN^-$ reaction was also demonstrated and investigated. The catalytically important intermediate in the process is proposed to be the Mn^V(O) porphyrin which forms in the reaction of HSO_5^- + MnTMe-4-PyP^{5+}. Furthermore the reactivity of the Mn^{IV}(O) species towards SCN^- is also described.

We discussed that $OSCN^-$ can engage in a cascade of pH- and concentration dependent comproportionation, disproportionation, and hydrolysis reactions that control its stability in water. Based on reaction kinetic, spectroscopic, and chromatographic methods, a detailed mechanism is proposed for the decomposition of $OSCN^-$ in the pH range of 4 to 7 to eventually give the simple inorganic anions CN^-, OCN^-, SCN^-, SO_3^{2-}, and SO_4^{2-}. Thiocyanogen ($(SCN)_2$) is proposed to be a key intermediate in the hydrolysis; and the facile reaction of $(SCN)_2$ with $OSCN^-$ to give the assumed NCS(=O)SCN, a previously unknown reactive sulfur species, has been independently investigated. The mechanism of the aqueous decomposition of $(SCN)_2$ around pH 4 is also reported. The resulting mechanistic models for the decomposition of HOSCN and $(SCN)_2$ address previous empirical observations, including the facts that the presence of SCN^- and/or $(SCN)_2$ decreases the stability of HOSCN/$OSCN^-$, that radioisotopic labeling provided evidence that under physiological conditions decomposing $OSCN^-$ is not in equilibrium with $(SCN)_2$ and SCN^-, and that the hydrolysis of $(SCN)_2$ does not produce $OSCN^-$ near neutral pH. Accordingly, we demonstrated that during the human peroxidase-catalyzed oxidation of SCN^-, $(SCN)_2$ cannot be the precursor of the $OSCN^-$ that is produced.

7) ÖSSZEFOGLALÁS

Változó hőmérsékleteken végzett ^{17}O-NMR relaxációs mérések segítségével meghatároztuk a kationos MnTE-2-PyP^{5+} (Mn(III)-mezo-tetra(N-etilpiridínium-2-il)-porfirin), a sztérikusan zsúfolt kationos MnTnHex-2-PyP^{5+} (Mn(III)-mezo-tetra(N-n-hexilpiridínium-2-il)-porfirin) és MnTTEG-2-PyP^{5+} (Mn(III)-mezo-tetra-(N-tri(etilénglikol)piridínium-2-il)-porfirin), valamint az anionos MnTSPP^{3-} (mezo-tetra(4-szulfonátofenil)-porfirin) komplexek pH = 6 körül érvényes vízcsere sebességi állandóját és aktiválási paramétereit. A 298 K-re vonatkozó sebességi állandók rendre a következők: $4{,}12 \times 10^6$ s^{-1}; $5{,}73 \times 10^6$ s^{-1}; $4{,}88 \times 10^6$ s^{-1} és $2{,}74 \times 10^7$ s^{-1}. A meghatározott aktiválási entrópiák alapján arra következtettünk, hogy a kationos komplexek vízcseréjének mechanizmusa ($\Delta S^{\ddagger}$ = kb. 0 J K^{-1} mol^{-1}) átmenetet mutat a disszociatív és az asszociatív között, míg az anionos komplexé (ΔS = +79 J K^{-1} mol^{-1}) egyértelműen disszociatív jellegű. A MnTSPP^{3-} esetén kapott vízcsere-sebességi állandó jó közelítéssel megegyezik a Koenig és munkatársai által becsülttel, amivel sikeresen szimulálták ezen komplex ^{1}H NMRD görbéit. Kijelenthetjük tehát, hogy az általunk mért vízcsere-sebességi állandó alátámasztja a MnTSPP^{3-} komplex anomáliás relaxivitására kidolgozott elméleteket. A szuperoxidgyök és a MnTE-2-PyP^{5+} között lejátszódó redoxireakció másodrendű sebességi állandójából a Fouss-egyenlet segítségével megbecsültük a belső szférás elektrontranszfer lejátszódásához szükséges víz – reaktáns ligandumcsere sebességi állandóját. Ez az állandó nagyságrendileg megegyezik a Mn(III)porfirin komplex disszociatív vízcseréjének sebességi állandójával. Ebből arra következtettünk, hogy a Mn(III)centrum és a szuperoxidgyök közötti reakció sebességmeghatározó lépése ténylegesen a reaktáns belső szférás koordinációja a Mn(III)centrumhoz.

Megfigyeltük, hogy az N-hidroxi-karbamid (HU) *in vitro* autooxidációját lúgos körülmények között katalizálja a szuperoxid-diszmutáz enzim utánzására is képes MnTTEG-2-PyP^{5+} szintetikus Mn(III)-porfirin komplex. A reakció mechanizmusának tanulmányozására tervezett reakciókinetikai vizsgálataink nagy részét pH = 11,70-en végeztük, amit kiegészítettünk néhány, a folyamat pH-függését vizsgáló kísérlettel a pH = 9 – 13 tartományban. A MnTTEG-2-PyP^{5+} és HU közötti reakció során felhalmozódó fő köztitermékeket UV-látható spektroszkópiás és elektroporlasztásos ionizációs tömegspektrometriai (ESI-MS) mérésekkel

azonosítottuk. A folyamat a HU gyors axiális koordinálódásával kezdődik a MnTTEG-2-PyP^{5+} fémcentrumára, amit a ligandumról fémre irányuló elektronátadás követ, Mn^{II}TTEG-2-PyP^{4+} porfirint és N-hidroxi-karbamid-gyököt (HU$^{\bullet}$) eredményezve. Az HU$^{\bullet}$ gyökből nitrogén-monoxid (NO) és nitroxil (HNO) is keletkezik a további folyamatok során. A folyamat során legnagyobb mennyiségben felhalmozódó köztiterméket, azaz a Mn^{II}TTEG-2-PyP^{4+} porfirin {Mn^{II}NO}^{7} típusú komplexét a Mn^{II}TTEG-2-PyP^{4+} porfirin és a NO reakciója termeli. Kísérleti bizonyítékot szolgáltattunk arra nézve, hogy a különböző köztitermékek autooxidációs folyamatai új reakcióutakat nyitnak. Ionkromatográfiás (IC) és spektroszkópiás mérésekkel megerősítettük, hogy a MnTTEG-2-PyP^{5+} és HU közötti reakció végtermékei a változatlan Mn(III) porfirin és a nitrition (NO_2^-). Tanulmányoztuk továbbá a {Mn^{II}NO}^{7} komplex fotokémiai bomlását is. A javasolt kinetikai modell validálására szimulációkat végeztünk, melyek jó egyezést mutatnak a kísérletileg mért kinetikai görbékkel.

Részletesen bemutattuk a tiocianátion (SCN^-) és a peroxomonoszulfát-ion (HSO_5^-, Oxone®-ként formulálva) között SCN^- felesleg mellett semleges és lúgos közegben lejátszódó reakciójának kinetikáját és mechanizmusát. A több lépéses oxidációs reakció spektroszkópiai módszerekkel jól detektálható köztitermékeként a hipotiocianit-iont ($OSCN^-$) azonosítottuk. Ez a részecske lúgos közegben SCN^- feleslege mellett egyik viszonylagosan stabil végterméke is a folyamatnak. A lejátszódó folyamatok leírására kinetikai modellt javasoltunk. Elvégeztük az egymást követő oxidációs lépések kinetikájának matematikai leírását, így méréseinkből közvetlenül tudtuk számolni a $OSCN^-$ és a HSO_5^- közti redoxreakció sebességi állandóját: $k_{21} = (1{,}6 \pm 0{,}1) \times 10^2\ M^{-1}\ s^{-1}$ lúgos körülmények között (pH = 13,5) és $k_{21}^{H} = (3{,}3 \pm 0{,}1) \times 10^3\ M^{-1}\ s^{-1}$ semleges körülmények között (pH = 6,89). Meghatároztuk az elemi reakciólépések aktiválási paramétereit, és ezek kritikai értékelését követően javaslatot tettünk az elemi reakciók mechanizmusára. Véleményünk szerint mind a SCN^-, mind a $OSCN^-$ peroxomonoszulfát-ionnal történő oxidációja során valószínűleg két elektron együttes átadása történik. Vizsgáltuk a MnTMe-4-PyP^{5+} Mn(III)-porfirin komplex az előbbi reakciókra kifejtett katalitikus hatását. Megállapítottuk, hogy a porfirinkomplex jelenléte gyorsítja a SCN^- oxidációját, és megmutattuk, hogy a katalitikusan aktív köztitermék nagy valószínűséggel a Mn^{V}(O)-porfirin. Ez a

részecske közvetlenül képződik a HSO_5^- és a MnTMe-4-PyP^{5+} reakciójában, és eredményeink szerint képes a SCN^- gyors oxidálására.

Részletesen vizsgáltuk a ditiocián ($(SCN)_2$) és a $OSCN^-$ hidrolitikus stabilitását befolyásoló tényezőket enyhén savas és semleges közegben (pH = 4 – 7). Mind kémiai, mind matematikai eszközökkel részletesen tanulmányoztuk és leírtuk azokat a bonyolult pH- és koncentráció-függő reakciórendszereket, melyek a fenti részecskék hidrolízise során kialakulnak. Reakciókinetikai, UV-látható és tömegspektrometriai, valamint kromatográfiás mérések alapján mechanizmust javasoltunk az $OSCN^-$ semleges és enyhén savas közegben bekövetkező hidrolitikus bomlásának mechanizmusára. Bizonyítottuk, hogy a bomlástermékek egyszerű szervetlen anionok: CN^-, OCN^-, SCN^-, SO_3^{2-}, és SO_4^{2-}. Megfigyeléseink szerint a $(SCN)_2$ kulcsfontosságú köztiterméke az $OSCN^-$ hidrolízisének, azonban a folyamat során nem halmozódik fel. Független kísérletekben sikerült kimutatnunk, hogy a $(SCN)_2$ enyhén savas közegben reagál a hipotiocianit-ionnal. Ezen reakció termékének szerkezetére javaslatot tettünk (NCS(=O)SCN). Kulcsfontosságú szerepe miatt a $(SCN)_2$ hidrolízisét is vizsgáltuk pH = 4 körül, és megmutattuk, hogy ilyen körülmények között a $(SCN)_2$ hidrolízise nem termel kimutatható mennyiségű hipotiocianit-ion. A fenti részecskék hidrolízésére javasolt kinetikai modellek összhangban vannak a korábbi empirikus megfigyelésekkel, miszerint a SCN^- és a $(SCN)_2$ jelenléte csökkenti a $OSCN^-$ stabilitását, továbbá, hogy a $OSCN^-$ enyhén savas pH-n nincs egyensúlyban $(SCN)_2$ és SCN^- elegyével. Ezzel azt is demonstráltuk hogy a humán peroxidáz enzimek által katalizált $SCN^- + H_2O_2$ oxidációs reakciónak nem lehet a $(SCN)_2$ a közvetlen terméke, hiszen ennek a részecskének a hidrolízise fiziológiás körülmények között nem szolgáltathatja a felhalmozódó hipotiocianit-iont.

8) LIST OF PUBLICATIONS

Publications covered in the thesis:

4) Detailed kinetics and mechanism of the oxidation of thiocyanate ion (SCN^-) by peroxomonosulfate ion (HSO_5^-). Formation and subsequent oxidation of hypothiocyanite ion ($OSCN^-$)
J. Kalmár*, G. Lente, I. Fábián
Inorganic Chemistry, **2013**, 52 (4), 2150-2156. *IF(2011): 4.60*

3) Detailed mechanism of the autoxidation of N-hydroxyurea catalyzed by a superoxide dismutase mimic Mn(III) porphyrin: formation of the nitrosylated Mn(II) porphyrin as an intermediate
J. Kalmár, B. Biri, G. Lente*, I. Bányai, A. Budimir, M. Biruš, I. Batinić-Haberle, I. Fábián
Dalton Transactions, **2012**, 41 (38), 11875-11884. *IF(2011): 3.84*

2) Mechanism of decomposition of the human defense factor hypothiocyanite near physiological pH
J. Kalmár, K. L. Woldegiorgis, B. Biri, M. T. Ashby*
Journal of the American Chemical Society, **2011**, 133 (49), 19911-19921. *IF(2011): 9.91*

1) Water exchange rates of water-soluble manganese(III) porphyrins of therapeutical potential
A. Budimir, J. Kalmár*, I. Fábián, G. Lente, I. Bányai, I. Batinić-Haberle, M. Biruš*
Dalton Transactions, **2010**, 39 (18), 4405-4410. *IF(2010): 3.65*

Summa IF: 22.00

Other publications:

5) Kinetics of formation of the host–guest complex of a viologen with cucurbit[7]uril
J. Kalmár, S. B. Ellis, M. T. Ashby, R. L. Halterman*
Organic Letters, **2012**, 14 (13), 3248-3251. *IF(2011): 5.86*

4) Collision induced dissociation study of the major components of silymarin
Á. Kuki, B. Biri, L. Nagy, Gy. Deák, J. Kalmár, M. Nagy, M. Zsuga, S. Kéki*
International Journal of Mass Spectrometry, **2012**, 315, 46-54. *IF(2011): 2.55*

3) Energy-dependent collision-induced dissociation study of buprenorphine and its synthetic precursors
B. Biri, J. Kalmár, L. Nagy, A. Sipos, M. Zsuga, S. Kéki*
Rapid Communications in Mass Spectrometry, **2011**, *25* (1), 41-49.
IF(2011): 2.79

2) Hydrochemical study of the source region of Ier (Ér) stream in Satu Mare (Szatmár) County, Romania
J. Kalmár*, M. Braun, I. Fábián
Studia Universitatis Vasile Goldis, Life Sciences Series, **2010**, *20* (4), 57-65.
IF(2010): Ø

1) One-versus two-electron oxidation with peroxomonosulfate ion: Reactions with iron(II), vanadium(IV), halide ions, and photoreaction with cerium(III)
G. Lente*, J. Kalmár, Zs. Baranyai, A. Kun, I. Kék, D. Bajusz, M. Takács, L. Veres, I. Fábián
Inorganic Chemistry, **2009**, 48 (4), 1763-1773. *IF(2009): 4.66*

Summa IF: 15.86

9) REFERENCES

1) Groves, J. T.; Shalyaev, K; Lee, J *The Porphyrin Handbook 1st Edition* **1999** (Elsevier), Vol. 4, pp. 17.

2) Susulick, K. *The Porphyrin Handbook 1st Edition* **1999** (Elsevier), Vol. 4, pp. 41.

3) Muenier, B; Robert, A.; Pratviel, G.; Bernadou, J. *The Porphyrin Handbook 1st Edition* **1999** (Elsevier), Vol. 4, pp. 119.

4) Aida, T.; Inoue, S. *The Porphyrin Handbook 1st Edition* **1999** (Elsevier), Vol. 6, pp. 133.

5) Hambright, P. *The Porphyrin Handbook 1st Edition* **1999** (Elsevier), Vol. 3, pp. 129.

6) Fukuzimi, S. *The Porphyrin Handbook 1st Edition* **1999** (Elsevier), Vol. 8, pp. 115.

7) Poulos, T. L. *The Porphyrin Handbook 1st Edition* **1999** (Elsevier), Vol. 4, pp. 189.

8) Cheng, L.; Richter-Addo, G. *The Porphyrin Handbook 1st Edition* **1999** (Elsevier), Vol. 4, pp. 219.

9) Miriyala, S.; Spasojevic, I.; Tovmasyan, A.; Salvemini, D.; Vujaskovic, Z.; St Clair, D.; Batinic-Haberle, I. *Biochim. Biophys. Acta* **2012**, *1882*, 794-814.

10) Halliwell, I. B.; Gutteridge, J. M. C. *Free Radicals in Biology and Medicine 4th Edition* **2007**, (Biosciences, Oxford).

11) Spasojević, I.; Batinić-Haberle, I. *Inorg. Chim. Acta* **2001**, *317*, 230-242.

12) Batinić-Haberle, I. *Methods Enzymol.* **2002**, *349*, 223-233.

13) Batinić-Haberle, I.; Spasojević, I.; Hambright, P.; Fridovich, I. *J. Chem. Soc. Dalton Trans.* **2002**, *30*, 2689-2696.

14) (a) Batinić-Haberle, I.; Rajic, Z.; Tovmasyan, A.; Reboucas, J. S.; Ye, X.; Leong, K. W.; Dewhirst, M. W.; Vujaskovic, Z.; Benov, L.; Spasojević, I. *Free Radic. Biol. Med.* **2011**, *51*, 1035-1053.

(b) Aslan, M.; Ryan, T. M.; Adler, B.; Townes, T. M.; Parks, D. A.; Thompson, J. A.; Tousson, A.; Gladwin, M. T.; Patel, R. P.; Tarpey, M. M; Batinić-Haberle, I.; White, C. R.; Freeman, B. A. *Proc. Nat. Acad. Sci. USA* **2001**, *98*, 15215-15220.

15) (a) Jaramillo, M. C.; Briehl, M. M.; Crapo, J. D.; Batinić-Haberle, I.; Tome, M. E. *Free Radic. Biol. Med.* **2012**, *52*, 1272-1284.

(b) Rajic, Z.; Tovmasyan, A.; Spasojevic, I.; Sheng, H.; Lu, M; Gralla, E. B.; Warner, D. S.; Benov, L.; Batinić-Haberle, I. *Free Radical Biol. Med.* **2012**, *52*, 1828-1834.

(c) Miriyala, S.; Tovmasyan, A.; Spasojević, I.; Salvemini, D.; Vujasković, Z; St.Clair, D. K.; Batinić-Haberle, I. *Biochim. Biophys. Acta* 2012, 1822, 792-814.

16) Lahaye, D.; Muthukumaran, K.; Hung, C.-H.; Gryko, D.; Rebouças, J. S.; Spasojević, I.; Batinić-Haberle, I.; Lindsey, J. S. *Bioorg. Med. Chem.* **2007**, *15*, 7066-7086.

17) J. S. Rebouças, I. Spasojević, D. H. Tjahjono, A. Richaud, F. Méndez, L. Benov and I. Batinić-Haberle, *Dalton Trans.* **2008**, *6*, 1233-1242.

18) Batinić-Haberle, I.; Benov, L.; Spasojević, I.; Fridovich, I. *J. Biol. Chem.* **1998**, *273*, 24521-24528.

19) Batinić-Haberle, I.; Spasojević, I.; Stevens, R. D.; Bondurant, B.; Okado-Matsumoto, A.; Fridovich, I.; Vujasković, Ž.; Dewhirst, M. W. *Dalton Trans.*, **2006**, *4*, 617-624.

20) Batinić-Haberle, I.; Spasojević, I.; Hambright, P.; Benov, L.; Crumbliss, A. L.; Fridovich, I. *Inorg. Chem.* **1999**, *38*, 4011-4022.

21) Batinić-Haberle, I.; Spasojević, I. Stevens, R. D.; Hambright, P.; Neta, P.; Okado-Matsumoto, A.; Fridovich, I. *Dalton Trans.* **2004**, *2*, 1696-1702.

22) Okado-Matsumoto, A.; Batinić-Haberle, I.; Fridovich, I. *Free Radical Biol. Med.*, **2004**, *37*, 401-410.

23) Moeller, B.J.; Batinić-Haberle, I; Spasojević, I.; Rabbani, Z. N.; Anscher, M. S.; Vujasković, Ž.; Dewhirst, M. W. *Int. J. Rad. Oncol. Biol. Phys.*, **2005**, *63*, 545-552.

24) Spasojević, I.; Chen, Y.; Noel, T. J.; Yu, Y.; Cole, M. P.; Zhang, L.; Zhao, Y.; StClair, D. K.; Batinić-Haberle, I. *Free Radical Biol. Med.* **2007**, *42*, 1193-1200.

25) Saba, H.; Batinić-Haberle, I.; Munusamy, S.; Mitchell, T.; Lichti, C.; Megyesi J.; MacMillan-Crow, L. A. *Free Radical Biol. Med.* **2007**, *42*, 1571-1578.

26) Rabbani, Z. N.; Spasojević, I.; Zhang, X.; Moeller, B. J.; Vasquez-Vivar, J.; Dewhirst, M. W.; Vujasković, Ž.; Batinić-Haberle, I. *Free Radical Biol. Med.* **2009**, *47*, 992-1004.

27) Ferrer-Sueta, G.; Vitturi, D.; Batinić-Haberle, I.; Fridovich, I.; Goldstein, S.; Czapski G.; Radi, R. J.; *J. Biol. Chem.* **2003**, *278*, 27432-27438.

28) Batinić-Haberle, I.; Reboucas, J. S.; Spasojević, I. *Antioxid. Redox Signal.* 2010, 13, 877-918.

29) Filipović, M. R.; Duerr, K.; Mojović, M.; Simeunović, V.; Zimmermann, R.; Niketić, V.; Ivanović-Burmazović, I.; *Angew. Chem. Int. Ed.* **2008**, *47*, 8735-8739.

30) Filipović, M. R.; Koh, A. C. W.; Arbault, S.; Niketić, V.; Debus, A.; Schleicher, U.; Bogdan, C.; Guille, M.; Lemaître, F.; Amatore, C.; Ivanović-Burmazović, I. *Angew. Chem. Int. Ed.* **2010**, *49*, 4228-4232.

31) Reboucas, J. S.; DeFreitas-Silva, G.; Idemori, Y. M.; Spasojević, I.; Benov, L.; Batinić-Haberle, I. *Free Radical Biol. Med.* **2008**, *45*, 201-210.

32) Ivanović-Burmazović, I.; van Eldik, R. *Dalton Trans*. **2008**, *6*, 5259-5275.

33) Lieb, D.; Zahl, A.; Shubina, T. E.; Ivanović-Burmazović, I. *J. Am. Chem. Soc*. **2010**, *132*, 7282-7284.

34) Spasojević, I.; Batinić-Haberle, I.; Reboucas, J. S.; Idemori, Y. M.; Fridovich, I. *J. Biol. Chem.* **2003**, *278*, 6831-6837.

35) Giovannetti, R.; Alibabaei, L.; Pucciarelli, F. *Inorg. Chim. Acta* **2010**, *363*, 1561-1567.

36) Abu-Omar, M. M. *Dalton Trans.* **2011**, *40*, 3435-3444.

37) Mahmoudi, L.; Mohajer, D.; Kissner, R.; Koppenol, W. H. *Dalton Trans.* **2011**, *40*, 8695-8700.

38) Harriman, A.; Porter, G. *J. Chem. Soc. Faraday Trans. 2*, **1979**, *75*, 1532-1544.

39) Weitner, T.; Budimir, A.; Kos, I.; Batinić-Haberle, I.; Biruš, M. *Dalton Trans.* **2010**, *39*, 11568-11576.

40) Nelson, J. A.; Schmiedl, U. *Magn. Reson. Med.* **1991**, *22*, 366-371.

41) Nasu, H.; Takehara, Y.; Isogai, S.; Kodaira, N.; Takeda, H.; Saga, T.; Nakajima, S.; Sakata I.; Sakahara, H. *J. Magn. Reson. Imaging* **2004**, *20*, 294-299.

42) Fiel, R. J.; Musser, D. A.; Mark, E. H.; Mazurchuk, R.; Alletto, J. J. *Magn. Reson. Imaging* **1990**, *8*, 255-259.

43) Nelson, J. A.; Schmiedl, U.; Shankland, E. G. *Invest. Radiol.* **1990**, *25*, S71-S73.

44) Yushmanov, V. E.; Tominaga, T. T.; Borissevitch, I. E.; Imasato, H.; Tabak, M. *Magn. Reson. Imaging* **1996**, *14*, 255-261.

45) Place, D. A.; Faustino, P. J.; Berghmanns, K. K.; van Zijl, P. C. M.; Chesnick, A. S.; Cohen, J. S. *Magn. Reson. Imaging* **1992**, *10*, 919-928.

46) Klein, A. T. J.; Rösch, F.; Coenen, H. H.; Qaim, S. M. *Appl. Radiat. Isot.* **2005**, *62*, 711-720.

47) Mouraviev, V.; Venkatraman, T. N.; Tovmasyan, A.; Kimura, M.; Tsivian, M.; Mouravieva, V.; Polascik, T. J.; Wang, H.; Amrhein, T. J.; Batinić-Haberle, I.; Lascola, C. *J. Endourology* **2012**, 26, 1420-1424.

48) Bohuslav, D.; Lukeš, I.; Tóth, É. *Eur. J. Inorg. Chem.* **2012**, *12*, 1975-1986.

49) Schaefle, N.; Sharp, R. *J. Phys. Chem. A* **2005**, *109*, 3267-3275.

50) Koenig, S. H.; Brown, R. D.; Spiller, M. *Magn. Reson. Med.* **1987**, *4*, 252-260.

51) Sur, S. K.; Bryant, R. G.; *J. Phys. Chem.* **1995**, *99*, 4900-4905.

52) Blombergen, M.; Morgan, L. *J. Chem. Phys.* **1961**, *34*, 842-850.

53) Schneppesieper, T.; Zahl, A.; van Eldik, R. *Angew. Chem. Int. Ed.* **2001**, *40*, 1678-1680.

54) Ostrich, I. J.; Liu, G.; Dodgen, H. W.; Hunt, P. J. *Inorg. Chem.* **1980**, *19*, 619-621.

55) Piver, M. S.; Barlow, J. J.; Vongtama, V.; Webster, J. *Am. J. Obstet. Gynecol*. **1974**, *120*, 969-972.

56) Piver, M. S.; Barlow, J. J.; Vongtama, V.; Blumenson, L. *Am. J. Obstet. Gynecol*. **1977**, *129*, 379-383.

57) Boyd, A. S.; Neldner, K. H. *J. Am. Acad. Dermatol.* **1991**, *25*, 518-524.

58) Burkitt, M. J.; Raafat, A. *Blood* **2006**, *107*, 2219-2222.

59) Charache, S.; Terrin, M. L.; Moore, R. D.; Dover, G. J.; Barton, F. B.; Eckert, S. V.; McMahon, R. P.; Bonds, D. R. *N. Engl. J. Med*. **1995**, *332*, 1317-1322.

60) Charache, S.; Barton, F. B.; Moore, R. D.; Terrin, M. L; Steinberg, M. H.; Dover, G. J.; Ballas, S. K.; McMahon, R. P.; Castro, O.; Orringer, E. P. *Medicine* **1996**, *75*, 300-326.

61) Ferguson, R. P.; Arun, A., Carter, C.; Walker, S. D.; Castro, O. *Am. J. Hematol*. **2002**, *70*, 326-330.

62) Steinberg, M. H.; Barton, F.; Castro, O.; Pegelow, C. H.; Ballas, S. K., Kutlar, A.; Orringer, E.; Bellevue, R., Olivieri, N.; Eckman, J.; Varma, M.; Ramirez, G.; Adler, B.; Smith, W.; Carlos, T.; Ataga, K.; DeCastro, L.; Bigelow, C.; Sauntharajah, Y.; Telfer, M.; Vichinsky, E.; Claster, S.; Shurin, S.; Bridges, K.; Waclawiw, M.; Bonds, D.; Terrin, M. *JAMA* **2003**, *289*, 1645-1651.

63) Bridges, K.; Barabino, G.; Brugnara, C.; Cho, M.; Christoph, G.; Dover, G.; Ewenstein, B.; Golan, D.; Guttmann, C.; Hofrichter, J.; Mulkern, R.; Zhang, B.; Eaton, W. *Blood* **1996**, *88*, 4701-4710.

64) Bundy, R.; Marczin, N.; Chester, A. H.; Yacoub, M. *Am. J. Physiol. Heart. - Circ. Physiol*. **1999**, *277*, H1799-1807.

65) Glover, R. E.; Ivy, E. D.; Orringer, E. P.; Maeda, H.; Mason, R. P.; *Mol. Pharmacol*. **1999**, *55*, 1006-1010.

66) Gladwin, M. T.; Shelhamer, J. H.; Ognibene, F. P.; Pease-Fye, M. E.; Nichols, J. S.; Link, B.; Patel, D. B.; Jankowski, M. A.; Pannell, L. K.; Schechter, A. N.; Rodgers, G. P. *Brit. J. Haematol*. **2002**, *116*, 436-444.

67) Cokic, V. P.; Smith, R. D.; Beleslin-Cokic, B. B.; Njoroge, J. M.; Miller, J. L.; Gladwin, M. T.; Schechter, A. N. *J. Cliv. Invest*. **2003**, *111*, 231-239.

68) Marmion, C. J.; Murphy, T. T.; Nolan, K. B.; Docherty, J. R. *Chem. Commun*. **2000**, 1153-1154.

69) Rupon, J. W.; Domingo, S. R.; Smith, S. V.; Gummadi, B. K.; Shields, H.; Ballas, S. K.; King, S. B.; Kim-Shapiro, D. B. *Biophys. Chem*. **2000**, *84*, 1-11.

70) Nahavandi, M.; Tavakkoli, F.; Millis, R. M.; Wyche, M. Q.; Habib, M. J.; Tavakoli, N. *Hematology* **2006**, *11*, 291-294.

71) Huang, J.; Hadimani, S. B.; Rupon, J. W; Ballas, S. K.; Kim-Shapiro, D. B.; King, S. B. *Biochemistry* **2002**, *41*, 2466-2474.

72) King, S. B. *Free Radical Biol. Med*. **2004**, *37*, 737-744.

73) King, S. B. *Curr. Topics in Med. Chem*. **2005**, *5*, 665-673.

74) Lewis, R. S.; Deen, W. M. *Chem. Res. Toxicol*. **1994**, *7*, 568-574.

75) Galliker, B.; Kissner, R.; Nauser, T.; Koppenol, W. H. *Chem. Eur. J.* **2009**, *15*, 6161-6168.

76) Martí, M. A.; Bari, S. E.; Estrin, D. A.; Doctorovich, F. *J. Am. Chem. Soc*. **2005**, *127*, 4680-4684.

77) Xu, Y.; Szép, S.; Lu, Z. *Proc. Natl. Acad. Sci. U.S.A.* **2009**, *106*, 20515-20519.

78) $OSCN^-$ is derived from HOSCN known commonly as hypothiocyanous acid. The systematic (IUPAC) names of $OSCN^-$ and HOSCN are oxidothiocyanate and hydrogenoxidothiocyanate, respectively.

79) Hawkins, C. L. *Free Radical Res.* **2009**, *43*, 1147-1158.

80) Barrett, T. J.; Hawkins, C. L. *Chem. Res. Toxicol.* **2012**, *25*, 263-273.

81) Ashby, M. T. *Adv. Inorg. Chem.* **2012**, *64*, 263-303.

82) Figlar, J. N.; Stanbury, D. M. *Inorg. Chem.* **2000**, *39*, 5089-5094.

83) Kettle, A. J.; Winterbourn, C. C. *Redox Rep.* **1997**, *3*, 3-15.

84) Wang, J.; Slungaard, A. *Arch. Biochem. Biophys*. **2006**, *445*, 256-260.

85) Shin, K.; Tomita, M.; Lönnerdal, B. *J. Nutr. Biochem*. **2000**, *11*, 94-102.

86) Bjorck, L.; Rosen, C. G.; Marshall, V.; Reiter, B. *J. Appl. Microbiol.* **1975**, *30*, 199-204.

87) Ihalin, R.; Loimaranta, V.; Tenovuo, J. *Arch. Biochem. Biophys*. **2006**, *445*, 261-268.

88) Ashby, M. T. *J. Dent. Res*. **2008**, *87*, 900-914.

89) Wijkstrom-Frei, C.; El-Chemaly, S.; Ali-Rachedi, R.; Gerson, C.; Cobas, M. A.; Forteza, R.; Salathe, M.; Conner, G. E. *Am. J. Res. Cell Mol*. **2003**, *29*, 206-212.

90) Rada, B.; Leto, T. L. *Immunol. Res*. **2009**, *43*, 198-209.

91) Lorentzen, D.; Durairaj, L.; Pezzulo, A. A.; Nakano, Y.; Launspach, J.; Stoltz, D. A.; Zamba, G.; McCray, P. B., Jr.; Zabner, J.; Welsh, M. J.; Nauseef, W. M.; Bánfi, B. *Free Radical Biol. Med*. **2011**, *50*, 1144-1150.

92) Ashby, M. T.; Carlson, A. C.; Scott, M. J. *J. Am. Chem. Soc*. **2004**, *126*, 15976-15977.

93) Nagy, P.; Beal, J. L.; Ashby, M. T. *Chem. Res. Toxicol*. **2006**, *19*, 587-593.

94) Aune, T. M.; Thomas, E. L. *Eur. J. Biochem*. **1977**, *80*, 209-214.

95) Pruitt, K. M.; Mansson-Rahemtulla, B.; Tenovuo, J *Arch. Oral Biol.* **1983**, *28*, 517-525.

96) Botz, M. M.; Mudder, T. I.; Akcil, A. U. *Dev. Miner. Process*. **2005**, *15*, 672-702.

97) Batoeva, A. A.; Tsybikova, B. A.; Ryazantsev, A. A. *Russ. J. Appl. Chem*. **2010**, *83*, 993-996.

98) Collado, S.; Laca, A.; Díaz, M. *J. Hazard. Mater*. **2010**, *177*, 183-189.

99) Udrea, I.; Avramescu, S. *Environ. Technol*. **2004**, *25*, 1131-1141.

100) Vohra, M. S.; Selimuzzaman, S. M.; Al-Suwaiyan, M. S. *Int. J. Environ. Res*. **2011**, *5*, 247-254.

101) Vohra, M. S. *Fresenius Environ. Bull*. **2011**, *20*, 1308-1313.

102) Rorke, G. V.; Mühlbauer, R. M. *Process Met*. **1999**, *9*, 731-740.

103) Grigor'eva, N. V.; Smirnova, Y. V.; Dulov, L. E. *Microbiology* **2009**, *78*, 402-406.

104) Kita, Y.; Takada, T.; Mihara, S.; Whelan, B. A.; Tohma, H. *J. Org. Chem*. **1995**, *60*, 7144-7148.

105) Yadav, J. S.; Reddy, B. V. S.; Shubashree, S.; Sadashiv, K. *Tetrahedron Lett*. 2004, *45*, 2951-2954.

106) Wu, G.; Liu, Q.; Shen, Y.; Wu, W.; Wu, L. *Tetrahedron Lett*. **2005**, *46*, 5831-5834.

107) Prakash, O.; Kaur, H.; Batra, H.; Rani, N.; Singh, S. P.; Moriarty, R. M. *J. Org. Chem*. **2001**, *66*, 2019-2023.

108) Wu, G.; Wu, W.; Li, R.; Shen, Y.; Wu, L. *Chem. Lett*. **2007**, *36*, 188-189.

109) Anil Kumar, M.; Reddy, K. R. K. K.; Reddy, M. V.; Reddy, C. S.; Reddy, C. D. *Synth. Commun*. **2008**, *38*, 2089-2095.

110) Lente, G.; Kalmár, J.; Baranyai, Z.; Kun, A.; Kék, I.; Bajusz, D.; Takács, M.; Veres, L.; Fábián, I. *Inorg. Chem*. **2009**, *48*, 1763-1773.

111) Bellér, G.; Bátki, G.; Lente, G.; Fábián, I. *J. Coord. Chem*. **2010**, *63*, 2586-2597.

112) Smith, R. H.; Wilson, I. R. *Aust. J. Chem*. **1966**, *19*, 1357-1363.

113) Smith, R. H.; Wilson, I. R. *Aust. J. Chem*. **1966**, *19*, 1365-1375.

114) Smith, R. H.; Wilson, I. R. *Aust. J. Chem*. **1967**, *20*, 1353-1366.

115) Nagy, P.; Lemma, K.; Ashby, M. T. *Inorg. Chem*. **2007**, *46*, 285-292.

116) Lahaye, D.; Groves, J. T. *J. Inorg. Biochem*. **2007**, *101*, 1786-1797.

117) De Angelis, F.; Jin, N.; Car, R.; Groves, J. T. *Inorg. Chem*. **2006**, *45*, 4268-4276.

118) Groves, J. T.; Lee, J.; Marla, S. S. *J. Am. Chem. Soc*. **1997**, *119*, 6269-6273.

119) Barnett, J. J.; McKee, M. L.; Stanbury, D. M. *Inorg. Chem*. **2004**, *43*, 5021-5033.

120) Rayson, M. S.; Mackie, J. C.; Kennedy, E. M.; Dlugogorski, B. Z. *Inorg. Chem*. **2011**, *50*, 7440-7452.

121) Mamman, S.; Iyun, J. F. *Int. J. Pure Appl. Chem*. **2007**, *2*, 429-432.

122) Thomas, E. L. *Biochemistry* **1981**, *20*, 3273-3280.

123) Kornath, A.; Blecher, O.; Ludwig, R. *J. Am. Chem. Soc*. **1999**, *121*, 4019-4122.

124) Kornath, A.; Blecher, O. Z. *Anorg. Allg. Chem*. **2002**, *628*, 625-631.

125) Jander, G.; Gruttner, B.; Scholz, G. *Chem. Ber*. **1947**, *80*, 279-289.

126) Walden, P.; Audrieth, L. F. *Chem. Rev*. **1928**, *5*, 339-359.

127) Lemma, K.; Ashby, M. T. *Chem. Res. Toxicol*. **2009**, *22*, 1622-1628.

128) Prof. Ines Batinić-Haberle's group, Department of Radiation Oncology, Duke University Medical School, Durham, NC, USA.

129) Rebouças, J. S.; Kos, I.; Vujasković, Z.; Batinić-Haberle, I. *J. Pharm. Biomed. Anal.* **2009**, *50*, 1088-1091.

130) Spasojević, I.; Batinić-Haberle, I.; Fridovich, I. *Nitric Oxide: Biol. Chem*. **2000**, *4*, 526-533.

131) Adam, L. C.; Fabian, I.; Suzuki, K.; Gordon, G. *Inorg. Chem*. **1992**, *31*, 3534-3541.

132) Cooper, W. J.; Mehran, M. F.; Slifker, R. A.; Smith, D. A.; Villate, J. T.; Gibbs, P. H. *J. Am. Water Works Assoc.* **1982**, *74*, 546-552.

133) Barnett, J. J.; Stanbury, D. M. *Inorg. Chem.* **2002**, *41*, 164-166.

134) Nagy, P.; Alguindigue, S. S.; Ashby, M. T. *Biochemistry* **2006**, *45*, 12610-12616.

135) Wood, J. L. Org. React. (New York, NY, United States) **1946**, 240.

136) Lemma, K.; Ashby, M. T. *J. Org. Chem.* **2008**, *73*, 3017-3023.

137) Nagy, P.; Wang, X.; Lemma, K.; Ashby, M. T. *J. Am. Chem. Soc*. **2007**, *129*, 15756-15757.

138) Aune, T. M.; Thomas, E. L.; Morrison, M. *Biochemistry* **1977**, *16*, 4611-4615.

139) Covington, A. K.; Bates, R. G.; Durst, R. A. *Pure Appl. Chem.* **1983**, *55*, 1467-1476.

140) van Geet, A. L. *Anal. Chem.* **1970**, *42*, 679-680.

141) Vold, R. V.; Waugh, J. S.; Klein, M. P.; Phelps, D. E. *J. Chem. Phys.* **1968**, *48*, 3831-3832.

142) Powel, D. H.; Merbach, A. E. *Magn. Reson. Chem.* **1994**, *32*, 739-745.

143) Swift, T. J.; Connick, R. E. *J. Chem. Phys.* **1962**, *37*, 307-320, (ibid, **1964**, *41*, 2553-2554).

144) Ducommun, Y.; Newman, K. E.; Merbach, A. E. *Inorg. Chem.* **1980**, *19*, 3696-3703.

145) Tonomura, B.; Nakatani, H.; Ohnishi, M.; Yamaguchi-Ito, J.; Hiromi, K. *Anal. Biochem.* **1978**, *84*, 370-383.

146) Dickson, P. N.; Margerum, D. W *Anal. Chem.* **1986**, *58*, 3153-3158.

147) Specfit/32 by Spectrum Software Associates is a multivariate data analysis program for modelling and fitting chemical kinetics and equilibrium titration multi-wavelength spectrophotometric data sets.

148) SCIENTIST, version 2.0; Micromath Software: Salt Lake City, UT, **1995**.

149) Peintler, G. ZiTa: A comprehensive program package for fitting parameters of chemical reaction mechanisms, version 4.1; Institute of Chemistry JATE: Szeged, Hungary, 1997. The first use of this program was described in: Peintler, G.; Nagypal, I.; Epstein, I. R. *J. Phys. Chem.* **1990**, *94*, 2954-2958.

150) Hindmarsh, A. C. GEAR: Ordinary Differential Equation SolVer, revision 2; Lawrence Livermore Laboratory: Livermore, CA, **1972**.

151) Cheng, R.-J.; Chang, S.-H.; Kuo-Cheng Hung, K.-C. *Inorg. Chem.* **2007**, *46*, 1948-1950.

152) Fuoss, R. M. *J. Am. Chem. Soc.* **1958**, *80*, 5059-5061.

153) Summers, J. S.; Base, K.; Boukhalfa, H.; Payne, J. E.; Shaw, B. R.; Crumbliss, A. L. *Inorg. Chem.* **2005**, *44*, 3405-3411.

154) Gabričević, M.; Bešić, E.; Biruš, M.; Zahl, A.; van Eldik, R. *J. Inorg. Biochem*. **2006**, *100*, 1606-1613.

155) Budimir, A.; Bešić, E.; Biruš, M. *Croatica Chemica Acta*, **2009**, *82*, 807-818.

156) Fábián, I.; Lente, G. *Pure Appl. Chem*. **2010**, *82*, 1957-1973.

157) Peintler, G.; Nagypál, I.; Jancsó, A.; Epstein, I. R.; Kustin, K. *J. Phys. Chem. A* **1997**, *101*, 8013-8020.

158) Peintler, G.; Nagypál, I.; Epstein, I. R.; Kustin, K. *J. Phys. Chem. A* **2002**, *106*, 3899-3904.

159) Bellér, G.; Bátki, G.; Lente, G.; Fábián, I. *J. Coord. Chem.* **2010**, *63*, 2586-2597.

160) Pellegrino, J.; Hübner, R.; Doctorovich, F.; Kaim, W. *Chem. Eur. J.* **2011**, *17*, 7868-7874.

161) Miranda, K. M. *Coord. Chem. Rev*. **2005**, *249*, 433-455.

162) Kormányos, B.; Horváth, A. K.; Peintler, G.; Nagypál, I. *J. Phys. Chem. A* **2007**, ***111***, 8104-8109.

163) Weitner, T.; Bešić, E.; Kos, I.; Gabričević, M.; Biruš, M. *Tetrahedron Lett*. **2007**, *48*, 9021-9024.

164) Gabričević, M. *Reac. Kinet. Mech. Cat*. **2012**, *105*, 223-232.

165) Zavarine, I. S.; Kini, A. D.; Morimoto, B. H.; Kubiak, C. P. *J. Phys. Chem. B* **1998**, *102*, 7287-7292.

166) Espenson, J. H. Chemical Kinetics and Reaction Mechanisms, 2nd ed.; McGraw-Hill Series in Advanced Chemistry; McGraw-Hill Inc.: New York, **1995**; pp 49-52.

167) SO_4^{2-} is in excess over SO_5^{2-} even in Oxone, which is used as the SO_5^{2-} source.

168) $SCN^- + 2OH^- \rightarrow OSCN^- + H_2O + 2e^-$ ($\varepsilon = -0.44$ V at pH ca. 7).
$HSO_5^- + 2e^- \rightarrow SO_4^{2-} + OH^-$ ($\varepsilon = +1.44$ V at pH ca. 7).

169) Reijenga, J. C.; Gagliardi, L. G.; Kenndler, E. *J. Chromatogr. A* **2007**, *1155*, 142-145.

170) Lente, G.; Fábián, I.; Poë, A. J. *New J. Chem*. **2005**, *29*, 759-760.

171) Stanbury, D. M. *Adv. Inorg. Chem*. **1989**, *33*, 69-138.

172) Umile, T. P.; Wang, D.; Groves, J. T. *Inorg. Chem.* **2011**, *50*, 10353-10362.

173) Nagy, P.; Jameson, G. N. L.; Winterbourn, C. C. *Chem. Res. Toxicol*. **2009**, *22*, 1833-1840.

174) Figlar, J. N.; Stanbury, D. M. *J. Phys. Chem. A* **1999**, *103*, 5732-5741.

175) Lengyel, I.; Epstein, I. R.; Kustin, K. *Inorg. Chem*. **1993**, *32*, 5880-5882.

176) Palmer, D. A.; Van Eldik, R. *Inorg. Chem*. **1986**, *25*, 928-931.

177) Truesdale, V. W.; Luther, G. W.; Greenwood, J. E. *Phys. Chem. Chem. Phys*. **2003**, *5*, 3428-3435.

178) Skaff,O.; Pattison, D. I.; Davies, M. J. *Biochem. J*. **2009**, *422*, 111-117.

179) van Dalen, C. J.; Whitehouse, M. W.; Winterbourn, C. C.; Kettle, A. J. *Biochem. J*. **1997**, *327*, 487-492.

180) Van Dalen, C. J.; Kettle, A. J. *Biochem. J.* **2001**, *358*, 233-239.

181) Slungaard, A.; Mahoney, J. R., Jr. *J. Biol. Chem*. **1991**, *266*, 4903-4910.

182) Das, D.; De, P. K.; Banerjee, R. K. *Biochem. J.* **1995**, *305*, 59-64.

183) Pollock, J. R.;Goff, H.M. *Biochim. Biophys. Acta* **1992**, *1159*, 279-285.

184) Wang, Z.; Nicholls, S. J.; Rodriguez, E. R.; Kummu, O.;Hörkkö, S.; Barnard, J.; Reynolds, W. F.; Topol, E. J.; DiDonato, J. A.; Hazen, S. L. *Nature Med.* **2007**, *13*, 1176-1184.